ASSESSMENT OF THE EFFECT OF UAV AND PLEIADES SPATIAL RESOLUTION AND BAND COMBINATION ON BIOMASS ESTIMATION IN HAAGSE BOS, THE NETHERLANDS.

MISHECK LESA CHUNDU
June 2021

SUPERVISORS:
Dr. M. Schlund
Ir. L.M. van Leeuwen

ASSESSMENT OF THE EFFECT OF UAV AND PLEIADES SPATIAL RESOLUTION AND BAND COMBINATION ON BIOMASS ESTIMATION IN HAAGSE BOS, THE NETHERLANDS.

MISHECK LESA CHUNDU

Enschede, The Netherlands, June 2021

Thesis submitted to the Faculty of Geo-Information Science and Earth Observation of the University of Twente in partial fulfilment of the requirements for the degree of Master of Science in Geo-information Science and Earth Observation.

Specialization: Natural Resource Management

SUPERVISORS:
Dr. M. Schlund
Ir. L.M. van Leeuwen

THESIS ASSESSMENT BOARD:
Dr. R. Darvish (Chair)
Prof dr T. Kauranne (External Examiner, Lahti University of Technology)

DISCLAIMER

This document describes work undertaken as part of a programme of study at the Faculty of Geo-Information Science and Earth Observation of the University of Twente. All views and opinions expressed therein remain the sole responsibility of the author, and do not necessarily represent those of the faculty.

ABSTRACT

Forests play an important role in mitigating climate change because they act as both a carbon sink and a carbon source. Climate change is putting increasing pressure on the forest ecosystems of European forests. Most of the carbon is stored in the forest Aboveground biomass (AGB), which is used in carbon inventory and mitigation and as an essential climate variable and a critical input to the United Nations' Reducing Emissions from Deforestation and Degradation-plus (REDD+) program. 50% of dry forest AGB represents carbon; therefore, accurate estimation of forest AGB is a vital step in monitoring carbon stocks and changes in the forest. The effective and accurate estimation of forest AGB is one of the most challenging tasks; finding a reliable and accurate method to estimate forest AGB is critical.

Remote sensing is well-placed to provide accurate, realistic, and cost-effective AGB estimates with large spatial and multi-temporal observation. Unmanned Aerial Vehicle (UAV) is less expensive, provides reliable data quality, and multitemporal capturing of forest parameters at a very high spatial resolution. The satellite data (Pleiades) is readily available with huge datasets archived, large spatial coverage, provide consistent spatial data, repetitive with high revisit time (daily), as well as a relatively cost-effective way of biomass estimation at a large scale.

This research aimed to extract the crown projection area (CPA) of individual trees in a coniferous forest through Object-Based Image Analysis (OBIA) of UAV and Pleiades satellite images with different spatial resolutions (10 cm, 20 cm, 30 cm, 40 cm, and 50 cm) and band combinations (1,1,1,4 –UAV_MS, 1,4,1,0 –UAV_RGB and 1,1,1,4 – Pleiades); investigate if variations in the extracted CPA leads to significant differences in AGB estimates. The fieldwork was carried out between August 2020, and October 2020. Pleiades satellite image was acquired on August 22, 2019. The UAV_MS and UAV_RGB images were acquired in August 2020 and September 2020 using the Phantom 4 drone.

The t-test results showed that means of the UAV_MS and UAV_RGB modelled AGB (AGB-est) per tree at 10 cm spatial resolution were not significantly different from means of the field estimated AGB (AGB-f) per tree. At 20 cm and 30 cm spatial resolutions, the means of the field estimated AGB-f per tree were also not significantly different from the means of the AGB-est per tree estimated with UAV_MS, but significantly different from the means of AGB-est per tree estimated with UAV_RGB. The means of field estimated AGB-f per tree were significantly different from the means of AGB-est per tree from both UAV_MS and UAV_RGB at 40 cm and 50 cm resolutions as well as Pleiades at 50 cm spatial resolution.

The t-test results for AGB per plot (500 m^2), showed that there were no significant differences between the means of the AGB-f per plot and the means of AGB-est per plot estimated from UAV_RGB and UAV_MS at 10 cm, 20 cm, 30 cm, 40 cm, and 50 cm as well as Pleiades at 50 cm spatial resolution.

It was concluded that the AGB per tree could be accurately estimated at 10 cm spatial resolution with UAV_MS and UAV_RGB, as well as at 20 cm and 30 cm spatial resolution with UAV_MS. The AGB per plot could be estimated with reasonable accuracy using UAV_RGB and UAV_MS at 10 cm, 20 cm, 30 cm, 40 cm, and 50 cm spatial resolutions as well as Pleiades at 50 cm spatial resolution.

***Key words**: Aboveground biomass, Crown Projection Area, Object-Based Image Analysis, Unmanned Ariel Vehicle, Pleiades, Near infrared band, green band, spatial resolution, and band combinations.*

ACKNOWLEDGEMENT

My sincere gratitude goes to NUFFIC - Orange Knowledge Program (OKP) for granting me a wonderful scholarship to study at ITC, University of Twente, The Netherlands. Otherwise, this research would not have been possible.

My heartfelt thanks and appreciation go to the following special people: My late father, Raymond Lesa, who would have loved to read my MSc research work, unfortunately, died one month before starting this program. I wish he were alive to see this coming to reality. My beloved aged mother Elizabeth Chanda, for the love and moral support she always showed towards me, I am grateful. Special thanks go to my wife, Lillian Mambepa Chundu, and my beloved daughter Moriah Lesa Chundu for the love, moral and spiritual support they rendered to me from the beginning of this research work to the end.

I am Indebted to my two supervisors Dr M. Schlund and Ir. L.M. van Leeuwen for being available for me each time I called on them and for their guidance, suggestions and advice rendered to me during this research work. In addition, I am also grateful to Drs. E.H Kloosterman for being so instrumental during the initial development of this research.

Above all, I thank the almighty God that this research became a reality.

Misheck Lesa Chundu,
June 2021,
Enschede.

TABLE OF CONTENT

1. INTRODUCTION 1
1.1 Background 1
1.2. Remote sensing sensors 3
1.3. Remote sensing platforms 4
1.3. Band combinations 4
1.4. Conceptual diagram 5
1.5. Research problem 6
1.6. Research objectives 6
2.0. MATERIALS AND METHODS 8
2.1. Study area 8
2.2. Sampling Design used 9
2.3. Plot size 9
2.4. Field equipment 9
2.5. Field data collection and processing 10
2.6. UAV flight planning 10
2.7. UAV data acquisition and processing 11
2.8. Very High-Resolution (VHR) imagery data 13
2.9. Object-Based Image Analysis (OBIA) 13
2.10. Descriptive Statistics and Normality Tests 15
2.11. Reference Crown Projection Area (CPA) 15
2.12. Segmentation accuracy assessment 16
2.13. Biomass Calculation 18
2.14. Field measured and Modelled AGB. 19
2.15. Comparing field measured and modelled AGB and significance test. 19
2.16. Summary of research methods 20
3. RESULTS 21
3.1. Descriptive Statistics and Normality Tests for Diameter at Breast Height data. 21
3.2. Relationship between reference CPA-r and field measured DBH-f 21
3.3. Relationship between manually Orthophoto segmented CPA-r and automatic 22
3.4. Relationship between field estimated DBH-f and modelled DBH-est 25
3.5. Biomass calculations and comparison 28
F-test and t-test of field measured biomass and modelled biomass per tree 31
4. DISCUSSION 39
4.1. Relationship between reference CPA-r and field measured DBH-f 39
4.2. Relationship between reference CPA-r and automatic segmented CPA-rs 40
4.3. Relationship between field measured DBH-f and estimated DBH-est. 41
4.4. Biomass calculations and comparison per tree and plot. 41
4.5. Uncertainties 43
4.6 Limitations 44
5.0. CONCLUSION AND RECOMMENDATIONS 45

5.1. Conclusion 45
5.2. Recommendations 45
List of references 46
Appendices 56

LIST OF FIGURES

Figure 1: Conceptual diagram 5
Figure 2: Study area location 8
Figure 3: UAV flight plan. 11
Figure 4: Summary of Pix4D photogrammetry initial report. 11
Figure 5: Resampled images in true colour composite (1,2,3-RGB) 12
Figure 6: Procedure for selecting the reference CPA: (RQ 1a) research question 1a. 15
Figure 7: Segmentation accuracy assessment 16
Figure 8: Procedure for CPA segmentation accuracy assessment: (RQ 2a) research question 2a. 17
Figure 9: Procedure for DBH modelling: (RQ 3a) research questions 3a. 18
Figure 10: Procedure for AGB estimation: (RQ 4a) research questions 4a 19
Figure 11: Workflow summary of the research methods. 20
Figure 12: a) Histogram and b) Box-Whisker-plot of the field measured DBH samples 21
Figure 13: Relationship between field measured DBH and UAV_RGB Nadir image digitized CPA: 22
Figure 14: Relationship between field measured DBH and UAV_RGB Orthophoto digitized CPA: a) 22
Figure 15: Effect of UAV image resolution on segmentation accuracy. 23
Figure 16: Relationship between UAV orthophoto automatic segmented CPA and manually 24
Figure 17: Relationship between 24
Figure 18: UAV and Pleiades tree detection at different resolutions compared to field observed 26
Figure 19: Relationship between tree detection accuracy and UAV spatial resolution 26
Figure 20: Relationship between field measured DBH-f and UAV modelled AGB-est per tree: a) 27
Figure 21: Relationship between field 27
Figure 22: Relationship between UAV modelled AGB-est and field estimated AGB-f: 29
Figure 23: Relationship between field 30
Figure 24: Mean AGB per plot (mg) 33
Figure 25: Relationship between field estimated AGB-f and UAV modelled AGB-est per plot: 34
Figure 26: Relationship between field estimated 34
Figure 27: Comparison of mean AGB (mg/ha) 36
Figure 28: Effects of spatial resolution on AGB estimation. 36
Figure 29: Illustration of a Logistic function (Lechman, 2014). 39

LIST OF TABLES

Table 1: Field instruments used. 9
Table 2: Collected field data. 10
Table 3: Types and number of coniferous tree species collected. 10
Table 4: Flight plan parameters 11
Table 5: Band combinations 14
Table 6: Summary of UAV orthophoto segmentation accuracy assessment results 23
Table 7: Pleiades segmentation accuracy assessment results 23
Table 8: Summary of the relationship between UAV automatic segmented CPA-rs and 25
Table 9: Summary of the relationship between Pleiades automatic segmented CPA and 25
Table 10: Summary of the relationship between Field measured DBH-f and UAV modelled DBH. 28
Table 11: Summary of the relationship between Field measured DBH-f and Pleiades modelled 28
Table 12: Descriptive statistics summary of field measured AGB-f per tree (kg) 28
Table 13: Descriptive statistics summary of UAV modelled AGB-est per tree. 29
Table 14: Descriptive statistics summary of Pleiades modelled AGB-est per tree. 29
Table 15: Summary of the Relationship between field estimated AGB and UAV modelled AGB. 30
Table 16: Summary of the Relationship between field estimated AGB and Pleiades modelled AGB ... 30
Table 17: Summary of the F-test results for field AGB-f and modelled AGB-est per tree 31
Table 18: Summary of the t-test results for field AGB-f and modelled AGB-est per tree 32
Table 19: Descriptive statistics summary of field estimated AGB per plot 32
Table 20: Descriptive statistics summary of UAV modelled AGB-est per plot. 33
Table 21: Descriptive statistics summary of Pleiades modelled AGB-est per plot. 33
Table 22: Summary of the Relationship between field estimated AGB-f and UAV modelled AGB- 35
Table 23: Summary of the Relationship between field estimated AGB-f and Pleiades modelled *35*
Table 24: Summary of the F-test results for AGB-f and AGB-est per plot 37
Table 25: Summary of the t-test results for AGB-f and AGB-est per plot 38

ACRONYMS

3D	3 - Dimension
3x3 LPF	3 x 3 low pass filter
AGB	Aboveground Biomass
CDM	Clean Development Mechanism
COP 15	Conference of parties 15
CPA	Crown Projection Area
DBH	Diameter at Breast Height
DGPS	Differential Global Positioning System
ESA	European Space Agency
EU	European Union
GCOS	The Global Climate Observing System
GCPs	Ground Control Points
ha	Hectare
kg	Kilogram
LiDAR	Light Detecting and Ranging
m^2	Meter squared.
MRV	Measurement, Reporting and Verification
NIR	Near Infrared band
OBIA	Object-Based Image Analysis
RADAR	Radio Detecting and Ranging
REDD+	Reducing Emissions from Deforestation and Degradation-plus
RGB	Red-Green-Blue bands
RMSE	Root Mean Square Error
MS	Multispectral sensor
rRMSE	Relative Root Mean Square Error
SEEA EEA	System of Environmental-Economic Accounting-Experimental Ecosystem Accounting
UAV	Unmanned Ariel Vehicle
UNFCCC	United Nations Framework Convention on Climate Change
VHR	Very High Resolution

1. INTRODUCTION

1.1 Background

The earth's forests cover approximately 30 percent of the land (Food and Agriculture Organization, 2015). Forests play a crucial role in mitigating the earth's climate change because it acts as both a carbon sink and source. On the one hand, the forest acts as a sink by absorbing carbon dioxide from the atmosphere and converting it into living biomass stored in terrestrial carbon sinks. These carbon sinks include tree trunks, roots, branches, and leaves. Geographically, 54 percent of global forest carbon is stored in a tropical forest, 32 percent in the boreal forest, and 14 percent in temperate forests (Brack, 2019). On the other hand, the chopping or burning of trees for cropland, pasture, infrastructure, among others, will release the stored carbon into the atmosphere (Watson et al., 2000; Ciais et al., 2013).

There are five carbon pools of terrestrial biomass ecosystem, namely, the Aboveground biomass (AGB), Belowground biomass, the dead mass litter, wood debris, and soil organic matter. The carbon dioxide that is fixed in the trees during photosynthesis is transported across the five different carbon pools. The majority of carbon dioxide is stored in the AGB carbon pool. Therefore, AGB is the most important carbon pool of the terrestrial forest ecosystem, and it has since been given the highest importance in carbon inventory and mitigation projects such as afforestation and reforestation Clean Development Mechanism (CDM) under Kyoto Protocol (Gytarsky, Kurz, Ogle, Richards, & Somogyi, 2006; Ravindranath.N.H. & Ostwald, 2008). The Global Climate Observing System (GCOS) has acknowledged the fact that forest AGB is an essential climate variable and a critical input to the United Nations' Reducing Emissions from Deforestation and Degradation-plus (REDD+) program; however, one of the greatest challenges of REDD+ is the effective and accurate estimation of forest biomass (Kankare et al., 2013).

The European Union (EU) member states' forest ecosystem is under increasing pressure because of climate change; therefore, the European Commission has set up a set of policy initiatives (European Green Deal) for the EU and its citizens. The European Green Deal aims to tackle climate change and make Europe climate-neutral and a healthy environment in 2050 by promoting innovative technologies such as carbon capture, storage, and utilization. The policy encourages forest managers to preserve, grow and manage the forest sustainably, as well as emphasizes the role that European forest sustainable management has in the fight against climate change (The European Green Deal, 2020; European Commission, 2019).

In 2013, the United Nations Statistical Commission endorsed the System of Environmental-Economic Accounting-Experimental Ecosystem Accounting (SEEA EEA) as a basis for testing and development of national carbon accounting. In line with the guidelines provided by SEEA-EEA, in 2016, the Netherlands embarked on the natural capital accounting project to allow for the consistent and quantitative comparison of carbon stocks and flows in reservoirs such as organic carbon stored in forest biomass (SEEA Experimental Ecosystem Accounting Revision | System of Environmental-Economic Accounting, 2020; Lof et al., 2017).

It should be noted that the total forest AGB is linked to the amount of carbon stored in the forest vegetation as research shows that about fifty percent (50 %) of dry forest biomass is carbon; thus, accurate estimation of forest AGB is a very critical step in measuring carbon stocks as well as its fluctuations in the forest (Penman et al., 2003; Saatchi et al., 2011). Therefore, finding a reliable and accurate method that can be used to estimate the forest AGB accurately is important for sustainable

forest management, climate change mitigation, greenhouse gas inventories, and global and national carbon accounting, as well as the implementation of both the European Green Deal policy and Kyoto Protocol of the United Nations Framework Convention on Climate Change (UNFCCC) (Duncanson et al., 2019; Herold et al., 2019; The European Green Deal, 2020 and Nichol & Sarker, 2011).

The review paper on the methods to estimate AGB and carbon stock in natural forests by (Vashum, 2012) stated that remote sensing could be able to overcome the numerous challenges faced by conventional methods as well as the only realistic and cost-effective method of acquiring forest data with large spatial and temporal coverage. Also, remote sensing technologies are vital methods that could be used for regular forest monitoring with large spatial coverage and multi-temporal observation, thereby providing a synoptic view over large areas and significantly increase the efficiency of conventional methods of AGB estimation (Calders, Jonckheere, Nightingale, & Vastaranta, 2020; Romijn, Herold, Kooistra, Murdiyarso, & Verchot, 2012 and Patenaude, Milne, & Dawson, 2005). In addition, Hirata, Takao, Sato, & Toriyama (2012) explained that in the implementation of REDD+, accurate measurement, reporting, and verification (MRV) of forest carbon stocks is essential to ensure transparency in issuing economic incentives; a guidance for the methodology determined by the conference of parties 15 (COP 15) under UNFCCC recommended a monitoring system that can combine remote sensing with ground-based inventory to estimate the balance of forest carbon storks.

There has been an increase in the availability of remote sensing imagery with different spectral, radiometric, temporal, and spatial resolution details, which has been used of late to non-destructively estimate forest parameters such as crown projection area (CPA), tree height, diameter at breast height (DBH); these parameters are used in regression models to estimate AGB with the help of allometric equations (Gibbs, Brown, Niles, & Foley, 2007). The allometric equation is the mathematical relation between AGB and its DBH or both DBH and tree height; it is a standard equation used for non-destructive estimation of AGB. The tree CPA can be directly estimated by remote sensing while DBH can not be directly estimated; thus, the CPA is used as a proxy for the DBH. This is because the DBH can be estimated from CPA using statistical models to establish the correlation between field measured DBH and remotely sensed estimated CPA (Chave et al., 2014; Kumar & Mutanga, 2017 and Pizaña, Hernández, & Romero, 2016).

The status of forest biomass can be managed and monitored by using two methods, namely, in-situ forest inventories and remote sensing methods. In-situ forest inventory is the most conventional and accurate method for estimating AGB; however, it is very strenuous, expensive, destructive, unable to assess abrupt short-term forest change and has very limited temporal and spatial coverage; in some cases where the area is too remote to be accessed, it is not applicable (Lausch et al., 2017; Vashum 2012). A review of approaches and data models on understanding forest health with remote sensing by Lausch et al. (2017) concluded that remote sensing methods are more suitable and sustainable in monitoring forest conditions compared to the in-situ inventory. Boyd & Danson (2005) also mentioned that remote sensing is well-placed to provide accurate and detailed information about the spatial extent of the forest cover, forest type, and condition leading to improved monitoring of forest biomass.

1.2. Remote sensing sensors

There are two types of remote sensing sensors used for forest parameter estimation, namely, active, and passive sensors, each with different characteristics of spectral, radiometric, temporal, and spatial resolution details as well as different strengths and weaknesses. Active sensors include Radio Detecting and Ranging (RADAR) and Light Detecting and Ranging (LiDAR), passive sensors include optical sensors (Mitchard, 2016; Sinha, Jeganathan, Sharma, & Nathawat, 2015).

Active Sensors

RADAR has been used to estimate forest AGB as well as the mapping of forest degradation. RADAR sensors can operate in all weather conditions and without obstruction from clouds and smoke (Rignot, Salas, & Skole, 1997). However, RADAR sensors are less precise in thick tree canopies of the older forests as they experience signal saturation (Joshi et al.,2017). Also, using RADAR to estimate AGB in mountainous or hilly terrain increases errors. Furthermore, RADAR data is usually expensive and technically demanding (Gibbs et al., 2007).

LiDAR has also been used to estimate the forest aboveground biomass and degradation (Mutwiri, Odera, & Kinyanjui, 2017). However, most LiDAR data commercially available is very expensive and technically demanding and requires extensive field data for calibration (Mitchard, 2016; Gibbs et al., 2007).

Passive Sensors

Optical remote sensing has been operational for more than three decades. Optical satellite data is collected routinely, very consistent, and available at both local and global scales, and the data has been used for AGB estimation (Gibbs et al., 2007; Asner, 2001). Satellite optical spatial resolution is divided into low (above 100 m), medium (between 10 m to 100 m), and high (less than 10 m). High resolution is further subdivided into high (5 m to less than 10 m) and very high (less than 5 m) (Fernández-Manso, Fernández-Manso, & Quintano, 2014; Lu, 2006). However, Navulur (2006) defined different spatial resolution as follows; low resolution above 30 m, medium resolution as a range of 2 m to 30 m, high resolution as above 0.5 m to 2 m, and very high resolution as 0.5 m and below. Sousa, Gonçalves, & da Silva (2017), in their review on the recent methods to estimate forest aboveground biomass using remote sensing data, stated that estimating forest parameters using low (above 100 m) and medium (between 10 m to 100 m) spatial resolution images is not possible because the pixel size does not allow the separation of the individual trees thereby making it difficult to identify and delineate individual tree crowns. The author concluded that high spatial resolution images overcome this challenge and can estimate aboveground biomass using forest parameters at both local and regional scales. Furthermore, Noorian et al. (2016) added that even though medium spatial resolution imagery has been the most used data for forest parameters estimation so far, high spatial resolution imagery leads to more accurate estimation of forest parameters as they can detect and recognize the spectral reflectance of the canopy crown and usually have fewer mixed pixels.

The literature review on the use of very high-resolution images shows that four sensors have mostly been used for forest AGB estimation; these sensors include IKONOS, Quickbird, Worldview and Pleiades. Recently, very high-resolution sensors contribute up to 20% of the studies on forest AGB estimation (Issa, Dahy, Ksiksi, & Saleous, 2020; Sousa et al., 2017 and Maack et al., 2015). The Pleiades provides very high-resolution imagery (50cm) and information in record time with daily revisit time to any point on earth, making it ideal for large scale area mapping of forest biomass (Pleiades-Satellite Sensor | Satellite Imaging Corp, 2021). Maack et al. (2015) examined if the combination of photogrammetric, textural, and spectral information derived from very high resolution (the Pleiades and worldview-2 sensors) could improve the accuracy of forest biomass estimation across two tests sites in Chile and Germany. It was observed that for both sensors, the

combination of photogrammetric information with either spectral or texture information with more field plots improves the accuracy of forest biomass estimation. Song et al. (2010) used Quickbird and IKONOS images to investigate the potential of using a different spatial resolution to estimate forest parameters in Ohio, USA, and Duke Forest in North Carolina Piedmont, USA. The paper concluded that the use of models to estimate tree crowns using image variance at different spatial resolutions can be generalized and applied across sensors and study sites.

The Unmanned Ariel Vehicle (UAV) spatial resolution is affected by the flight altitude; the lower the flight altitude, the higher the spatial resolution, but the lower the spatial coverage and vice versa (Borra-Serrano, Peña, Torres-Sánchez, Mesas-Carrascosa, & López-Granados, 2015; Whitehead & Hugenholtz, 2014). Research by Okojie (2017) was conducted in Ahaus, Germany, on forest tree parameter extractability from the UAV-RGB data set. In his research, the Object-Based Image Analysis (OBIA) technique was used to evaluate the extractability of tree CPA at six different spatial (resampled) resolutions (4.8 cm, 10 cm, 15 cm, 20 cm, 25 cm, and 30 cm) to determine the optimal resolution for tree CPA extraction.

1.3. Remote sensing platforms

Sensors can be mounted on three commonly used remote sensing platforms: Aircraft, Unmanned Aerial Vehicle (UAV), and satellite. Aircraft mounted with Optical, LiDAR, and RADAR sensors have been used for biomass estimation. However, high-cost maintenance, complex data acquisition, lack of free manoeuvre, inability to fly at low altitudes, and close to the object limit the application of Aircraft in biomass estimation (Mitchard, 2016; Yang et al., 2017 and Lu et al., 2019).
UAV has been used at the local scale estimation of forest biomass. The rise in the use of cheap UAV since 2011 in forest monitoring and research has made it possible to successfully capture data frequently at high resolution over the area of interest, and With UAV, a survey can be repeated as often as required using the same sensor at reduced data collection costs compared to Aircraft based data (Mitchard, 2016). Lausch et al. (2017) also added that UAVs could carry various forms of sensor types, thus contributing to a more complete, quick, less expensive, reliable data quality, and multitemporal capturing of forest parameters a very high resolution. The satellite platform (spaceborne system) is the most used in AGB estimation because it is readily available with huge datasets archived, large spatial coverage, provide consistent spatial data, repetitive with high revisit time, as well as a relatively cost-effective way of biomass estimation at large scale (Kumar, Sinha, Taylor, & Alqurashi, 2015; Issa, Dahy, Ksiksi, & Saleous, 2020).

1.3. Band combinations

Sensors have a different number of bands and band widths, and each band is narrowly focused on a just particular range of the electromagnetic spectrum which is sensitive to a specific feature on the ground; this makes forest parameters and spectral signatures respond differently to different band combinations (Xue & Su, 2017). In this research, the following sensor bands were used: Pleiades with four bands (Blue = 430 – 550 nm, Green = 490 – 610 nm, Red = 600 – 720 nm, and Near-Infrared = 750 nm – 950 nm), and UAV: parrot sequoia which is a multispectral sensor (MS) with four bands (Green= 530 – 570 nm, Red 640 – 680 nm, Red Edge = 730 – 740 nm, Near infrared (NIR) = 770 – 810 nm) and Phantom 4 camera (RGB) with 3 bands (Blue = 455 to 492 nm, Green = 492 – 577 nm, Red = 622 – 780 nm) (Holman, Riche, Castle, Wooster, & Hawkesford, 2019; Wang et al., 2018 and Carrasco-Escobar et al., 2019).

The Red band is one of the most important bands for vegetation discrimination as it focuses on the absorption of red light by chlorophyll in plants. The Green band is strongly correlated with chlorophyll and focuses specifically on the peak reflectance of plants. The green is ideal for

discriminating between types of plant materials. Plant's chlorophyll and carotenoid absorption are associated with the blue band. Therefore, the band is useful in discriminating within the groups of conifers and between conifers and broadleaf species based on their leaf's senescence. (Elhabiby, Elsharkawy, & El-Sheimy, 2012; Alonzo, Bookhagen, & Roberts, 2014). The Near-infrared band is very effective in estimating plant biomass and helps to separate other objects from vegetation effectively and identify types of vegetation. Combining these individual bands improves image segmentation and plant classification (Elhabiby, Elsharkawy, & El-Sheimy, 2012; Hennessy, Clarke, & Lewis, 2020).

1.4. Conceptual diagram

Figure 1 shows the conceptual diagram of this research showing the relevant key system concepts and data requirements and application. The system boundary is Haagse Bos, the Netherlands. Remote sensing (UAV and Pleiades) which is outside the system was used to estimate the systems' elements (trees) parameters which were validated by field measurements. Various stakeholders such as private owners and non-governmental organisations (NGOs) and the government manage the forest.

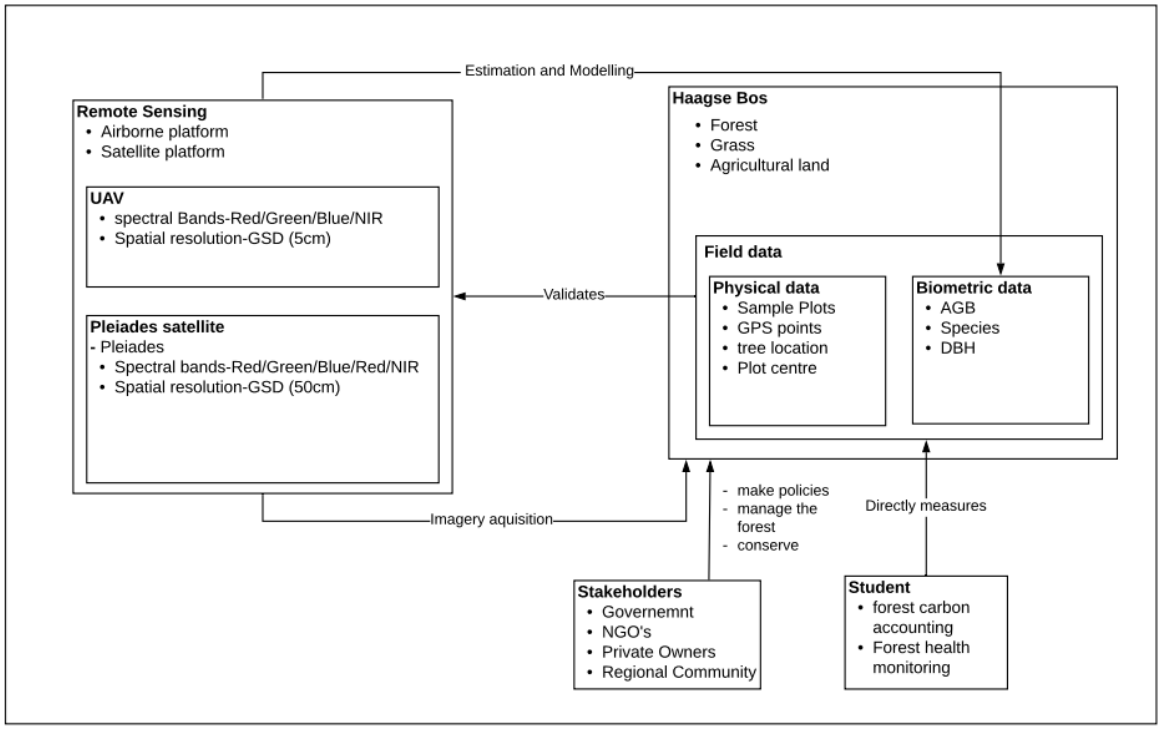

Figure 1: Conceptual diagram

1.5. Research problem

Forests are of great importance, as earlier alluded to in section 1.1. The total forest AGB is linked to the amount of carbon stored in the forest vegetation. The estimation of AGB can be done using different sensors with different spatial resolutions and spectral bands (Lu & Batistella, 2005; Noorian et al., 2016 and Sousa et al., 2017). Forest parameters and spectral signatures respond differently at different spatial resolutions and band combinations, which could significantly affect forest parameter and AGB estimation accuracy. However, there is scanty information, and little study has been done to systematically analyse how changing spatial resolution (resampling) and spectral band combinations would affect the accuracy of temperate coniferous forest parameters estimation and the subsequent effect on biomass estimation. Therefore, this research aims to extract the CPA of individual trees in a forest through image segmentation of UAV and Pleiades satellite images at different spatial resolutions and band combination; it will investigate if variations in the extracted CPA leads to lead to significant differences in AGB estimates. This will contribute to scientifically validated remote sensing-based methods for assessing and monitoring forest biomass and carbon sequestration.

1.6. Research objectives

1.6.1. Main objective

The main objective of this thesis is to determine if the effect of different spatial resolutions and spectral band combinations of the Unmanned Aerial Vehicle and Pleiades satellite imagery on the accuracy of forest parameter estimation leads to significant differences in Above Ground Biomass estimation.

1.6.2. Specific objectives

1. To establish the relationship between field measured Diameter at Breast Height (DBH-f) and reference Crown Projection Area (CPA-r) from UAV-RGB.

Research question (a): What is the relationship between DBH and CPA?

2. To assess the accuracy of the automatic segmented Crown Projection Area (CPA-rs) from UAV (RGB and multispectral) and Pleiades at different spatial resolution and band combinations.

Research question (a): What is the accuracy of the CPA-rs compared with CPA-r.

3. To estimate and assess the accuracy of the DBH using automatic segmented Crown Projection Area from UAV (RGB and multispectral), and Pleiades.

Research question (a): What is the accuracy of the modelled Diameter at Breast Height (DBH-est) at different spatial resolutions and band combinations compared to field measured DBH.

4. To determine if the differences in DBH derived from UAV (RGB and multispectral) and Pleiades will lead to significant differences in biomass estimations.

Research question (a): Does the estimated Aboveground Biomass from UAV (RGB and multispectral) and Pleiades differ significantly from the field estimated Aboveground Biomass?

1.6.3. Hypothesis

1. Ho: The two reference CPA (manually digitized from orthophoto and plot Nadir images) have the same relationship (R^2 and RMSE) with field measured DBH.
   H1: The manually digitized CPA from orthophoto has a better relationship (R^2 and RMSE) with field measured DBH than manually digitized CPA from Nadir plot images.

2. Ho: Automatic segmented CPA from UAV (RGB and multispectral) and Pleiades have the same relationships (R^2 and RMSE) with reference CPA.
   H1: Automatic segmented CPA from UAV (RGB and multispectral) and Pleiades have different relationships (R^2 and RMSE) with reference CPA.

3. Ho: Modelled DBH from UAV (RGB and multispectral) and Pleiades have the same relationship (R^2 and RMSE) with field measured DBH.
   H1: Modelled DBH from UAV_ multispectral are more accurate (R^2 and RMSE) than UAV_RGB and Pleiades.

4. Ho: There is no significant difference between estimated AGB and field measured AGB.
   H1: There is a significant difference between estimated AGB and field measured AGB.

2.0. MATERIALS AND METHODS

2.1. Study area

The Haagse Bos is a semi-natural forest and has landscape and flora conditions which are characterized by different tree species (Oak, Beech, Birch, Larch, Douglas Fir, Scot's pine, Spruce), different forest types (broadleaf deciduous trees, coniferous trees, and mixed trees) with different canopy density (open, medium, and high forest canopy densities). These different unique characteristics make it a suitable study area for this research. The forest is located in Enschede near Losser in the province of Overijssel, the Netherlands, and lies between latitude 52°16'39.21" N and 52°14'55.22" N and longitude 6°56'26.80" E and 6°58'24.90" E (Haagse Bos (Overijssel) - Wikipedia, 2018; Mohren & Vodde, 2006). The study area map is shown in figure 2.

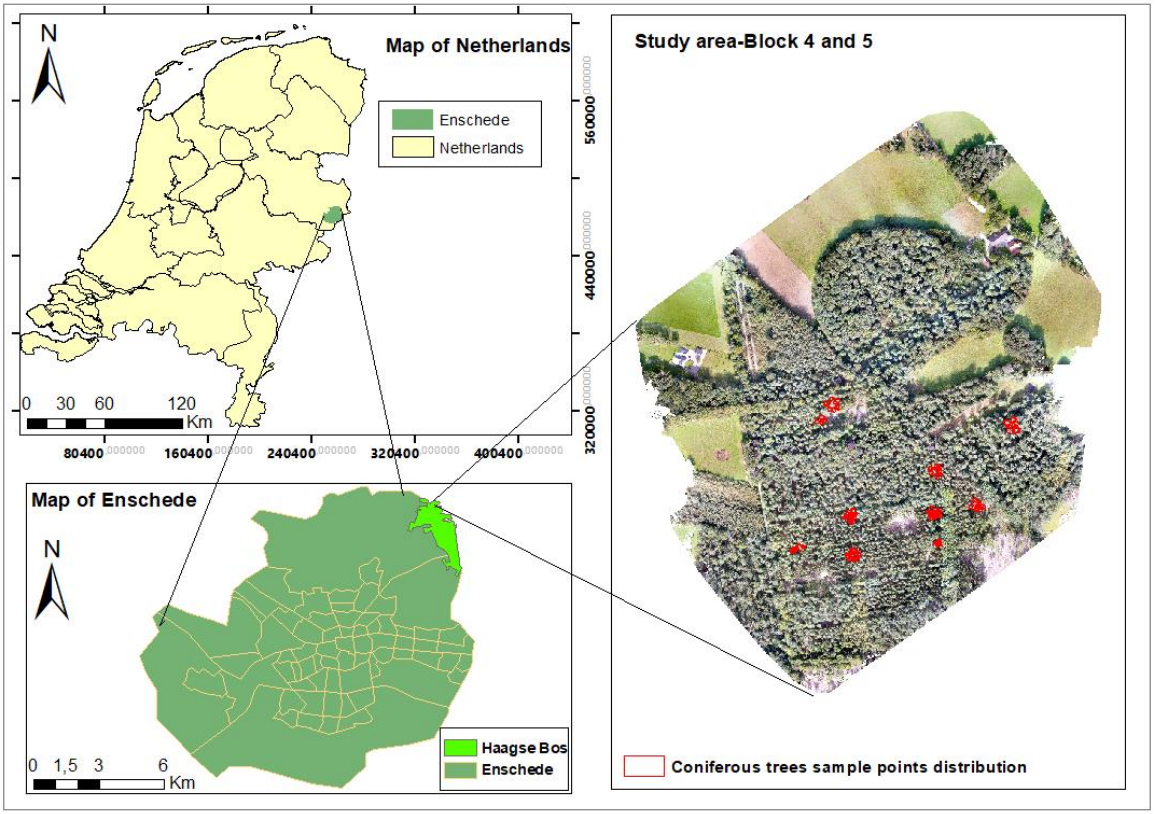

Figure 2: Study area location

2.2. Sampling Design used

The following criteria were considered in the sampling design; The flight areas were selected based on the availability of the open space for ground control points and as well as incorporation of the following required different forest structure variations; medium coniferous canopy density, high coniferous canopy density. High canopy density refers to forest type where tree crowns are interlocking, whereas medium canopy density refers to forest type where individual tree crowns are barely touching each other (López García, Prado Molina, Manzo Delgado, & Peralta Higuera, 2016). Considering all these parameters needs a non-probability method where the sample plot choice is based on the researcher's judgment. Such kind of non-probability method was defined by Etikan (2016) as purposive sampling. The paper further stated that in this kind of method, a researcher selects elements to be included in the sample based on what is needed in the topic of study. Therefore, after an initial stratification on forest type, a purposive sampling design was used for this research for data collection in the field.

2.3. Plot size

A research which was conducted to study the combined effect of field plot size and LiDAR density on the estimation of forest parameters observed that plot size has a huge effect on the estimation of forest parameters; the paper concluded that minimum circular plots of 500 – 600 m^2 are sufficient for estimation of AGB as larger plot sizes do not significantly improve the accuracy, but increase fieldwork cost (Ruiz, Hermosilla, Mauro, & Godino, 2014). Circular plots are better than square or rectangular plots because they only require a single control point compared with the four points needed for square and rectangular plots. Furthermore, it is very easy to decide on trees close to the plot boundary regarding which trees to include or exclude as circular plots have the shortest plot perimeter (Mcroberts, Tomppo, & Czaplewski, 2015; Paul, Kimberley, & Beets, 2019). Mauya et al. (2015) also added that circular plots are easy to outline and usually less prone to errors. Therefore, in this research, 500 m^2 (radius 12.62 m) circular plots were used in flat terrain for field data collection.

2.4. Field equipment

Different field instruments and equipment were used in the field to measure forest parameters for the estimation of forest AGB. The fieldwork was carried out between September 5, 2020, and October 10, 2020. The field instruments used are listed in table 1.

Table 1: Field instruments used.

S/N	Instruments/equipment	Application
1	Diameter tape (5 meters)	Diameter at Breast height (1.3 m) measurement
2	Measuring tape (30 meters)	Tree distance from the plot centre
3	Differential Global Positioning System (DGPS)	GCPs coordinate acquisition.
4	Garmin GPS	Navigation and positioning
5	Forest Range finder	Tree distance from the plot centre
6	Chalk	Marking trees
7	GLAMA	Canopy closure/openness estimation

2.5. Field data collection and processing

Various field data which were collected are listed in table 2 and 3. Field measured DBH (DBH-f) is a diameter of a tree stem mostly measured at 1.3 m height from the ground (Brokaw & Thompson, 2000). Trees with DBH less than 10 cm were not considered because their biomass contribution is relatively small (Cummings, Boone Kauffman, Perry, & Flint Hughes, 2002; Hughes, Kauffman, & Jaramillo, 2000). DBH-f (greater than/equal to 10cm) was used to estimate field above ground biomass (reference biomass-AGB-f). Plot centre coordinates, tree distance from the plot centre and bearing of each tree were used to locate all the trees within the plots. Appendix 4 shows the data sheet used for tree parameters data collection.

Table 2: Collected field data.

S/N	Data	Source
1	UAV RGB Images	Phantom 4 (RGB camera)
2	UAV multispectral Images	Phantom 4 (Sequoia MSS camera)
3	Tree DBH	Field measured
4	Tree Location	Field measured
5	Plot centre coordinates	Field measured
6	Distance and bearing of each tree from the plot centre	Field measured
7	Canopy density (Medium and Dense – 31 plots)	Field measured
8	Tree species (coniferous)	Field identification

Table 3: Types and number of coniferous tree species collected.

Family	Species	Count (Trees)	Percentage
Pinaceae	Douglas fir	224	66.27
	European spruce	74	21.89
	Larch	29	8.58
	Scotch Pine	11	3.25
	Total	**338**	**100**

2.6. UAV flight planning

The images were collected using Phantom 4 (1/2.3" CMOS camera (RGB) and Sequoia MSS camera). The mission planning was done using the pix4D capture app, where flight parameters such as speed, angle, front and side overlap, and flight height were appropriately set.

Various research shows that side and front overlaps are important for overall forest canopy sampling. A clear sky, 80% side photographic overlap, and 80 m of flying height result in a very high correlation of accurate forest parameters estimation (Dandois, Olano, & Ellis, 2015). It was also noted that the higher the front overlaps, the higher the possible views and view angle, leading to higher canopy penetration to the forest floor with high accuracy of forest parameter estimation. It was further noted that point cloud density is affected by view angle as point matching stability begins to decrease rapidly when the view angle exceeds 20 degrees off Nadir, which leads to a reduced sampling of the forest canopy, thereby increasing the errors in the estimation of forest canopy parameters (Hirschmugl, Ofner, Raggam, & Schardt, 2007; Ofner, Hirschmugl, Raggam, & Schardt, 2006 and Dandois et al., 2015). Flight height is also a very important parameter of the UAV flight plan because it affects the spatial resolution of the UAV, as discussed earlier in section 1.2. above. Therefore, all these issues discussed above were taken into consideration to come up with an appropriate flight plan parameter combination in table 4 and figure 3.

Table 4: Flight plan parameters

S/N	Parameters	Value
1	Speed	Slow
2	Angle	Nadir (90°)
3	Front overlap	90%
4	Side overlap	80%
5	Flight height	100-110 meters
6	Flight pattern	Double grid

Figure 3: UAV flight plan.

2.7. UAV data acquisition and processing

The images were acquired in August and September 2020 using Phantom 4 drone carrying two sensors (RGB and MS). The acquired images were processed to generate a 3D point cloud and orthophoto using Pix4D mapper software. This software uses the principle of photogrammetry to process the UAV images in three steps: image orientation, 3D point cloud generation, and orthophoto generation. The software uses the ground control points (GCP) and checkpoints for image registration; GCPs are used for absolute orientation of the UAV images, whereas checkpoints are used for accuracy assessment as shown in figure 4 and appendix 2 (to be added) (Westoby, Brasington, Glasser, Hambrey, & Reynolds, 2012).

Summary

Project	B45
Processed	2020-09-29 10:58:03
Camera Model Name(s)	FC330_3.6_4000x3000 (RGB)
Average Ground Sampling Distance (GSD)	4.49 cm / 1.77 in
Area Covered	0.575 km^2 / 57.5429 ha / 0.22 sq. mi. / 142.2651 acres
Time for Initial Processing (without report)	53m:49s

Quality Check

Images	median of 58179 keypoints per image	✓
Dataset	1470 out of 1470 images calibrated (100%), all images enabled	✓
Camera Optimization	0% relative difference between initial and optimized internal camera parameters	✓
Matching	median of 5730.64 matches per calibrated image	✓
Georeferencing	yes, 9 GCPs (9 3D), mean RMS error = 0.011 m	✓

Figure 4: Summary of Pix4D photogrammetry initial report.

The final product of the photogrammetry process was the RGB – orthophoto with a spatial resolution of 4.5 cm from phantom 4 camera and individual bands (Red, Green, red edge and Near-infrared) orthophotos from sequoia camera with a spatial resolution of 11cm. Near-infrared band orthophoto and RGB - orthophoto were resampled to 10 cm spatial resolution and composited to produce a multispectral orthophoto with RGB-NIR bands with 10 cm spatial resolution, which was later resampled to 20 cm, 30 cm, 40 cm and 50 cm spatial resolutions. Resampling refers to changing the pixel dimensions of an image, as shown in figure 5.

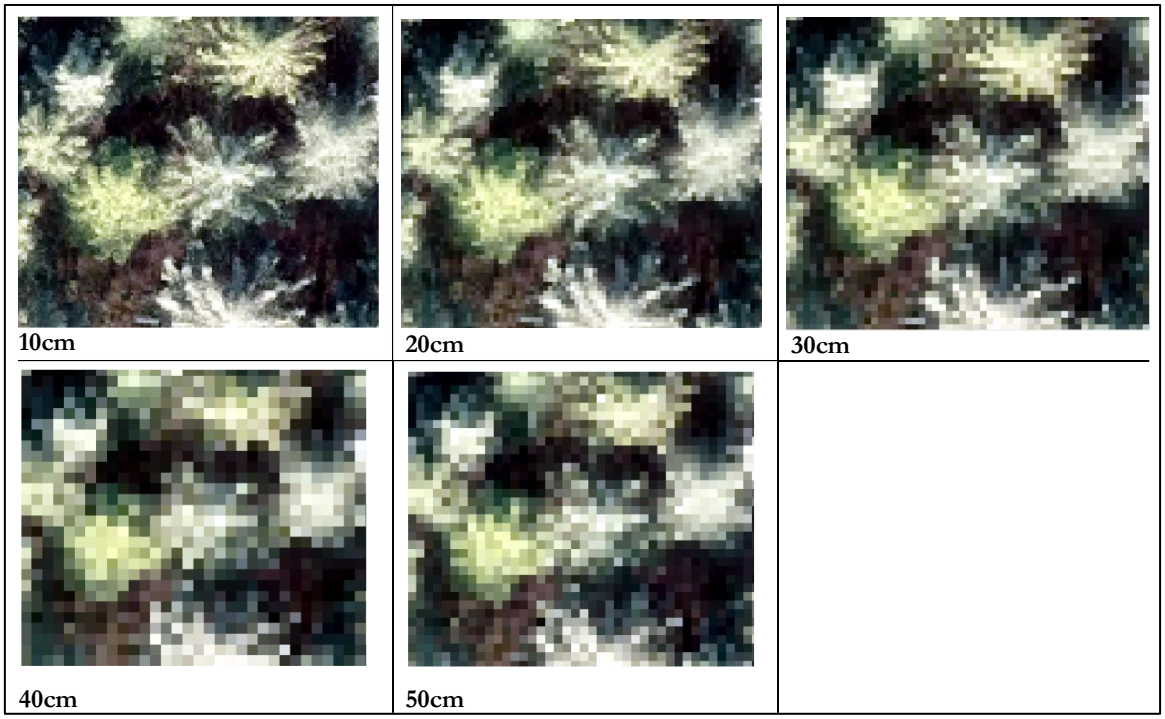

Figure 5: Resampled images in true colour composite (1,2,3-RGB)

Baboo & Devi (2010) in the Coimbatore district, India, evaluated three resampling methods (Nearest Neighbour, Bilinear interpolation, and Cubic Convolution) to find out the effect of the three methods on the image pixel values. The paper concluded that: (a) Nearest neighbour methods preserve the original values, but the results can be blocky; therefore, this method can be best used for categorical data like classification of land use or slope. (b) Bilinear interpolation takes a 2x2 window with a weighted average, leading to producing an output with values that are slightly different from the nearest input but always within the range; because of this, it should not be used for categorical values but continuous data. (c) The Cubic convolution method takes a 4x4 window with a weighted average, leading to producing an output with values outside the input values; this method does well for smoothing continuous data. This research dealt with continuous data such as tree CPA and AGB values and needed values within the range even after resampling was performed on the images; therefore, the Bilinear interpolation method was used. The sample plots of interest were clipped from the resampled orthophotos in ArcMap using a 12.6m buffer (500 m^2 plot size) from the plot centre coordinate; the clipped plots were loaded in eCognition for Object-Based Image Analysis (OBIA) to generate individual tree CPA (CPA-UAV) at different spatial resolution and band combinations. Clipped individual plots were used in the segmentation processing to reduce computational time.

2.8. Very High-Resolution (VHR) imagery data

A proposal was submitted to European Space Agency (ESA) on August 24, 2020, requesting for Pleiades satellite imagery (50 cm spatial resolution). Two suitable Pleiades images of August 22, 2019, and October 14, 2018, were available in the ESA archive. An orthorectified Pleiades satellite imagery of August 22, 2019, with four spectral bands (R, G, B, and NIR)) was acquired from Airbus through ESA and used in this research. Pleiades image was acquired a year earlier than UAV images; therefore, 13.2 mg/hectare (ha) of AGB was added to the mean AGB-est per hectare (ha) of Pleiades because maximum temperate forest annual carbon sequestration is 6.6 mg/ha (2 * Carbon = AGB) (Valentini et al., 2000).

2.8.1 Pre-processing of satellite image

Before image segmentation, noise (spatial image variations) reduction through image smoothing was applied to the image to avoid over-segmentation. A mean filter with 3 x 3 window sizes i.e., low pass filter (3x3 LPF) was applied to the image in Erdas Imagine 2020. This filter was used because it produces more homogenous image segments by smoothing the image data to eliminate noise, thereby avoiding over-segmentation (Gougeon & Leckie, 2006; Platt & Schoennagel, 2009).

2.9. Object-Based Image Analysis (OBIA)

Object-based image analysis (OBIA) is an image analysis technique used to identify and classify objects through a process of pattern recognition. Once an image raster is segmented, the object can be classified using analyst defined rules. Features such as shape, size, and texture and not just spectral features are used to drive the classification (Halabisky, Babcock, & Moskal, 2018; Veljanovski, Kanjir, & Oštir, 2011). OBIA comprises of two main parts, which include image segmentation: where an image is divided into adjacent and homogenous groups of pixels to form image objects based on homogeneity criteria, and Image objects classification based on spectral, textural as well as shape information (Baral, 2016).

Image segmentation

During the segmentation procedure, the region-based segmentation (multi-resolution segmentation) technique was applied. This algorithm was used because it creates homogeneous objects such as tree crowns; during the process of segmentation it obtains both an initial over-segmentation and under-segmentation of the image; after that, it merges or splits the neighbouring segments which are similar or different; this process continues until there are no more segments that should be merged or split thereby improving the accuracy of image segmentation (Bins, Fonseca, Erthal, & Ii, 1996). Furthermore, multi-resolution segmentation algorithm can generate segments at different spatial resolutions. It ensures that any object smaller than the set spatial resolution is not identified during the segmentation process, while items larger than the provided spatial resolution are fragmented into pixel (Hossain & Chen, 2019; Wang, Jensen, & Im, 2010).

Segmentation combinations: Image Band weights (Band combinations)

Image band weights indicates the level to which the bands in the image influence the segmentation process, and it ranges between 0 (lowest/no effect on segmentation) to 4 (highest/maximum effect on segmentation). The higher the value assigned to an image band; the more weight was assigned to that bands' pixel information during the image segmentation process (*Definiens Developer XD 2.0.4 User Guide*, 2012). Green and NIR bands were given the highest weight in the combination weights used. Green and NIR were given maximum weights because Xu et al. (2020) observed a significant difference in the reflectivity and high separability of different forest tree species in green and near-infrared bands of the UAV-based data. The weights were assigned to different bands as shown in table 5.

Table 5: Band combinations

Bands	Sensor	Image band weights	Comment
R, G, B, NIR	UAV_RGB	1,4,1,0	This means that the green band influenced the segmentation process.
	UAV_MS	1,1,1,4	A near-infrared band influenced the segmentation process.
Pleiades	R, G, B, NIR	1,1,1,4	The near-infrared band influenced the segmentation process.

Scale parameter

The scale parameter is spatial resolution dependent (Hay, Castilla, Wulder, & Ruiz, 2005). This meant that different image spatial resolutions and band combinations used in this research required different scale parameter value to produce meaningful segments. The different rule set segmentation scale parameter values that were determined by trial and error and used in this research are shown in the appendix 1.

Composition of homogeneity criterion

Composition of homogeneity measures the homogeneity or heterogeneity of an image object. It is calculated as a combination of the spectral colour and shape properties of an image. The homogeneity criteria can be adapted by weighing shape and compactness criteria. The shape criterion has a value between 0 to 0.9; it determines to what extent the image resolution influences the segmentation compared to colour. Compactness criterion also has a value of 0 to 0.9; it determines to what extent the spectral colour (band combination) influences the segmentation compared to shape (*Definiens Developer XD 2.0.4 User Guide*, 2012). Therefore, in this research, both shape and compactness were set at 0.5 so that both spatial resolution and spectral colour had an equal effect on the image segmentation.

Watershed transformation.

After multi-resolution segmentation, the watershed transformation was performed to split the overlapping tree crowns into individual tree crowns based on the suitable splitting threshold that was set at different resolution and band combinations. The watershed transformation algorithm calculates an inverted distance map based on the inverted distances for each pixel to the image border. After that, the minima are flooded by increasing the level; where the individual catchment basins touch each other, the image objects split (*Definiens Developer XD 2.0.4 User Guide*, 2012; Baral, 2016).

Morphology

Morphology operation was undertaken to smoothen the borders of the image objects through two pixel-based operations, namely, opening image object which removes the pixel that is isolated from an image object and closing image objects which adds surrounding isolated pixel to an image object. Closing image object operation was performed in this research, and it helped in defining the shape and size of the mask (structuring element on which the morphology is based), like a circular mask that defines the tree's circular crown. To finally get an individual tree crown (CPA-rs), the undesired objects were removed. The undesired objects include very tiny objects (usually with less than 16 pixels), whose reflectance might not be detected in a dense or medium forest (*Definiens Developer XD 2.0.4 User Guide*, 2012; Baral, 2016).

Export

Segmented tree polygons were exported, and the areas of the individual segmented polygons were calculated in ArcMap 10.7.1.

2.10. Descriptive Statistics and Normality Tests

To reach a meaningful statistical conclusion, descriptive statistics, and normality tests for diameter at breast height (DBH) were performed. Assumption of the normality is supposed to be followed regardless of the sample size; otherwise, the statistical prediction of the intervals is inaccurate; the fundamental element of the normality assumption states that before running certain statistical tests or regression, the data to be used should roughly fit a bell curve shape (Mishra et al., 2019).

2.11. Reference Crown Projection Area (CPA)

Firstly, the plot Nadir UAV images were selected and georeferenced, 165 tree crowns were digitized, and the area of individual tree crowns was calculated in ArcMap. secondly, 173 tree crowns from the original Orthophoto resolution (4.5 cm) were as well digitized, and the areas of individual tree crowns were calculated in ArcMap. In total 109 (same trees) digitized Nadir image tree crowns, and digitized orthophoto tree crowns were matched with their respective field measured DBH for regression analysis.

Regression analysis was performed to determine the relationship between the two reference CPA and the field measured DBH to answer research question 1a. The resulting R^2 values were used to determine the better reference CPA. R^2 is the percentage of response variable variation explained by a model. It is a statistical measure of how close the data is to the fitted regression line, and it is always between zero and hundred percent. The higher the R^2 value, in general, the better the model fits the data (Waterman, 2014). The operation described above is summarised in figure 6.

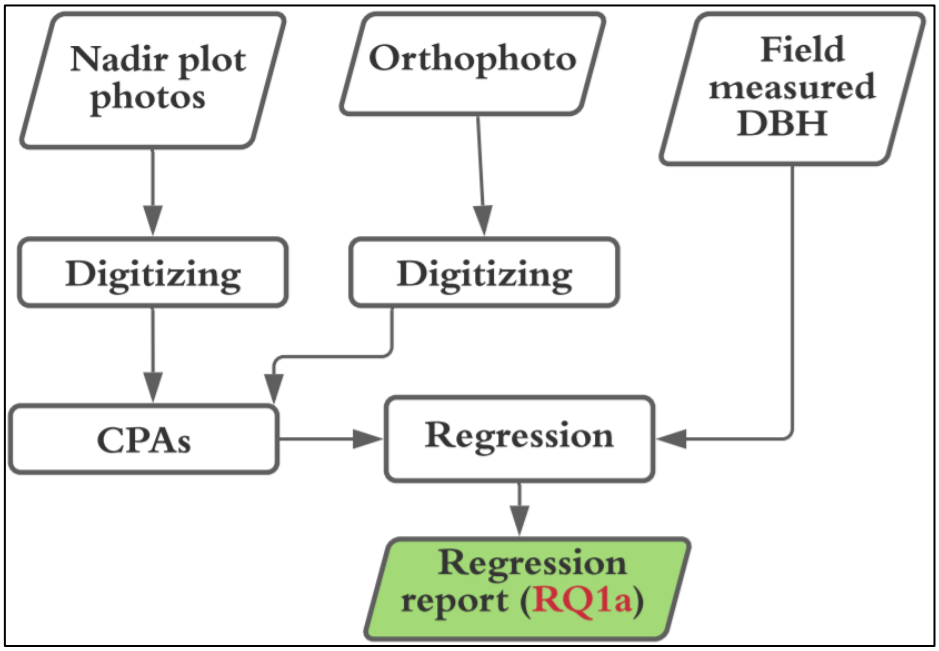

Figure 6: Procedure for selecting the reference CPA: (RQ 1a) research question 1a.

2.12. Segmentation accuracy assessment

The multiresolution segmentation process partitioned the image objects that resulted in a one-to-one mapping between each segment in the image and each object in the study area as described by Troya-Galvis, Gancarski, Passat, & Berti-Equille (2015). Segmentation errors are classified into two: over segmentation and under segmentation. Over segmentation is where corresponding segments are too small compared to the reference objects while under segmentation is where corresponding segments are larger than the reference objects as shown in figure 7. Over segmentation is preferred instead of under segmentation as it is easier to join small segments to form a large segment than splitting a region into smaller segments. Segmentation errors range from 0 to 1; Zero (0) error indicates a perfect match of the image segment and reference object (Clinton, Holt, Scarborough, Yan, & Gong, 2010; Troya-Galvis et al., 2015).

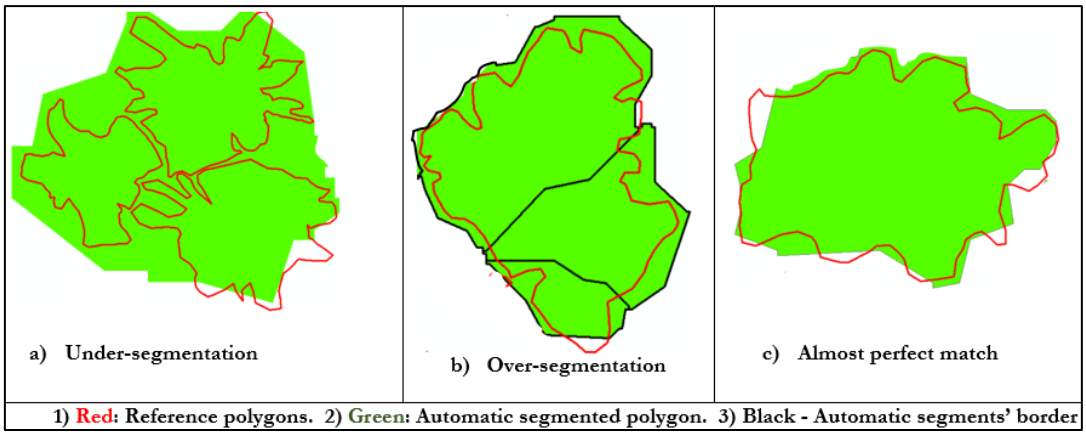

Figure 7: Segmentation accuracy assessment

The three-step approach was used for segmentation accuracy assessment as proposed by (Clinton et al., 2010).

Step 1: Over segmentation $= \mathbf{1} - \frac{Area(xi \cap yj)}{Area\ (xi)}$ ……...… equation 1

Step 2: Under segmentation $= \mathbf{1} - \frac{Area(xi \cap yj)}{Area\ (yj)}$ ……..……..…… equation 2

Step 3: total error detection (Di) $= \sqrt{\frac{(Over\ segmentation^2 + \text{Under } segmentation^2)}{2}}$ …… equation 3

Where:
$\cap$ = Intersect,
x_i = Automatic segmented polygon,
y_j = Reference polygon.

To find the relationship between the automatic segmented CPA-rs and reference CPA-r, which is research question 2a, linear regression analysis was executed.
The resulting R^2 and RMSE were used to determine the best correlation between automatic segmented CPA-rs at different spatial resolution and band combinations, and reference CPA-r as shown in figure 8.

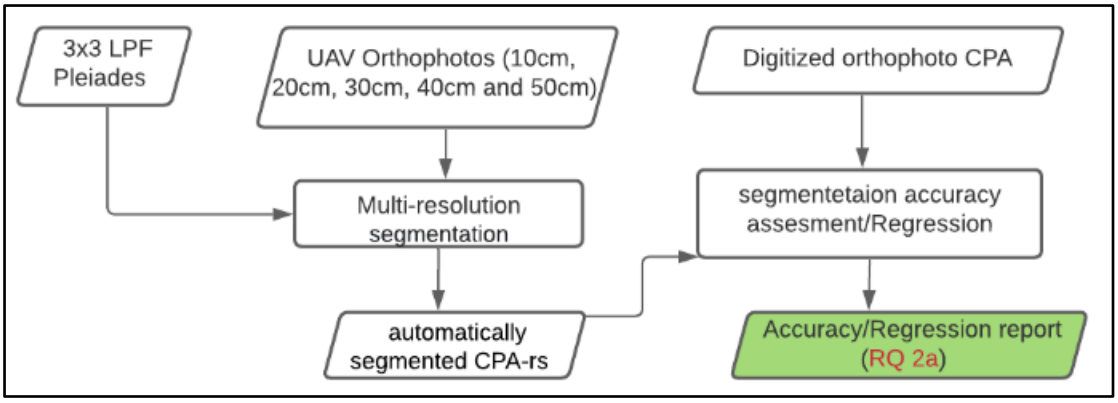

Figure 8: Procedure for CPA segmentation accuracy assessment: (RQ 2a) research question 2a.

Root mean square error (RMSE) measures the discrepancy between the values predicted by a model and the actual values. The lower the RMSE, the more accurate the estimates are. The RMSE was calculated using equation 4 (Gopinathan, 1988).

$$\textbf{RMSE} = \sqrt{\sum_{i=1}^{n} \frac{(\hat{y}_i - y_i)^2}{n}} \quad \text{.....equation 4}$$

Where:

$\hat{y}_i$ = Modelled values.

y_i = Observed values.

N = Number of observations

i = Variables.

The RMSE was normalised (relative RMSE) by dividing it with the average value of the observed data (Li, Tang, Wu, & Liu, 2013).

Furthermore, the established relationship between reference CPA-r and field measured DBH-f in section 2.11, was used to model the DBH (DBH-est) using automatically segmented CPA-rs at different resolution and band combination. To answer research question 3a, DBH-est were matched with their respective DBH-f, and linear regression analysis was performed as shown in figure 9; the resulting R^2 and RMSE were used to determine the most accurate modelled DBH-est.

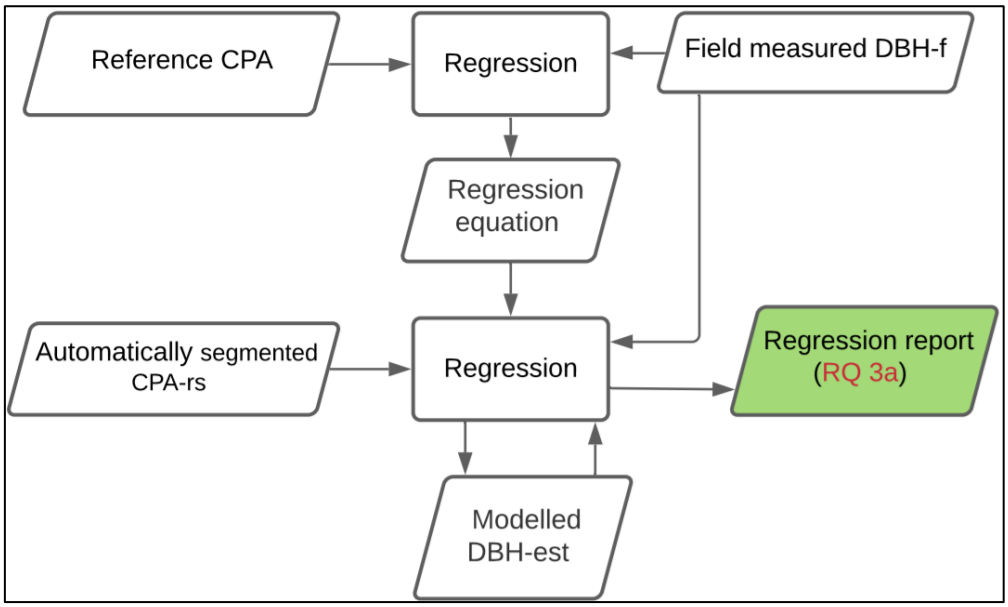

Figure 9: Procedure for DBH modelling: (RQ 3a) research questions 3a.

2.13. Biomass Calculation

Commonly used mathematical model for biomass calculation that takes the form of a power equation as described by Zianis & Mencuccini (2004) was adopted as shown in equation 5.

$$Y = b0 * DBH^{b1}$$ ……..……. equation 5

Where:
Y = Aboveground Biomass (kg),
DBH = Diameter at Breast Height (cm),
b0 and b1 = Scaling coefficients.

Muukkonen (2007) analysed various allometric equations to provide a new generalized allometric equation's scaling coefficient that should provide a consistent and unbiased basis for evaluating forest biomass for the most common coniferous tree species across regional boundaries in Europe. The paper established that for the most common temperate coniferous species, bo and b1 is equal to 0.255 and 2.174 for European spruce and 0.158 and 2.237 for scots pines. The DBH was used as the only AGB predictive variable because it is the most common, easiest, and accurate variable to measure in the field (Pastor, Aber, & Melillo, 1984). This research applied the European spruce allometric equation for all the coniferous species under study as shown in equation 5. This is because the equation provides reliable and impartial results at both local and region scale across European coniferous forest (Muukkonen, 2007), and all the species (table 3) under study belong to the same family (Pinaceae). No suitable local coniferous allometric equation that uses DBH as the only AGB predictive variable was found. However, the implication of applying a generalized allometric equation of one species to all species under study is discussed in section 4.5.

2.14. Field measured and Modelled AGB.

Field measured AGB-f, which is the reference AGB, was calculated by using the individual tree DBH measured from the field whereas modelled AGB (AGB-est) was calculated by using the modelled DBH (DBH-est) and the allometric equation as described in equation 5. Figure 10 describes the procedure taken in AGB calculation.

2.15. Comparing field measured and modelled AGB and significance test.

Comparing of field measured and modelled AGB, and the subsequent significance test analysis was done to find out the differences between the estimated AGB-est from UAV and Pleiades at different resolutions and band combinations, and the field measured AGB-f. The resulting biomass differences indicated how much carbon is lost or gained by changing the imagery's spatial resolution from higher to lower. To establish if the AGB-est differs significantly from AGB-f, the means of the two data sets were compared using a two-sample t-test. The results with a t-statistic value greater than the t-critical value meant that the two data sets were significantly different and vice-versa. The analysis was undertaken as shown in figure 10.

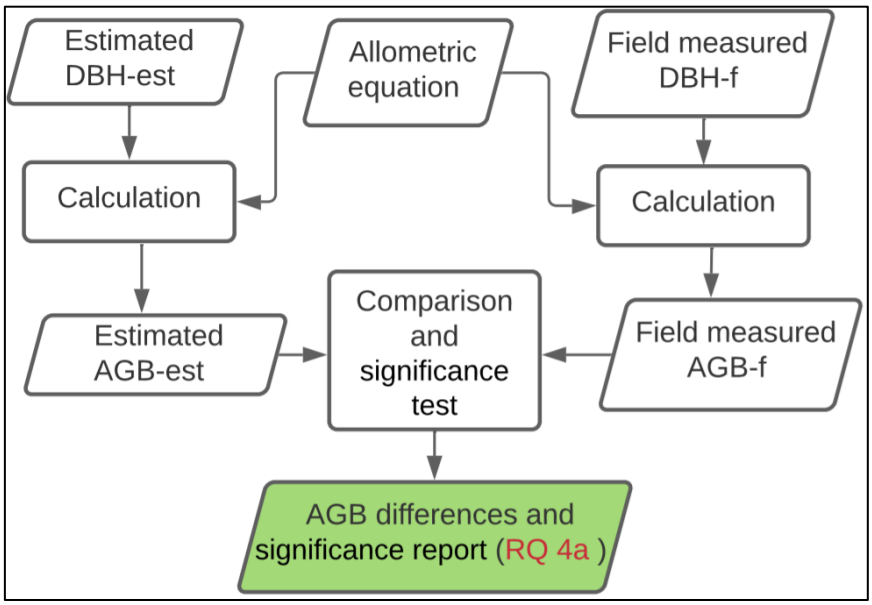

Figure 10: Procedure for AGB estimation: (RQ 4a) research questions 4a

2.16. Summary of research methods

The research method is summarised in the following four parts:

1. Field data collection and processing (section 2.5)
2. UAV data acquisition and processing (sections 2.7)
3. VHR satellite imagery acquisition and processing (sections 2.8)
4. Biomass calculation, comparing results and significance test (sections 2.13 to 2.15)

The analysis of the four components described in figures 6, 8, 9 and 10 are integrated in figure 11.

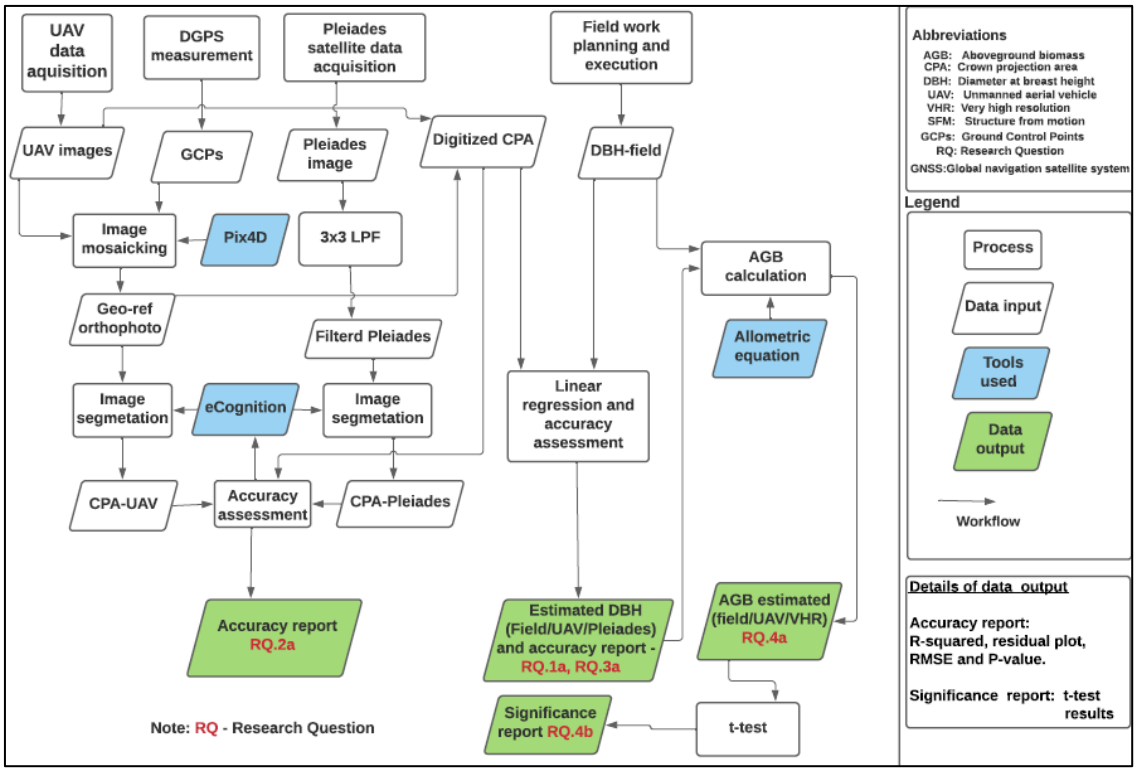

Figure 11: Workflow summary of the research methods.

3. RESULTS

3.1. Descriptive Statistics and Normality Tests for Diameter at Breast Height data.

In total, 338 DBH samples from 20 plots of coniferous forest (10 dense and 10 medium forests) were tested for normality, as shown in figure 12. The data showed a DBH of 10.8 cm and 59.6 cm as lower and upper limits of the Box-Whisker-plot, respectively. In order to make accurate conclusions in the subsequent analysis, all the DBH samples (12 samples) with values above the whisker's plot upper limit (59.6 cm) were treated as potential outliers, and were not considered in the model development (Li, Feng, Li, & Liu, 2016). The data further showed a non-normal distribution of samples with a positive skewness as shown in the histogram in figure 12a. The skewness observed was due to the DBH values falling outside the Box-Whisker-plot's upper limit (59.6) and no values falling below the lower limit (10.8 cm) as no DBH below 10 cm was measured from the field (section 2.5).

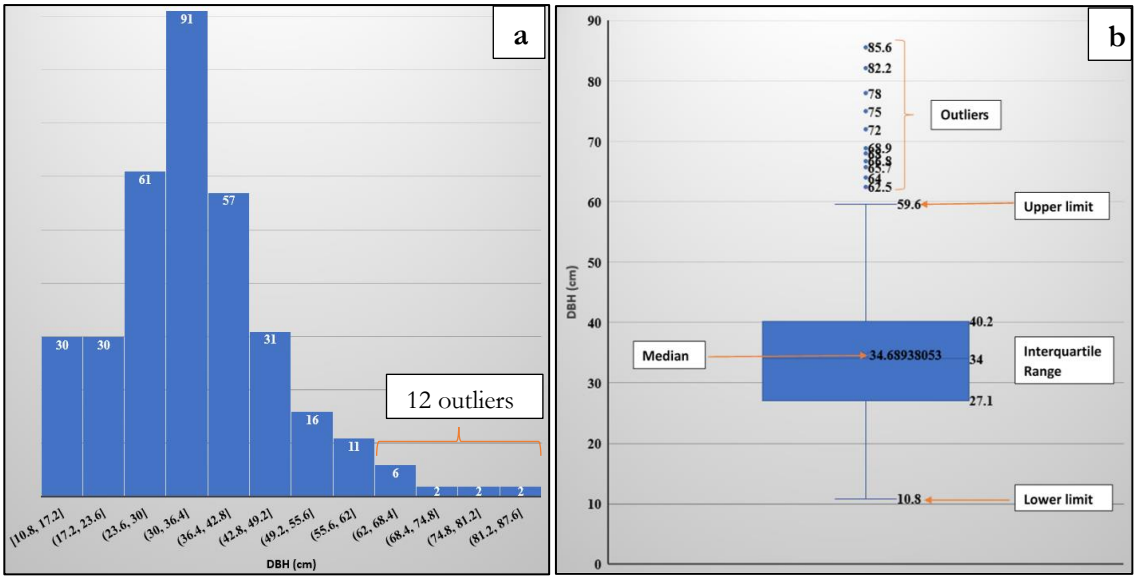

Figure 12: a) Histogram and b) Box-Whisker-plot of the field measured DBH samples

3.2. Relationship between reference CPA-r and field measured DBH-f

The digitized CPA from Nadir plot images and the orthophoto (UAV_RGB) with the original resolution (5 cm) were considered as reference CPA (CPA-r). An exponential relationship was observed between the field measured DBH-f and the two reference CPA-r. A total of 109 manually digitized CPAs from Nadir plot images and the orthophoto (same trees) were selected and matched with their respective 109 filed measured DBH samples. 57 samples (same trees of digitized Nadir photo and orthophoto CPAs) were used for model development, whereas 52 samples were used for model validation. The R^2 for the relationship between field measured DBH and manually digitized Orthophoto_UAV_RGB CPA was 0.731 with RMSE of 6.906 m^2; whereas, for manually digitized Nadir image CPA the relationship with field measured DBH had a R^2 of 0.584 with RMSE of 9.797 m^2 as shown in figures 13 and 14. Therefore, orthophoto digitized CPA was selected as a reference CPA, the regression equation in figure 14a was used in the subsequent analysis for DBH-est modelling.

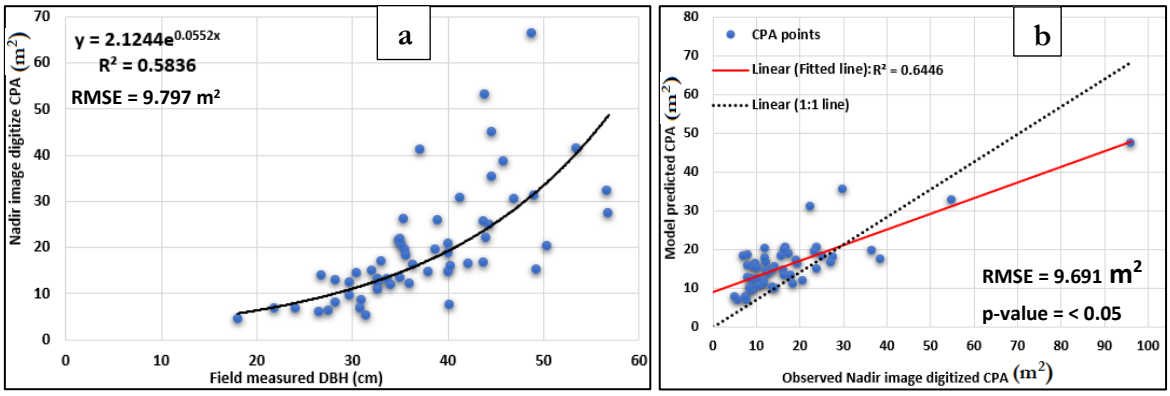

Figure 13: Relationship between field measured DBH and UAV_RGB Nadir image digitized CPA: a) model development b) model validation.

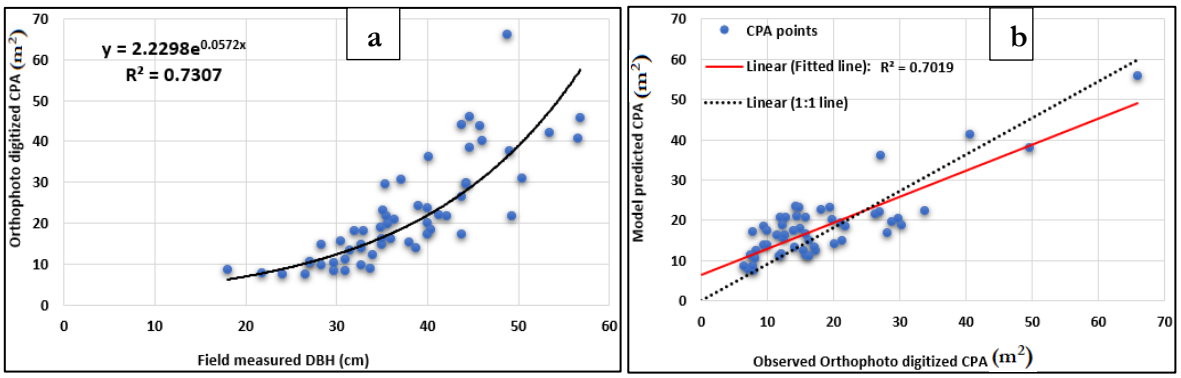

Figure 14: Relationship between field measured DBH and UAV_RGB Orthophoto digitized CPA: a) model development b) model validation.

3.3. Relationship between manually Orthophoto segmented CPA-r and automatic segmented CPA-rs

3.3.1. Segmentation accuracy assessment

The orthophoto (UAV_MS) at 10 cm spatial resolution had the highest segmentation accuracy of 84.63% (total error = 0.154); the lowest accuracy of 75.16% (total error = 0.248) was observed in UAV_RGB at 50 cm. The rest of the segmentation accuracy results (for both UAV_MS and UAV_RGB and the Pleiades) at different spatial resolution, are shown in tables 6 and 7.

Table 6: Summary of UAV orthophoto segmentation accuracy assessment results

Sensor	Resolution	Band weight	Over segmentation	Under segmentation	Total error	Percent
UAV (RGB/MS)	10cm	1,1,1,0,4	0.2	0.0837	0.15	84.63
		1,4,1,0,0	0.235	0.107	0.18	81.77
	20cm	1,1,1,0,4	0.256	0.0693	0.19	81.24
		1,4,1,0,0	0.309	0.069	0.22	78.06
	30cm	1,1,1,0,4	0.272	0.055	0.2	80.36
		1,4,1,0,0	0.291	0.082	0.21	78.61
	40cm	1,1,1,0,4	0.281	0.056	0.2	79.74
		1,4,1,0,0	0.308	0.09	0.23	77.31
	50cm	1,1,1,0,4	0.341	0.035	0.24	75.79
		1,4,1,0,0	0.343	0.0774	0.25	75.157
UAV_MS-Band weight: 1,1,1,4 - segmentation process was influenced by near-infrared band.						
UAV_RGB-Band weight: 1,4,1,0 - segmentation process was influenced by green band.						

Table 7: Pleiades segmentation accuracy assessment results

Sensor	Resolution	Band weight	Over segmentation	Under segmentation	Total error	Percent
Pleiades	50cm	1,1,1,4	0.558	0.386	0.48	52.04
Band weight: 1,1,1,4 - segmentation process was influenced by near-infrared band.						

In addition, it was observed that segmentation accuracy depended on UAV image resolution, as shown in figure 15, the lower the resolution, the lower the segmentation accuracy, and vice versa. The trend was similar in both UAV_MS, and UAV_RGB influenced segmentation process.

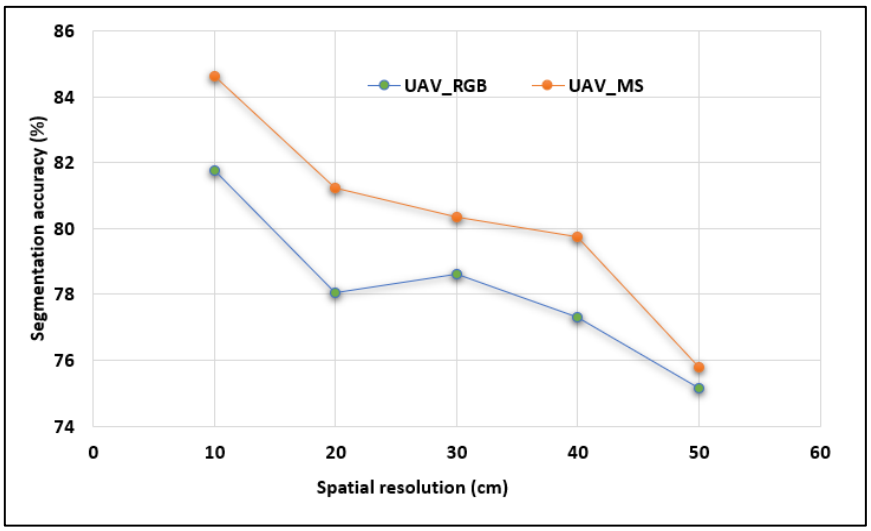

Figure 15: Effect of UAV image resolution on segmentation accuracy.

UAV_MS-Band weight: 1,1,1,4 (R,G,B,NIR): segmentation process was influenced by near infrared band.
UAV_RGB-Band weight 1,4,1,0 (R,G,B,NIR): segmentation process was influenced by green band.

3.3.2 Linear regression

The relationship between automatic segmented CPA-rs and manually digitized CPA-r at different spatial resolution and band combinations was analysed for UAV orthophoto and Pleiades satellite imagery. 109 CPA-rs from the same locations (same trees) were selected from all resolutions and band combinations. The selected CPA-rs were then matched with their respective orthophoto manually digitized CPA-r. For UAV, it was observed that the highest R^2 of 0.822 was obtained at 30 cm resolution with segmentation band weights of 1,1,1,4 (UAV_MS), while the lowest R^2 of 0.4 was observed at 50 cm resolution with segmentation band weights of 1,4,1,0 (UAV_RGB) as shown in figure 16 and table 8.

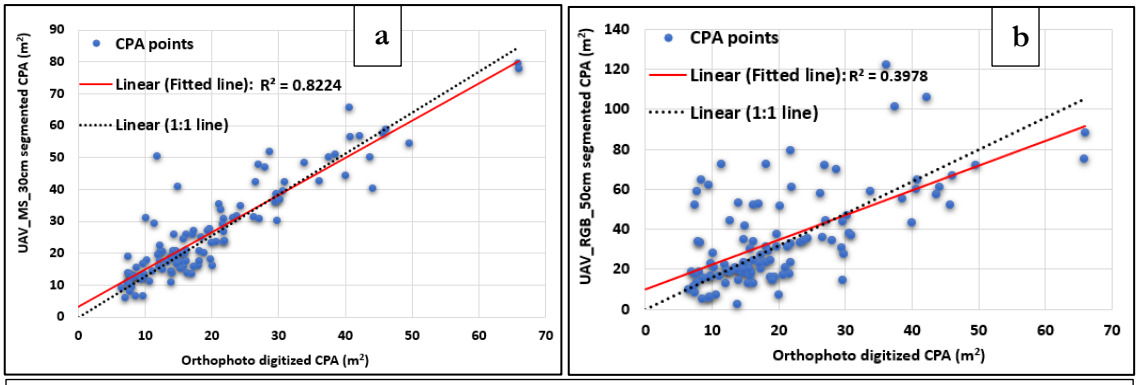

UAV_MS-Band weight: 1,1,1,4 (R,G,B,NIR): segmentation process was influenced by near infrared band.
UAV_RGB-Band weight 1,4,1,0 (R,G,B,NIR): segmentation process was influenced by green band.

Figure 16: Relationship between UAV orthophoto automatic segmented CPA and manually digitized CPA: a)UAV highest R^2, b) UAV lowest R^2

For Pleiades (50 cm resolution), the R^2 of 0.405 was observed with segmentation band weights of 1,1,1,4 as shown in figure 17 and table 9.

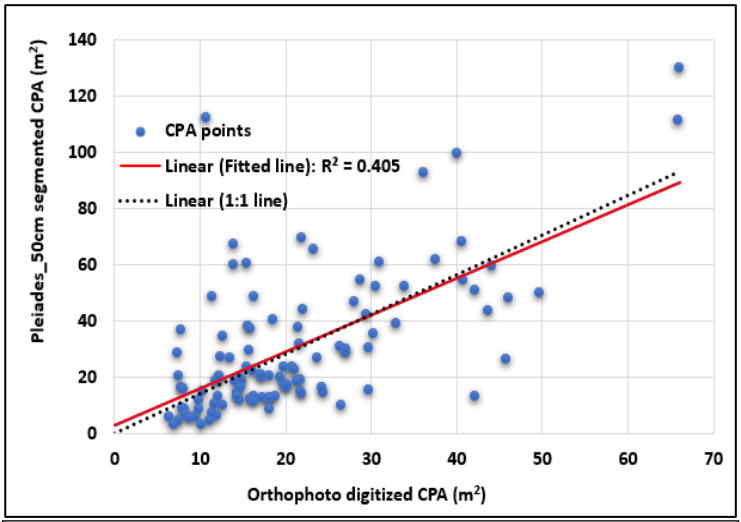

Band weight: 1,1,1,4 (R,G,B,NIR): segmentation process was influenced by near infrared band.

Figure 17: Relationship between Pleiades image automatic segmented CPA and orthophoto manually digitized CPA

The observed relationships between Orthophoto manually digitized CPA-r and UAV automatic segmented CPA-rs at 10 cm, 20 cm, 30 cm, 40 cm, and 50 cm spatial resolutions with two different band combinations (1,4,1,0_UAV_RGB and 1,1,1,4_UAV_MS), and Orthophoto digitized CPA-r and Pleiades automatic segmented CPA-rs at 50 cm with one band combination (1,1,1,4) are summarised in table 8 and 9.

Table 8: Summary of the relationship between UAV automatic segmented CPA-rs and orthophoto manually digitized CPA-r

UAV Orthophoto					
Resolution	**Relationship**	**Band weight**	**R^2**	**RMSE (m^2)**	**p-value**
10cm	Relationship between UAV 10cm segmented CPA and orthophoto digitized CPA	1,1,1,0,4 (R,G,B,NIR)	0.695	8.389	< 0.05
		1,4,1,0,0 (R,G,B,NIR)	0.747	8.951	< 0.05
20cm	Relationship between UAV 20cm segmented CPA and orthophoto digitized CPA	1,1,1,0,4 (R,G,B,NIR)	0.801	7.358	< 0.05
		1,4,1,0,0 (R,G,B,NIR)	0.547	13.675	< 0.05
30cm	Relationship between UAV 30cm segmented CPA and orthophoto digitized CPA	1,1,1,0,4 (R,G,B,NIR)	0.822	6.567	< 0.05
		1,4,1,0,0 (R,G,B,NIR)	0.568	11.257	< 0.05
40cm	Relationship between UAV 40cm segmented CPA and orthophoto digitized CPA	1,1,1,0,4 (R,G,B,NIR)	0.643	10.143	< 0.05
		1,4,1,0,0 (R,G,B,NIR)	0.46	15.928	< 0.05
50cm	Relationship between UAV 50cm segmented CPA and orthophoto digitized CPA	1,1,1,0,4 (R,G,B,NIR)	0.471	8.812	< 0.05
		1,4,1,0,0 (R,G,B,NIR)	0.398	18.3	< 0.05

UAV_MS-Band weight: 1,1,1,4 (R,G,B,NIR): segmentation process was influenced by near infrared band.
UAV_RGB-Band weight 1,4,1,0 (R,G,B,NIR): segmentation process was influenced by green band.

Table 9: Summary of the relationship between Pleiades automatic segmented CPA and Orthophoto manually digitized CPA-r

Upscaling: Pleiades					
Resolution	**Relationship**	**Band weight**	**R^2**	**RMSE (m^2)**	**p-value**
50cm	Relationship between Pleiades segmented CPA-rs and orthophoto digitized CPA	1,1,1,4 (R,G,B,NIR)	0.405	19.09	< 0.05

Pleiades-Band weight: 1,1,1,4 (R,G,B,NIR): segmentation process was influenced by near infrared band.

3.4. Relationship between field estimated DBH-f and modelled DBH-est

3.4.1. Tree detection assessment

A total of 338 trees observed from the field in 20 plots were considered for DBH modelling. The DBH for trees whose tree CPAs were detected from the automatic segmented CPA-rs were modelled using regression equation in figure 14a. A different number of trees were detected at different spatial resolutions and band combinations, as shown in figures 18 and 19.

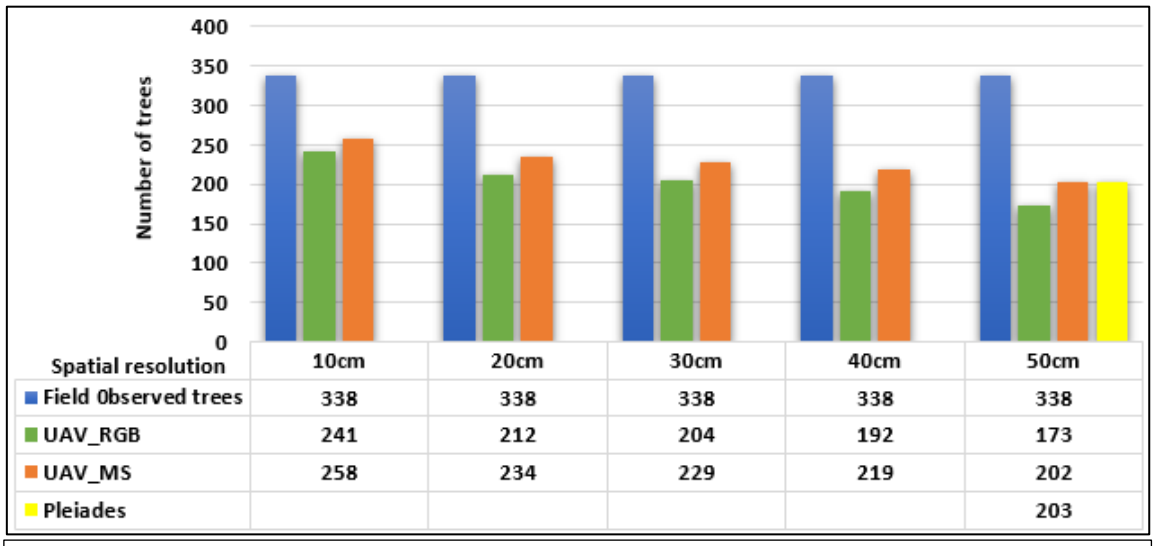

Spatial resolution	10cm	20cm	30cm	40cm	50cm
Field Observed trees	338	338	338	338	338
UAV_RGB	241	212	204	192	173
UAV_MS	258	234	229	219	202
Pleiades					203

UAV_MS-Band weight: 1,1,1,4 (R,G,B,NIR): segmentation process was influenced by near infrared band.
UAV_RGB-Band weight 1,4,1,0 (R,G,B,NIR): segmentation process was influenced by green band.
Pleiades- Band weight: 1,1,1,4 (R,G,B,NIR): segmentation process was influenced by near infrared band.

Figure 18: UAV and Pleiades tree detection at different resolutions compared to field observed trees.

In addition, it was observed that trees detection accuracy (just like segmentation accuracy) depended on UAV spatial resolution: the lower the resolution, the lower the tree detection accuracy and vice versa. The trend was similar in both UAV_MS and UAV_RGB influenced segmentation process as shown in figure 19.

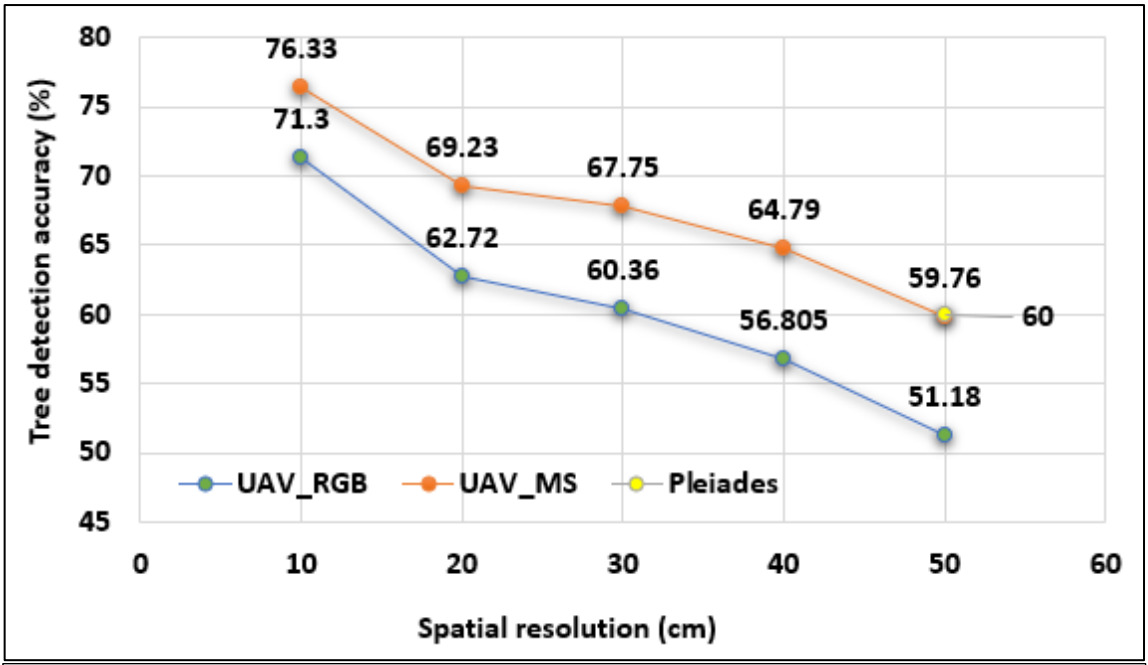

UAV_MS-Band weight: 1,1,1,4 (R,G,B,NIR): segmentation process was influenced by near infrared band.
UAV_RGB-Band weight 1,4,1,0 (R,G,B,NIR): segmentation process was influenced by green band.
Pleiades- Band weight: 1,1,1,4 (R,G,B,NIR): segmentation process was influenced by near infrared band.

Figure 19: Relationship between tree detection accuracy and UAV spatial resolution

3.4.2 Linear regression of DBH-f and modelled DBH-est.

DBH was modelled (DBH-est) for all automatically segmented crowns. From the modelled DBH-est, 140 DBH-est values from the same locations (same trees) from all different spatial resolutions and band combinations were selected and used for linear regression of field-measured DBH-f and modelled DBH-est. The selected DBH-est were then matched with their respective field measured DBH-f. For UAV, it was observed that the highest $R^2 = 0.672$ was obtained at 30 cm resolution with segmentation band weights of 1,1,1,4 (UAV_MS). In comparison, the lowest $R^2 = 0.267$ was observed at 50 cm resolution with segmentation band weights of 1,4,1,0 (UAV_RGB) as shown in figure 20 and table 10.

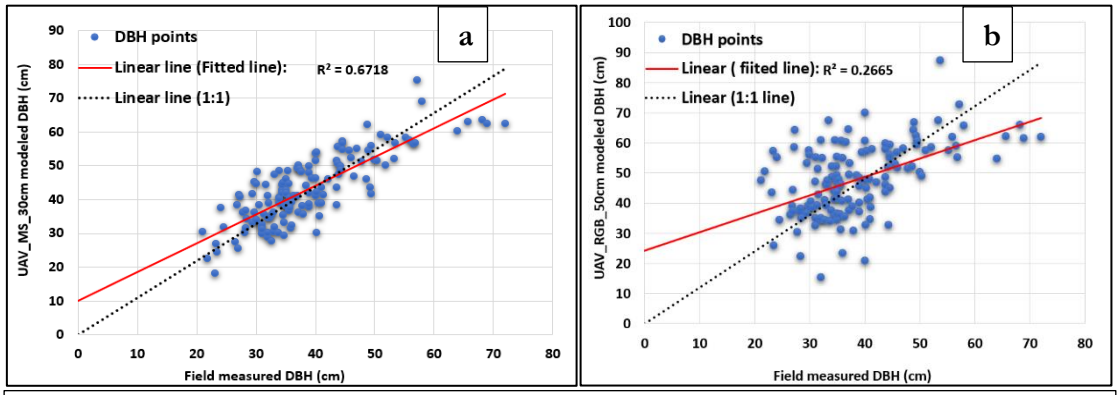

UAV_MS-Band weight: 1,1,1,4 (R,G,B,NIR): segmentation process was influenced by near infrared band.
UAV_RGB-Band weight 1,4,1,0 (R,G,B,NIR): segmentation process was influenced by green band.

Figure 20: Relationship between field measured DBH-f and UAV modelled DBH-est: a) UAV's highest R^2, b) UAV's lowest R^2

For Pleiades (50 cm resolution), the R^2 of 0.323 was observed with segmentation band weights of 1,1,1,4 as shown in figure 21 and table 11.

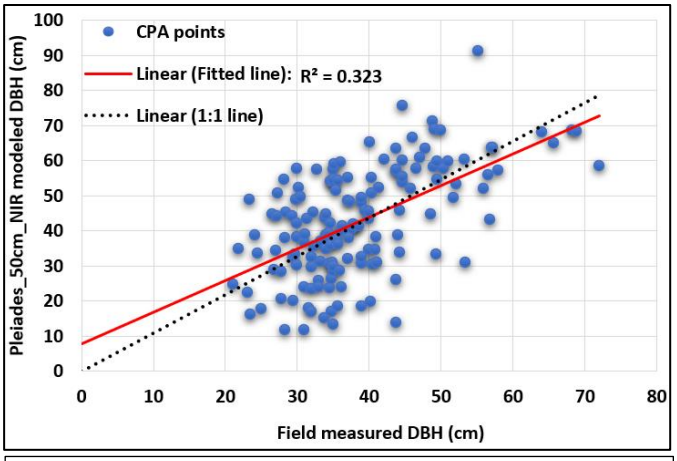

MS-Band weight: 1,1,1,4 (R,G,B,NIR): segmentation process was influenced by near infrared band.

Figure 21: Relationship between field measured DBH-f and Pleiades modelled DBH-est at 50cm.

The rest of the observed relationships between field-measured DBH-f and UAV modelled DBH-est at 10 cm, 20 cm, 30 cm, 40 cm, and 50 cm spatial resolutions with two different band combinations and field measured DBH-f and Pleiades modelled DBH-est at 50 cm with one band combination are summarised in tables 10 and 11.

Table 10: Summary of the relationship between Field measured DBH-f and UAV modelled DBH.

UAV Orthophoto					
Resolution	**Relationship**	**Band weight**	**R^2**	**RMSE (cm)**	**P-value**
10cm	Relationship between field measured DBH and UAV modelled DBH-est	1,1,1,0,4 (R,G,B,NIR)	0.548	6.947	< 0.05
		1,4,1,0,0 (R,G,B,NIR)	0.543	6.902	< 0.05
20cm	Relationship between field measured DBH and UAV modelled DBH-est	1,1,1,0,4 (R,G,B,NIR)	0.556	6.938	< 0.05
		1,4,1,0,0 (R,G,B,NIR)	0.448	9.008	< 0.05
30cm	Relationship between field measured DBH and UAV modelled DBH-est	1,1,1,0,4 (R,G,B,NIR)	0.672	5.843	< 0.05
		1,4,1,0,0 (R,G,B,NIR)	0.392	9.307	< 0.05
40cm	Relationship between field measured DBH and UAV modelled DBH-est	1,1,1,0,4 (R,G,B,NIR)	0.404	8.491	< 0.05
		1,4,1,0,0 (R,G,B,NIR)	0.455	9.359	< 0.05
50cm	Relationship between field measured DBH and UAV modelled DBH-est	1,1,1,0,4 (R,G,B,NIR)	0.408	8.545	< 0.05
		1,4,1,0,0 (R,G,B,NIR)	0.267	10.042	< 0.05

UAV_MS-Band weight: 1,1,1,4 (R,G,B,NIR): segmentation process was influenced by near infrared band.
UAV_RGB-Band weight 1,4,1,0 (R,G,B,NIR): segmentation process was influenced by green band.

Table 11: Summary of the relationship between Field measured DBH-f and Pleiades modelled DBH-est.

Upscaling: Pleiades					
Resolution	**Relationship**	**Band weight**	**R^2**	**RMSE (cm)**	**p-value**
50cm	Relationship between field measured DBH and Pleiades modelled DBH-est	1,1,1,4 (R,G,B,IR)	0.323	12.723	<0.05

Pleiades _ MS-Band weight: 1,1,1,4 (R,G,B,NIR): segmentation process was influenced by near infrared band.

3.5. Biomass calculations and comparison

3.5.1. Biomass per tree : Descriptive statistics for estimated AGB

A total of 338 trees observed from the field in 20 plots were used to calculate field estimated AGB-f. Table 12 summarises the descriptive statistics of the field estimated biomass (AGB-f) per tree of 338 coniferous trees from 20 plots. The modelled DBH-est from automatically segmented CPA at different spatial resolution and band combinations were used to calculate modelled biomass per tree (AGB-est); table 13 and 14 show the summary of the descriptive statistics of the modelled AGB-est per tree for both UAV and Pleiades.

Table 12: Descriptive statistics summary of field measured AGB-f per tree (kg)

AGB-f (kg) per tree	
Mean	666.65
Standard Error	30.819
Standard Deviation	566.601
Minimum	44.999
Maximum	4052.641
Sum	225329.129
Count	338

Table 13: Descriptive statistics summary of UAV modelled AGB-est per tree.

UAV Orthophoto							
Resolution	Band weight	Observation	Minimum (kg)	Maximum (kg)	Mean (kg)	Sum (kg)	St. Deviation (kg)
10cm	1,1,1,0,4 (R,G,B,NIR)	258	8.477	3052.665	872.878	225202.484	564.737
	1,4,1,0,0 (R,G,B,NIR)	241	4.377	3497.350	913.52	220158.374	640.126
20cm	1,1,1,0,4 (R,G,B,NIR)	234	15.63	3890.750	987.94	231178.942	655.100
	1,4,1,0,0 (R,G,B,NIR)	212	103.572	4217.826	1059.918	235702.695	706.909
30cm	1,1,1,0,4 (R,G,B,NIR)	229	4.965	3898.491	989.661	236922.520	609.480
	1,4,1,0,0 (R,G,B,NIR)	204	28.874	4626.510	1096.48	223677.505	726.533
40cm	1,1,1,0,4 (R,G,B,NIR)	219	78.828	3473.538	1077.29	239624.330	638.928
	1,4,1,0,0 (R,G,B,NIR)	192	34.071	4161.453	1162.387	223178.395	753.503
50cm	1,1,1,0,4 (R,G,B,NIR)	202	22.69	4681.792	1257.855	254086.639	765.161
	1,4,1,0,0 (R,G,B,NIR)	173	0.01	5031.565	1299.123	224748.270	823.717

UAV_MS-Band weight: 1,1,1,4 (R,G,B,NIR): segmentation process was influenced by near infrared band.
UAV_RGB-Band weight 1,4,1,0 (R,G,B,NIR): segmentation process was influenced by green band.

Table 14: Descriptive statistics summary of Pleiades modelled AGB-est per tree.

Pleiades							
Resolution	Band weight	Observation	Minimum (kg)	Maximum (kg)	Mean (kg)	Sum (kg)	St. Deviation (kg)
50cm	1,1,1,4 (R,G,B,NIR)	203	12.09	4651.85	1096.99	222689.62	828.5

Pleiades MS-Band weight: 1,1,1,4 (R,G,B,NIR): segmentation process was influenced by near infrared

Linear regression: AGB accuracy assessment per tree

From the modelled AGB-est, 140 AGB-est values per tree of the same trees from all different spatial resolutions and band combinations were selected and used for linear regression of field-measured AGB-f and modelled AGB-est. The 140 selected points of the AGB-est were then matched with their respective field measured AGB-f. For UAV, it was observed that the highest $R^2 = 0.709$ was obtained at 30 cm spatial resolution with segmentation band weights of 1,1,1,4 (UAV_MS). In contrast, the lowest $R^2 = 0.386$ was observed at 50 cm resolution with segmentation band weights of 1,4,1,0 (UAV_RGB) as shown in figure 22 and table 15.

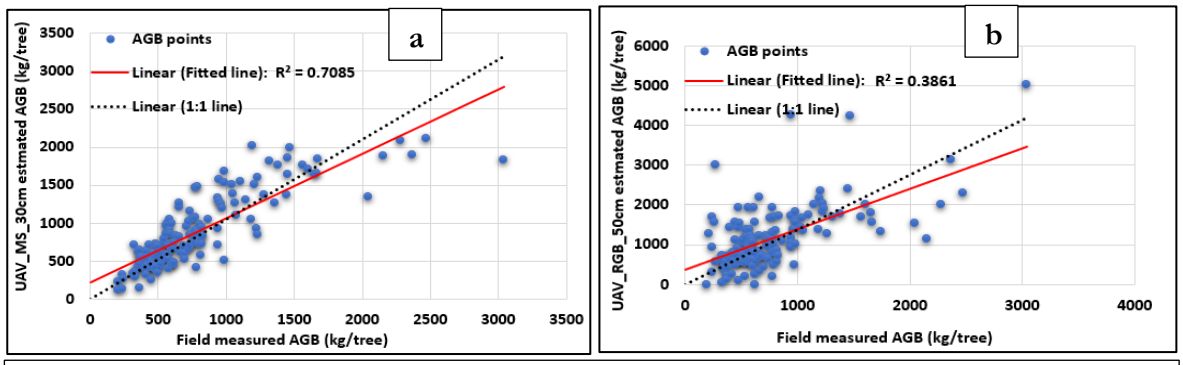

UAV_MS-Band weight: 1,1,1,4 (R,G,B,NIR): segmentation process was influenced by near infrared band.
UAV_RGB-Band weight 1,4,1,0 (R,G,B,NIR): segmentation process was influenced by green band.

Figure 22: Relationship between UAV modelled AGB-est and field estimated AGB-f: a)UAV's highest R^2, b) UAV's lowest R^2

For Pleiades (50 cm resolution), the $R^2 = 0.433$ was observed with segmentation band weights of 1,1,1,4 (Pleiades) as shown in figure 23 and table 16.

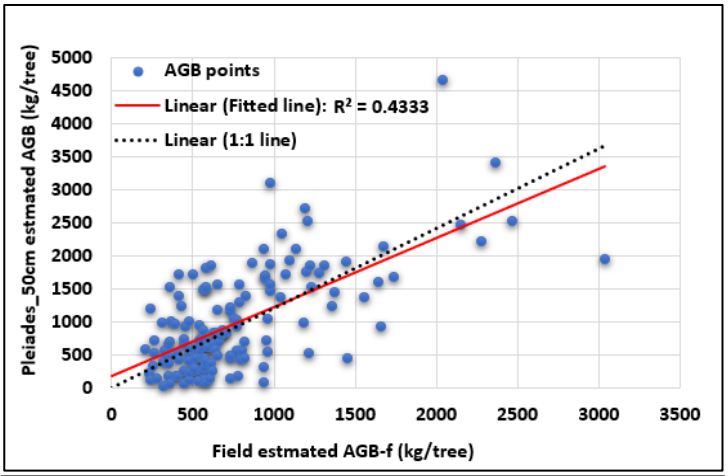

Figure 23: Relationship between field estimated AGB-f and Pleiades modelled AGB-est.

MS-Band weight: 1,1,1,4 (R,G,B,NIR): segmentation process was influenced bv near infrared band.

The other observed relationships between field estimated AGB-f and UAV modelled AGB-est at 10 cm, 20 cm, 30 cm, 40 cm, and 50 cm spatial resolutions with two different band combinations (1,4,1,0-UAV_RGB and 1,1,1,4-UAV_MS); and field measured AGB-f and Pleiades modelled AGB-est at 50 cm with one band combination (1,1,1,4) are summarised in tables 15 and 16.

Table 15: Summary of the Relationship between field estimated AGB-f and UAV modelled AGB-est per tree.

UAV Orthophoto					
Resolution	**Relationship**	**Band weight**	**R^2**	**RMSE (kg)**	**p-value**
10cm	Relationship between field estimated AGB-f and 10cm modelled AGB-est	1,1,1,0,4 (R,G,B,NIR)	0.457	357.404	< 0.05
		1,4,1,0,0 (R,G,B,NIR)	0.637	318.534	< 0.05
20cm	Relationship between field estimated AGB-f and 20cm modelled AGB-est	1,1,1,0,4 (R,G,B,NIR)	0.602	328.79	< 0.05
		1,4,1,0,0 (R,G,B,NIR)	0.615	387.914	< 0.05
30cm	Relationship between field estimated AGB-f and 30cm modelled AGB-est	1,1,1,0,4 (R,G,B,NIR)	0.708	263.088	< 0.05
		1,4,1,0,0 (R,G,B,NIR)	0.576	420.956	< 0.05
40cm	Relationship between field estimated AGB-f and 40cm modelled AGB-est	1,1,1,0,4 (R,G,B,NIR)	0.6	368.295	< 0.05
		1,4,1,0,0 (R,G,B,NIR)	0.605	423.982	< 0.05
50cm	Relationship between field estimated AGB-f and 50cm modelled AGB-est	1,1,1,0,4 (R,G,B,NIR)	0.431	445.386	< 0.05
		1,4,1,0,0 (R,G,B,NIR)	0.386	600.693	< 0.05

UAV_MS-Band weight: 1,1,1,4 (R,G,B,NIR): segmentation process was influenced by near infrared band.
UAV_RGB-Band weight 1,4,1,0 (R,G,B,NIR): segmentation process was influenced by green band.

Table 16: Summary of the Relationship between field estimated AGB-f and Pleiades modelled AGB-est per tree

Pleiades					
Resolution	**Relationship**	**Band weight**	**R^2**	**RMSE (kg)**	**p-value**
50cm	Relationship between 50cm modelled AGB per plot and field estimated AGB per plot	1,1,1,4 (R,G,B,NIR)	0.433	594.234	< 0.05

Pleiades _MS-Band weight: 1,1,1,4 (R,G,B,NIR): segmentation process was influenced by near infrared

F-test and t-test of field measured biomass and modelled biomass per tree

F-test was done with 140 samples of individual tree AGB for all resolutions and band combinations to determine if the variances of the field estimated AGB-f were equal or unequal to the modelled AGB-est. The F-test results showed that at 10 cm spatial resolution, the variances of AGB-f were equal to the AGB-est modelled from UAV_RGB influenced segmentation. At 20 cm and 30 cm spatial resolutions, the variances of AGB-f were also equal to the AGB-est modelled from UAV_MS influenced segmentation. The rest of the results are summarised in table 17.

Table 17: Summary of the F-test results for field AGB-f and modelled AGB-est per tree

F-Test Two-Sample for Variances-field estimated AGB-f per tree and modelled AGB-est per tree												
	Variable 1	Variable 2	UAV									Pleiades
Observations	140	140										
df	139	139	Spatial resolution									
			10cm		20cm		30cm		40cm		50cm	50cm
			MS	RGB	MS	RGB	MS	RGB	MS	RGB	MS	RGB	MS
F			0.911	1.087	1.259	1.546	1.02	1.908	1.569	2.11	1.501	2.837	2.601
P(F<=f) one-tail			0.292	0.313	0.088	< 0.05	0.454	< 0.05	< 0.05	< 0.05	< 0.05	< 0.05	< 0.05
F Critical one-tail			0.756	1.323	1.323	1.323	1.323	1.323	1.323	1.323	1.323	1.323	1.323
Comment			Unequal variance	Equal variance	Equal variance	Unequal variance	Equal variance	Unequal variance	Unequal variance	Unequal variance	Unequal variance	Unequal variance	Unequal variance

MS-Band weight: 1,1,1,4 (R,G,B,NIR): segmentation process was influenced by near infrared band.
RGB-Band weight 1,4,1,0 (R,G,B,NIR): segmentation process was influenced by green band.

Key:

Unequal variance – No difference between the variance of AGB-f per tree and AGB-est per tree.

Equal variance – There is a difference between the variance of AGB-f per tree and AGB-est per tree.

Subsequently, a t-test was then performed on 140 values of AGB-f per tree and AGB-est per tree assuming equal or unequal variance depending on the F-test results at different resolution and band combinations to determine if the means between the data sets were significantly different or not. The results of the t-test results are summarised in table 18.

Table 18: Summary of the t-test results for field AGB-f and modelled AGB-est per tree

The t-test results: Two-Sample Assuming Equal/Unequal Variances (based on F-test) of field estimated AGB-f and modelled AGB-est per tree												
Hypothesized Mean Difference	0	UAV										Pleiades
Observations	140	Spatial resolution										
		10cm		20cm		30cm		40cm		50cm		50cm
		MS	RGB	MS	RGB	MS	RGB	MS	RGB	MS	RGB	MS
t Stat		0.361	1.414	1.765	2.453	1.682	3.276	3.303	3.605	4.882	5.565	2.82
P(T<=t) one-tail		0.359	0.079	<0.05	< 0.05	<0.05	< 0.05	<0.05	<0.05	<0.05	< 0.05	< 0.05
t Critical one-tail		1.65	1.65	1.65	1.65	1.65	1.65	1.65	1.65	1.651	1.652	1.651
P(T<=t) two-tail		0.718	0.158	<0.05	<0.05	<0.05	<0.05	<0.05	<0.05	<0.05	<0.05	<0.05
t Critical two-tail		1.969	1.969	1.969	1.969	1.969	1.969	1.969	1.97	1.969	1.971	1.97
Comment		Not significant	Not significant	Not significant	Significant	Not significant	Significant	Significant	Significant	Significant	Significant	Significant

MS-Band weight: 1,1,1,4 (R,G,B,NIR): segmentation process was influenced by near infrared band.
RGB-Band weight 1,4,1,0 (R,G,B,NIR): segmentation process was influenced by green band.

Key:

Not significant – no difference between the means of AGB-f per tree and AGB-est per tree.

Significant There is a difference between the means of AGB-f per tree and AGB-est per tree.

3.5.2. Biomass per plot and hectare

Table 19 summarises the descriptive statistics of the field estimated AGB-f per plot of 338 coniferous trees from 20 plots. The modelled DBH-est of the automatically segmented CPA-rs at different resolution and band combinations were used to calculate modelled biomass per plot (AGB-est). Tables 20 and 21 show the summary of the descriptive statistics of the modelled AGB-est per plot for both UAV and Pleiades.

Table 19: Descriptive statistics summary of field estimated AGB per plot

AGB-f (mg) per plot	
Mean	11.266
Standard Error	1.215
Standard Deviation	5.433
Minimum	7.103
Maximum	29.678
Sum	225.329
Count	20

Table 20: Descriptive statistics summary of UAV modelled AGB-est per plot.

UAV Orthophoto estimated AGB (mg/plot)							
Resolution	Band weight	Observation	Minimun (mg)	Maximum (mg)	Mean (mg)	Sum (mg)	St.Deviation (mg)
10cm	1,1,1,0,4 (R,G,B,NIR)	20	5.812	25.592	11.26	225.202	4.207
	1,4,1,0,0 (R,G,B,NIR)	20	5.425	22.281	11.008	220.158	3.339
20cm	1,1,1,0,4 (R,G,B,NIR)	20	5.694	21.077	11.559	231.179	3.358
	1,4,1,0,0 (R,G,B,NIR)	20	5.389	24.28	11.785	235.7	4.325
30cm	1,1,1,0,4 (R,G,B,NIR)	20	6.011	21.209	11.846	236.92	3.564
	1,4,1,0,0 (R,G,B,NIR)	20	5.415	20.063	11.185	223.678	3.064
40cm	1,1,1,0,4 (R,G,B,NIR)	20	5.866	27.816	11.981	239.62	4.328
	1,4,1,0,0 (R,G,B,NIR)	20	5.453	20.623	11.159	223.178	3.257
50cm	1,1,1,0,4 (R,G,B,NIR)	20	6.049	24.581	12.704	254.087	3.968
	1,4,1,0,0 (R,G,B,NIR)	20	5.747	19.404	11.237	224.748	2.957

UAV_MS-Band weight: 1,1,1,4 (R,G,B,NIR): segmentation process was influenced by near infrared band.
UAV_RGB-Band weight 1,4,1,0 (R,G,B,NIR): segmentation process was influenced by green band.

Table 21: Descriptive statistics summary of Pleiades modelled AGB-est per plot.

Pleiades estimated AGB-est (mg/plot)							
Resolution	Band weight	Observation	Minimum (mg)	Maximum (mg)	Mean (mg)	Sum (mg)	St. Deviation (mg)
50cm	1,1,1,4 (R,G,B,NIR)	20	6.459	21.388	11.134	222.69	3.311

Pleiades _MS-Band weight: 1,1,1,4 (R,G,B,NIR): segmentation process was influenced by near infrared band.

The graphical comparison of the AGB per plot (mg) between field estimated AGB-f and modelled AGB-est per plot for all different spatial resolutions, and band combinations under study are presented in appendix 3. Figure 24 shows the graphical comparison of mean AGB per plot at different resolutions and band combinations.

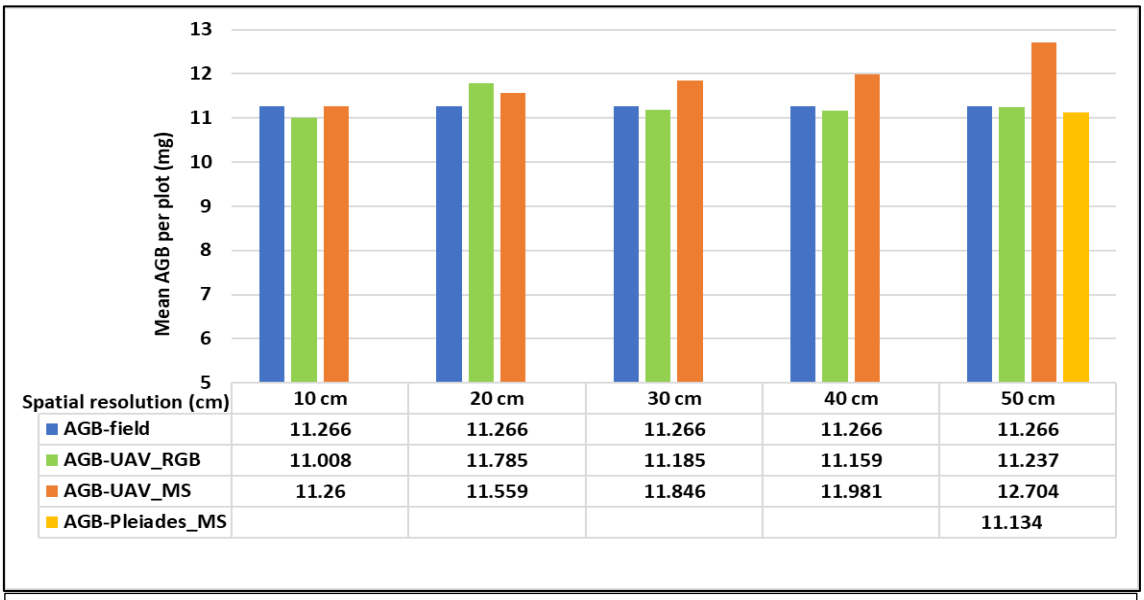

AGB-field: AGB estimated from the field.
MS-Band weight 1,1,1,4 (R,G,B,NIR): AGB estimated from segmentation process influenced by near-infrared band.
RGB-Band weight 1,4,1,0,0 (R,G,B,NIR): AGB estimated from segmentation process influenced by green band.

Figure 24: Mean AGB per plot (mg)

Linear regression: AGB accuracy assessment per plot

Figure 25 and table 22 show the results of the relationship between field estimated AGB-f per plot and modelled AGB-est per plot at different resolution and band combinations. It was observed that the highest R^2 of 0.758 was obtained at 30 cm resolution with segmentation band weights of 1,1,1,4 (UAV_MS), while the lowest R^2 = 0.197 was observed at 50 cm resolution with segmentation band weights of 1,4,1,0 (UAV_RGB).

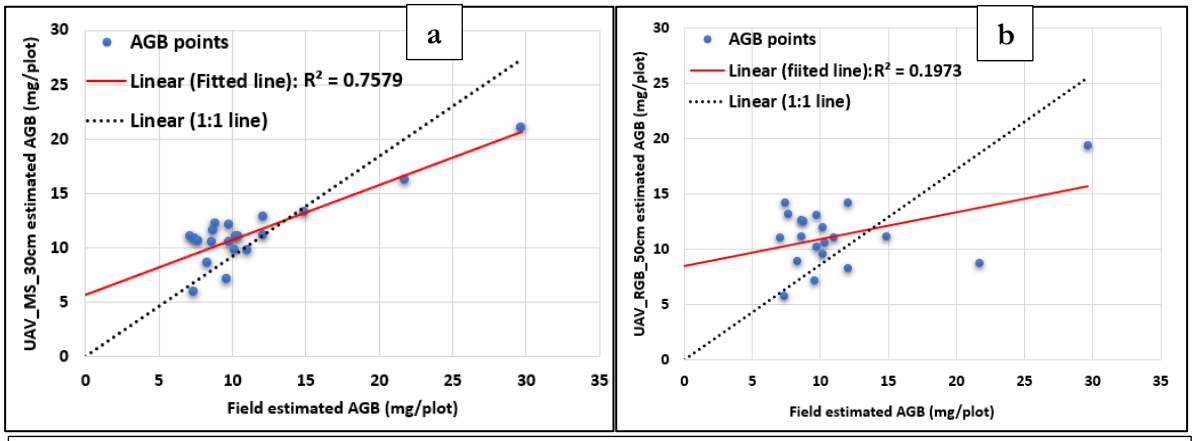

UAV_MS-Band weight: 1,1,1,4 (R,G,B,NIR): segmentation process was influenced by near infrared band.
UAV_RGB-Band weight 1,4,1,0 (R,G,B,NIR): segmentation process was influenced by green band.

Figure 25: Relationship between field estimated AGB-f and UAV modelled AGB-est per plot: a)UAV's highest R^2, b) UAV's lowest R^2

For Pleiades (50 cm resolution), the R^2 = 0.5277 was observed with segmentation band weights of 1,1,1,4 (Pleiades) as shown in figure 26 and table 23.

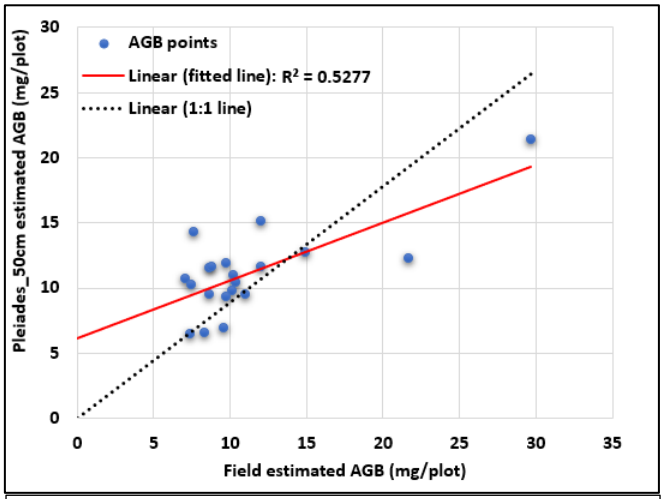

MS-Band weight: 1,1,1,4 (R,G,B,NIR): segmentation process was influenced by near infrared band.

Figure 26: Relationship between field estimated AGB-f and Pleiades modelled AGB-est per plot.

The other observed relationships between field estimated AGB-f and UAV modelled AGB-est per plot at 10 cm, 20 cm, 30 cm, 40 cm, and 50 cm spatial resolutions with two different band combinations (1,4,1,0 and 1,1,1,4); and field measured AGB-f and Pleiades modelled AGB-est per plot at 50 cm with one band combination (1,1,1,4) are summarised in table 22 and 23.

Table 22: Summary of the Relationship between field estimated AGB-f and UAV modelled AGB-est per plot.

UAV Orthophoto						
Resolution	**Relationship**	**Band weight**	**R^2**	**RMSE (mg)**	**rRMSE %**	**p-value**
10cm	Relationship between field estimated AGB-f and 10cm modelled AGB-est per plot.	1,1,1,4 (R,G,B,NIR)	0.722	2.217	19.677	< 0.05
		1,4,1,0 (R,G,B,NIR)	0.71	1.753	15.564	< 0.05
20cm	Relationship between field estimated AGB-f and 20cm modelled AGB-est per plot.	1,1,1,4 (R,G,B,NIR)	0.61	2.045	18.149	< 0.05
		1,4,1,0 (R,G,B,NIR)	0.629	1.904	16.902	< 0.05
30cm	Relationship between field estimated AGB-f and 30cm modelled AGB-est per plot.	1,1,1,4 (R,G,B,NIR)	0.758	1.507	13.381	< 0.05
		1,4,1,0 (R,G,B,NIR)	0.464	2.188	19.422	< 0.05
40cm	Relationship between field estimated AGB-f and 40cm modelled AGB-est per plot.	1,1,1,4 (R,G,B,NIR)	0.628	2.699	23.96	< 0.05
		1,4,1,0 (R,G,B,NIR)	0.549	2.132	18.928	< 0.05
50cm	Relationship between field estimated AGB-f and 50cm modelled AGB-est per plot.	1,1,1,4 (R,G,B,NIR)	0.512	2.701	23.971	< 0.05
		1,4,1,0 (R,G,B,NIR)	0.197	2.582	22.917	< 0.05

UAV_MS-Band weight: 1,1,1,4 (R,G,B,NIR): segmentation process was influenced by near infrared band.
UAV_RGB-Band weight 1,4,1,0 (R,G,B,NIR): segmentation process was influenced by green band.

Table 23: Summary of the Relationship between field estimated AGB-f and Pleiades modelled AGB-est per plot

Pleiades						
Resolution	**Relationship**	**Band weight**	**R^2**	**RMSE (mg)**	**rRMSE %**	**p-value**
50cm	Relationship between 50 cm modelled AGB and field estimated AGB-est per plot	1,1,1,4 (R,G,B,NIR)	0.528	2.218	19.69	< 0.05

Pleiades _MS-Band weight: 1,1,1,4 (R,G,B,NIR): segmentation process was influenced by near infrared band.

AGB was extrapolated from AGB per plot to AGB per hectare. Figure 27 shows the mean AGB per hectare after extrapolation. Pleiades image was acquired a year earlier than UAV images as alluded to in section 2.8; therefore, 13.2 mg/hectare (ha) of AGB was added to the mean AGB-est of Pleiades.

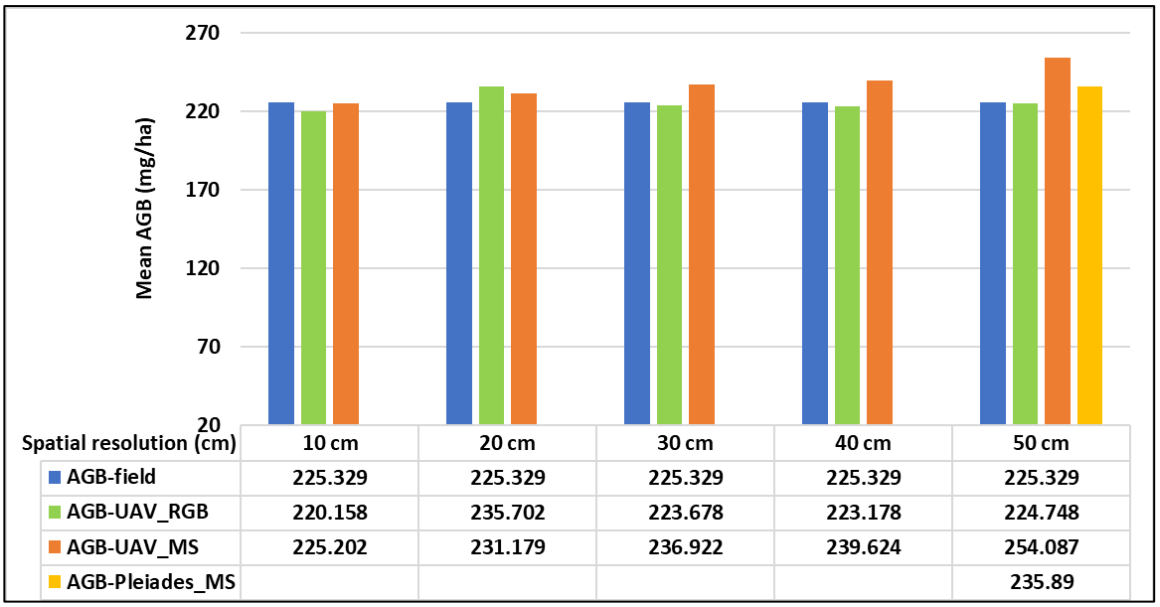

Spatial resolution (cm)	10 cm	20 cm	30 cm	40 cm	50 cm
AGB-field	225.329	225.329	225.329	225.329	225.329
AGB-UAV_RGB	220.158	235.702	223.678	223.178	224.748
AGB-UAV_MS	225.202	231.179	236.922	239.624	254.087
AGB-Pleiades_MS					235.89

AGB-field: AGB estimated from the field.
MS-Band weight 1,1,1,4 (R,G,B,NIR): AGB estimated from segmentation process influenced by near-infrared band.
RGB-Band weight 1,4,1,0,0 (R,G,B,NIR): AGB estimated from segmentation process influenced by green band.

Figure 27: Comparison of mean AGB (mg/ha)

The differences between modelled AGB-est and field estimated AGB-f (AGB-est – AGB-f) at different spatial resolution and band combinations are presented in figure 28.

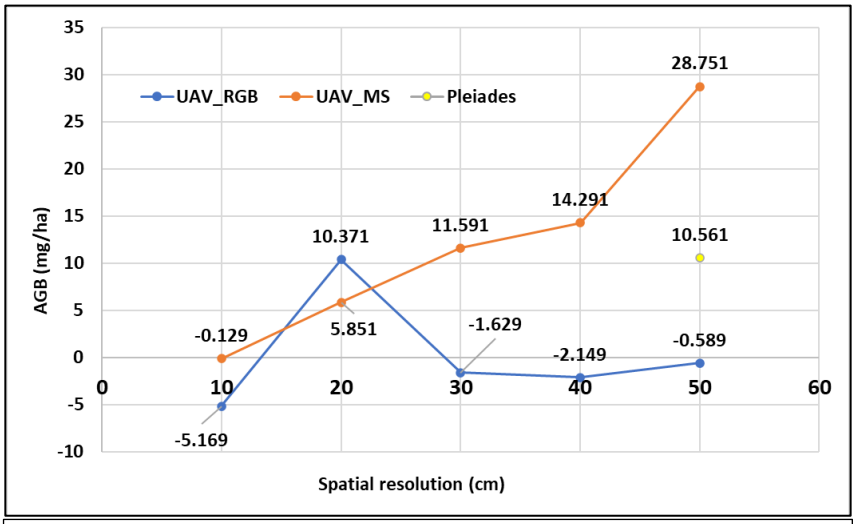

UAV_MS-Band weight 1,1,1,4 (R,G,B,NIR): AGB estimated from segmentation process influenced by near-infrared band.
UAV_RGB-Band weight 1,4,1,0,0 (R,G,B,NIR): AGB estimated from segmentation process influenced by green band.
Pleiades-Band weight 1,1,1,4 (R,G,B,NIR): AGB estimated from segmentation process influenced by near-infrared band.

Figure 28: Effects of spatial resolution on AGB estimation.

Note: Negative: Under-estimated AGB, Positive: Over-estimated AGB

F-test and t-test for field estimated biomass and modelled biomass per plot

F-test was done with 20 plots at different spatial resolutions and band combinations to determine if the variances of the field estimated AGB-f per plot were equal or unequal to the modelled AGB-est per plot. The results are shown in table 24. It should be noted that 20 plots as samples are too few to make a proper statistical conclusion; however, the results might be a true indication of the reality.

Table 24: Summary of the F-test results for AGB-f and AGB-est per plot

F-Test Two-Sample for Variances-field estimated AGB-f and modelled AGB-est per plot												
	Variable 1	Variable 2	UAV									Pleiades
Observations	20	20	Spatial resolution									
df	19	19	10cm		20cm		30cm		40cm		50cm	50cm
			MS	RGB	MS	RGB	MS	RGB	MS	RGB	MS	RGB	MS
F			0.63	0.378	0.382	0.349	0.335	0.318	0.698	0.359	0.533	0.296	0.371
P(F<=f) one-tail			0.162	<0.05	<0.05	<0.05	<0.05	<0.05	0.22	<0.05	0.09	<0.05	<0.05
F Critical one-tail			0.461	0.461	0.461	0.461	0.461	0.461	0.461	0.461	0.461	0.461	0.461
Comment			Unequal variance	Equal variance	Equal variance	Equal variance	Equal variance	Equal variance	Unequal variance	Equal variance	Unequal variance	Equal variance	Equal variance

MS-Band weight: 1,1,1,4 (R,G,B,NIR): segmentation process was influenced by near infrared band.
RGB-Band weight 1,4,1,0 (R,G,B,NIR): segmentation process was influenced by green band.

Key:

Unequal variance – no difference between the variance of AGB-f per tree and AGB-est per tree.

Equal variance – There is a difference between the variance of AGB-f per tree and AGB-est per tree.

Afterwards, t-test was performed assuming equal or unequal variance depending on the F-test results at different resolution and band combinations to determine if the means between the data sets were significantly different or not. The results of the t-test findings are summarised in table 25.

Table 25: Summary of the t-test results for AGB-f and AGB-est per plot

The t-test results: Two-Sample Assuming Equal/Unequal Variances (based on F-test) of field estimated AGB-f and modelled AGB-est per plot											
Hypothesized Mean Difference	0	UAV									Pleiades
Observations	20	Spatial resolution									
		10cm		20cm		30cm		40cm		50cm	50cm
		MS	RGB	MS	RGB	MS	RGB	MS	RGB	MS	RGB	MS
t Stat		0.004	0.181	0.205	-0.022	0.082	0.059	0.335	0.076	0.956	1.326	0.093
P(T<=t) one-tail		0.498	0.429	0.419	0.491	0.468	0.4765	0.37	0.47	0.173	0.0968	0.463
t Critical one-tail		1.688	1.686	1.686	1.686	1.686	1.686	1.687	1.696	1.69	1.69	1.69
P(T<=t) two-tail		0.997	0.857	0.839	0.982	0.935	0.953	0.74	0.94	0.346	0.194	0.927
t Critical two-tail		2.028	2.024	2.024	2.024	2.024	2.024	2.026	2.04	2.03	2.03	2.024
Comment		Not significant	Not significant	Not significant	Not significant	Not significant	Not significant	Not significant	Not significant	Not significant	Not significant	Not significant

MS-Band weight: 1,1,1,4 (R,G,B,NIR): segmentation process was influenced by near infrared band.
RGB-Band weight 1,4,1,0 (R,G,B,NIR): segmentation process was influenced by green band.

Key:

Not significant – no difference between the means of AGB-f per tree and AGB-est per tree.

Significant – There is a difference between the means of AGB-f per tree and AGB-est per tree.

4. DISCUSSION

4.1. Relationship between reference CPA-r and field measured DBH-f

An exponential relationship was observed (figures 13 and 14, section 3.2) between the field measured DBH-f and the reference CPA-r, namely, Nadir image plot photos manually digitized CPA and orthophoto manually digitized CPA. Generally, there is a logistic function kind of relationship between tree DBH and CPA. This is because, in a young forest, CPA expands as DBH grows, the rate of increase of CPA slows as the forest matures due to competition with neighbouring trees. The logistic function is exponential in its early stage, and so is the relationship between CPA and DBH before the forest is fully matured (CPA interlocks) (Shimano, 1997). This research developed a model for the relationship between field-measured DBH-f and CPA-r using DBH values in the range of 10.8 cm and 59.6 cm. The majority of the DBH values fall between 27.1 cm and 40.2 cm, as explained in figure 12, section 3.1. Therefore, the exponential function was the best fit for the model, as illustrated in Figure 29.

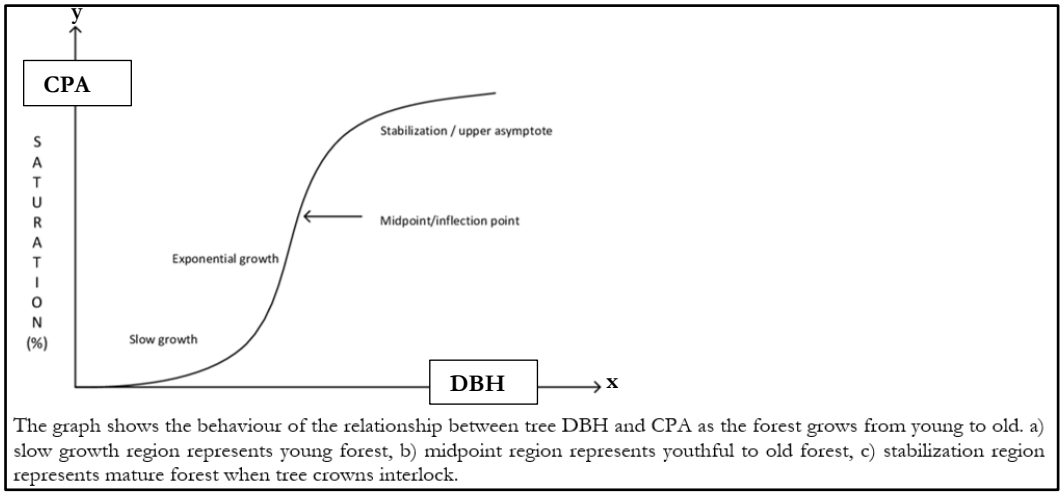

Figure 29: Illustration of a Logistic function (Lechman, 2014).

The manually digitized orthophoto CPA showed a better relationship with field measured DBH-f than manually digitized Nadir plot image CPA, therefore, the first (1. Ho) null hypothesis (section 1.6.3.) was rejected. The lower R^2 of the manually digitized Nadir image CPA could have been due to image geometry distortion caused during georeferencing of individual UAV raster plot images as it was difficult to find proper control points. The other reason could be because some plots did not have raster images with proper Nadir view, thereby having tree CPA with a distorted shape. The regression equation with R^2 of 0.731 (figure 14a) from the relationship between manually digitized orthophoto CPA with field measured DBH-f was the best model developed for this research and was used for DBH modelling. The best model of this research was however, lower than the R^2 of 0.876 which Shimano (1997) had found when he used power sigmoid (logistic function) to establish the relationship between DBH and CPA of coniferous trees.

4.2. Relationship between reference CPA-r and automatic segmented CPA-rs

4.2.1. Segmentation and Tree detection accuracy assessment

Generally, as shown in tables 6 and 7, and figure 15, it was observed that higher UAV resolution showed lower segmentation total error than lower resolution (the higher the spatial resolution, the higher the segmentation accuracy). The pattern was observed in both UAV_RGB, and UAV_MS influenced segmentation process; UAV_MS showed a better individual tree separation rate than UAV_RGB. A similar trend was also observed in tree detection accuracy assessment, as shown in figures 18 and 19. At higher resolution, more trees were detected than at lower resolution. The higher accuracy of tree detection and segmentation at higher spatial resolution than at lower resolution was as a result of higher spectral heterogeneity and a lot of details in the image, thereby making it possible to discriminate even smaller trees which were not possible to be recognized at a lower resolution (Huang, Li, & Chen, 2018; Pouliot, King, Bell, & Pitt, 2002). This implies that UAV in general is more suitable in separating individual trees at higher spatial resolution (10 cm being the best in this case) than at lower spatial resolution (50 cm being the worst in this case), and that UAV_MS is more suitable in separating individual trees than UAV_RGB.

The results of my research are similar to other publications like Huiping, Wu, & Fan (2003) who used object-based classification of different land cover classes to analyse the relationships among classification accuracy, segmentation scale, and image resolution, and observed that for tree species, the optimal resolution for image segmentation was at 10 cm. In addition, the research, which was done by Pouliot et al. (2002) where four different spatial resolutions (5 cm, 10 cm, 15 cm, and 30 cm) were used for automatic tree crown detection and delineation in high-resolution digital camera imagery of coniferous forest, a similar and stable higher tree detection accuracy was observed at 5 cm, 10 cm and 15 cm (88.9%, 88.9% and 90.9%) spatial resolutions, and a lower tree detection accuracy was observed at 30 cm (80.3%) spatial resolution. However, while my results showed a strong relationship between image segmentation accuracy and spatial resolution, Okojie (2017) who used six resampled UAV spatial resolutions (5 cm, 10 cm, 15 cm, 20 cm, 25 cm and 30 cm) to assess the forest tree structural parameter extractability did not find any relationship between spatial resolution of the image and segmentation accuracies. The contradiction in the findings could be alluded to the different forest types used in the analysis; my research used coniferous forest only whereas Okojie (2017) used both coniferous and deciduous (both separate and mixed forest).

4.2.2 Linear regression of reference CPA and automatic segmented CPA-rs

As observed from tables 8 and 9, for UAV_MS influenced segmentation process at different spatial resolutions (10 cm, 20 cm, 30 cm, 40 cm, and 50 cm), the best CPA segments compared to the reference segments were from 30cm spatial resolution which was not so different from 20 cm spatial resolution with R^2 of 0.822 and 0.801, respectively. The worst CPA segments were from 50 cm spatial resolution with $R^2 = 0.471$ compared to reference CPA.

The R^2 of the relationship between reference CPA-r and automatic CPA-rs segments of UAV_MS influenced segmentation process was lower at 10 cm than at 20 cm and 30 cm because at high spatial resolution, the spectral intra-crown variability is so high that it becomes a source of problem for the watershed transformation algorithm to detect the actual hedge of the tree crowns. The within tree crown spectral variability makes the algorithm to detect branches as tree crowns, thereby leading to over segmentation (Huang et al., 2018; Pouliot et al., 2002). This implies that better tree separation at higher resolution (10 cm) than at lower resolution (30 cm), does not certainly mean better detection of the actual hedges of tree crowns.

The original resolution of the NIR band was 11cm, as discussed in section 2.7, when the image was resampled to lower resolution (30cm), the R^2 was higher than at higher resolution (10 cm), because the resampling (bilinear interpolation) takes a 2 x 2 window with a weighted average, the averaging of pixel information reduces the image within tree crown spectral variations thereby the actual tree crown hedge is better defined during watershed transformation. However, at a very low image resolutions (40 cm, 50 cm), the tree crowns become too homogeneous such that their boundaries become less distinct, making them harder to identify by the watershed transformation algorithm (Gougeon & Leckie, 2006; Huang et al., 2018; Pouliot et al., 2002).

Generally, at all five different resolutions, the CPA-rs segments from the segmentation process which was influenced by UAV_MS performed better than CPA-rs segments from UAV_RGB because the NIR band in UAV_MS enhances segmentation accuracy: therefore, the second null hypothesis (2. Ho) was also rejected. The enhancement of segmentation accuracy occurs because the NIR band increases spectral variations between trees, which helps to clearly show tree actual hedges, thereby resulting in better tree CPA segments than UAV_RGB (Effiom, van Leeuwen, Nyktas, Okojie, & Erdbrügger, 2019; Pu & Landry, 2012).

The R^2 of the relationship between reference CPA-r and automatic CPA-rs segments of Pleiades (50 cm resolution) was very low, and so was the R^2 for both UAV_MS and UAV_RGB at 50cm resolution because at a very low resolution (50 cm), smaller size trees could not be clearly identified; therefore, difficult to separate them from the neighbouring bigger trees, which distorted the individual tree boundaries during segmentation (Huang et al., 2018; Pouliot et al., 2002).

4.3. Relationship between field measured DBH-f and estimated DBH-est.

As observed from tables 10 and 11, for UAV_MS influenced segmentation process at different spatial resolutions (10 cm, 20 cm, 30 cm, 40 cm, and 50 cm), the best-modelled DBH-est ($R^2 = 0.672$, RMSE = 5.843) compared to field measured DBH-f was at 30 cm spatial resolution. For UAV_RGB influenced segmentation process the best-modelled DBH-est ($R^2 = 0.543$, RMSE = 6.902) was at 10cm spatial resolution. This implies that UAV_SM is more accurate in DBH modelling than UAV_RGB. Moreover, these results reflected the trend observed in section 4.2.2 because the modelled DBH-est at different spatial resolution were from the CPA-rs obtained at different spatial resolution and band combination; therefore, the most accurate UAV_segmeted CPA-rs (30cm _UAV_MS: $R^2 = 0.822$), modelled the most accurate DBH-est ($R^2 = 0.672$) and vice versa. Therefore, the third null hypothesis (3. Ho) was rejected. In comparison with other similar work on DBH modelling, Guerra-Hernández et al. (2017) used a multi-temporal UAV imagery to model DBH of Italian stone pine (*Pinus pinea*) from UAV derived tree height and CPA, and found a better R^2 of 0.79 with RMSE of 2.36 cm compared to my research. The better R^2 of Guerra-Hernández et al. (2017) could be because they used only one tree species (*Pinus pinea*) to model the DBH, thereby avoiding errors from variations of DBH of different tree species.

4.4. Biomass calculations and comparison per tree and plot.

Descriptive statistics of field AGB per tree

The descriptive statistics of field AGB per tree as presented in table 12 showed that the field measured AGB-f had a minimum AGB-f of 44.999 kg, maximum AGB-f of 4052.641 kg and mean AGB-f of 666.650 kg (DBH ranging from 10.8 cm to 85.6 cm with a sample size of 338 coniferous trees). The results of descriptive statistics per tree are similar to Popescu (2007) who estimated AGB of individual pine trees using airborne Lidar; a minimum AGB of 13.02 kg, maximum AGB of 3254.11 kg and mean of 486.55 kg (DBH ranged from 8.13 cm to 78.49 cm with a sample size of 43 coniferous trees) were observed. The differences in the descriptive statistic of AGB values between my research and

that of Popescu (2007) could be attributed to differences in the DBH range and sample size. The modelled AGB-est showed differences in the minimum, maximum, and mean AGB-est per tree as shown in tables 13 and 14; the differences were attributed to differences in different spatial resolution and band combinations used to model the AGB-est.

Linear regression of AGB per tree

The linear regression of UAV modelled AGB-est per tree (140 trees) showed that the UAV_MS at 30 cm resolution had the highest accuracy (R^2 = 0.708, RMSE = 263.088 kg) followed by UAV_RGB influenced segmentation process at 10 cm (R^2 = 0.637, RMSE = 318 kg) and the least accurate was UAV_RGB at 50 cm resolution as elaborated in table 15. This means that UAV_MS at 30 cm resolution was the most accurate in modelling the DBH than any other resolutions. The results of this research were lower than that of Lin, Wang, Ma, & Lin (2018) who found the R^2 of 0.96 with RMSE of 54.90 kg from the accuracy assessment of the estimated individual tree AGB using UAV orthophoto of oblique photographs at 5 cm spatial resolution. Again, it was observed that the individual tree AGB accuracy assessment results reflected what was discussed in section 4.2.2, where UAV_MS at 30 cm resolution had the most accurate CPA-rs (R^2 = 0.822), which modelled the most accurate DBH (R^2 = 0.672), and subsequently modelled the most accurate AGB-est per tree (R^2 = 0.708). In contrast, UAV_RGB at 50 cm resolution had the least accurate CPA-rs (R^2 = 0.398), which modelled the least accurate DBH-est (R^2 = 0.267) and subsequently modelled the least accurate AGB-est per tree (R^2 = 0.386). This implies that accurate modelling of individual tree CPA leads to accurate estimation of AGB per tree.

Accuracy assessment of UAV modelled AGB-est per plot (20 plots) showed that UAV_MS at 30 cm resolution had the highest accuracy (R^2 = 0.758, RMSE = 1.507 mg _ AGB/plot, rRMSE = 13.381%), and the least accurate was UAV_RGB at 50 cm resolution as shown in table 22 and 23. The accuracy of the AGB-est per plot modelled by this research at all different spatial resolutions (10 cm, 20 cm, 30 cm, 40 cm and 50 cm) had relative RMSE (rRMSE) of less than 24% which were comparable to Jayathunga, Owari, & Tsuyuki (2018) who used UAV orthophoto at 5 cm spatial resolution to estimate AGB over mixed conifer-broadleaf forest, and found RMSE of 14.3 mg C/ha (1.43 mg _ AGB/plot) and rRMSE = 17.4%.

Comparison of mean AGB per hectare: Effects of spatial resolution on AGB estimation.

It was observed in figure 28 that for UAV_MS, the AGB estimation per hectare steadily increased with reducing spatial resolution. This was because the NIR band in UAV_MS, as earlier alluded to in section 4.2.2, enhances segmentation accuracy as it (NIR) increases spectral variations between trees. However, at a lower resolution, smaller trees can not be separated from the bigger trees; therefore, they are identified as one tree crown (generalization), which leads to an overestimation of biomass. This could mean that the methods presented in this research might not be ideal for estimating biomass with UAV_MS at a lower resolution (50cm). For UAV_RGB, the AGB estimation per hectare increased with reducing resolution from 10 cm to 20 cm, and then it dropped drastically from 20 cm to 30 cm; from 30 cm to 50 cm, the AGB estimation per hectare was stable and uniform. This could mean that UAV_RGB has a spatial resolution threshold beyond which it can not exceed in estimating AGB per hectare. Generally, the observed trend in figure 28 needs further investigation.

F-Test and t-test of field estimated AGB-f and modelled AGB-est

The F-test results on AGB per tree reviewed that the AGB-est per tree modelled from UAV_RGB at 10 cm resolution, and UAV_MS at 20 cm and 30 cm resolution were more accurate than the rest of the AGB-est per tree estimated from other resolutions as their AGB-est per tree variances were equal to the variance of field estimated AGB-f per tree (table 17). Furthermore, the t-test results on the 140 AGB per tree values from the same trees observed from the field and images at different spatial resolution and band combinations as shown in table 18, showed that the means of the

UAV_RGB and UAV_MS estimated AGB-est per tree at 10 cm spatial resolution were not significantly different from means of the field estimated AGB-f per tree. At 20 cm and 30 cm spatial resolution, the means of the field estimated AGB-f per tree were also not significantly different from the means of AGB-est per tree estimated with UAV_MS but significantly different from the means of AGB-est per tree estimated with UAV_RGB. The means of field estimated AGB-f per tree were significantly different from the means of AGB-est per tree from both UAV_MS and UAV_RGB at 40 cm and 50 cm resolutions as well as Pleiades at 50 cm spatial resolution. This implied that AGB per tree could be estimated at 10 cm spatial resolution with UAV_MS and UAV_RGB as well as at 20 cm and 30 cm spatial resolution with UAV_MS.
A similar observation was also made by Lin et al. (2018) who used a 5 cm spatial resolution UAV orthophoto to model the AGB of individual trees of coniferous forest and concluded that UAV is effective in estimating individual tree AGB at very high spatial resolution.

The t-test results on the AGB per plot from the 20 plots showed no significant differences between the means of the AGB-f estimated from the field and AGB-est means estimated from UAV_RGB and UAV_MS, and Pleiades at different spatial resolution and band combinations as shown in table 25. Therefore, the fourth Null hypothesis (4. Ho) was accepted; this could mean that the losses of estimated biomass per tree at different resolutions (10 cm, 20 cm, 30 cm 40 cm and 50 cm) and band combinations because of occlusion by bigger trees and image under-segmentation were compensated in the overall estimated AGB-est per plot. The results of the t-test of AGB per plot also implied that AGB per plot could be estimated using UAV_RGB and UAV_MS at 10 cm, 20 cm, 30 cm, 40 cm, and 50 cm spatial resolution as well as Pleiades at 50 cm spatial resolution with reasonable accuracy.

The results of the t-test per plot for this research were comparable to other studies like: (1) Jayathunga, Owari, & Tsuyuki (2018) who used UAV orthophoto at 5 cm spatial resolution to estimate AGB over the mixed conifer-broadleaf forest and concluded that UAV could accurately assess forest biomass as the means of the reference AGB were not significantly different from UAV estimated AGB. (2) Wahyuni, Jaya, & Puspaningsih (2016) who used a UAV orthophoto with 10 cm spatial resolution to develop a mathematical model for AGB estimation; the modelled AGB did not differ significantly from the reference AGB. The paper also concluded that UAV imagery could be used to estimate AGB accurately.

4.5. Uncertainties

Firstly, the two models used in this research to estimate the DBH-est (regression equation in figure 14a) and AGB allometric equation (equation 5) might have been the source of errors as models are a simplification of reality, and built from a sample population (selected trees) and not from the entire population (forest); therefore, when sample population is changed, the adjustment of the model also slightly changes (Chave et al., 2004; Chen, Laurin, & Valentini, 2015). For allometric equation uncertainties, Vorster et al. (2020) analysed the variability and uncertainty involved in forest AGB estimates from individual trees to large scale and found out that depending on the allometric equation and evaluation method used in AGB estimation, the allometric uncertainty contributes 30% – 75% of the total uncertainty, while remote sensing fitting model uncertainty contributes 25% – 70% of the total uncertainty. Clough et al. (2016) also used a data-driven, hierarchical modelling approach to quantify allometric model uncertainty for plot-level tree biomass and concluded that allometric models have a huge contribution to the overall uncertainty of AGB estimates. My research applied generalized European spruce allometric equation to all the coniferous species under study (table 3), which might also be a source of errors as allometric equations are species and site-specific (Abich,

Mucheye, Tebikew, Gebremariam, & Alemu, 2019; Basuki, van Laake, Skidmore, & Hussin, 2009 and Mahmood et al., 2020).

Secondly, as mentioned (section 2.9), the image segmentation rule set is resolution and band combination dependent. The different rule sets (appendix 1) used in this research for image segmentation at different resolution and band combinations were developed based on trial and error and were assured to be optimal rule sets.

4.6 Limitations

Firstly, the DBH value range was too narrow, with the majority falling between 23 cm to 42 cm (figure 12) because the data was collected from the semi-natural forest for timber production. This meant that the model developed in figure 14a was less accurate in predicting DBH values falling below 23 cm and above 42 cm. This was also elaborated more in Section 4.1; figure 29 where it was explained that the complete relationship between forest trees DBH and CPA should have a logistic function; however, this research just extracted a part of this function (exponential) to develop a DBH-CPA relationship. This meant that the developed model (figure 14a) could only be used to predict DBH in a youthful to old coniferous forest, but not in young and mature coniferous forest.

Secondly, small data set of field plots (20 plots) was used in the analysis. The number of plots used were too few to make a proper statistical conclusion. To make an appropriate statical conclusion minimum sample plots should have been at least 30 (Louangrath, 2017).

Lastly, unable to find a site-specific allometric equation as discussed in section 4.5 site specific allometric equations are more accurate than generalised equation.

5.0. CONCLUSION AND RECOMMENDATIONS

5.1. Conclusion

In this research, UAV at different resampled spatial resolutions and band combinations, and Pleiades were used to study the effect of spatial resolution and band combination on coniferous forest AGB estimation. It was established that the AGB per tree could be accurately estimated at 10 cm spatial resolution with UAV_MS and UAV_RGB, as well as at 20 cm and 30 cm spatial resolution with UAV_MS. The AGB per plot could be estimated with reasonable accuracy using UAV_RGB and UAV_MS at 10 cm, 20 cm, 30 cm, 40 cm, and 50 cm spatial resolutions as well as Pleiades at 50 cm spatial resolution. The specific conclusions of this study based on the four research questions are highlighted below.

Research question 1:

a. What is the relationship between field measured DBH-f and reference CPA-r?

The manually digitized orthophoto CPA showed a better relationship (R^2 of 0.731; RMSE of 6.906 m^2) with field measured DBH than manually digitized Nadir image CPA (R^2 of 0.584; RMSE of 9.797 m^2) .

Research question 2:

a. What is the accuracy of the automatic segmented CPA-rs from UAV and Pleiades at different spatial resolutions and band combinations compared with the reference CPA-r?

The UAV_MS at 30cm resolution produced the most accurate automatic CPA segments (R^2 of 0.822 and RMSE of 6.567 m^2) than any other resolutions and band combination.

Research question 3:

a. What is the accuracy of the estimated DBH-est compared to field measured DBH-f?

The UAV_MS at 30cm modelled the most accurate DBH-est (R^2 = 0.672 and RMSE of 5.843 cm) than any other resolutions and band combination.

Research question 4:

a. Does the estimated AGB-est differ significantly from field measured AGB-f?

There were no significant differences between the means of the AGB-f per plot estimated from the field and the means of the AGB-est per plot estimated from UAV_RGB and UAV_MS at 10 cm, 20 cm, 30 cm, 40 cm, and 50 cm spatial resolutions as well as Pleiades at 50 cm spatial resolutions.

5.2. Recommendations

Firstly, further studies are needed where the methods presented in this study can be used in a natural forest with large data set of field plots (more than 30). The natural forest has a wide range of DBH distribution, unlike the semi-natural (Haagse Bos) forest where majoring of the trees had the DBH ranging from 23 cm to 42 cm. The wide range of DBH might be vital for developing a stable model (DBH-CPA relationship).

Secondly, further studies are needed where higher spatial resolution satellite (30 cm like worldview-3 or 4) than the Pleiades 1A/B where tree crowns can be clearly seen. If tree crowns can be clearly seen from the satellite image, manually digitising of tree crowns can be done and develop a satellite-based DBH-CPA relationship model directly.

List of references

Abich, A., Mucheye, T., Tebikew, M., Gebremariam, Y., & Alemu, A. (2019). Species-specific allometric equations for improving aboveground biomass estimates of dry deciduous woodland ecosystems. *Journal of Forestry Research*, *30*(5), 1619–1632. https://doi.org/10.1007/s11676-018-0707-5

Alonzo, M., Bookhagen, B., & Roberts, D. A. (2014). Urban tree species mapping using hyperspectral and lidar data fusion. *Remote Sensing of Environment*, *148*, 70–83. https://doi.org/10.1016/j.rse.2014.03.018

Asner, G. P. (2001). Cloud cover in Landsat observations of the Brazilian Amazon. *International Journal of Remote Sensing*, *22*(18), 3855–3862. https://doi.org/10.1080/01431160010006926

Baboo, D. S. S., & Devi, M. R. (2010). An Analysis of Different Resampling Methods in Coimbatore, District. *Global Journal of Computer Science and Technology*, *10*(15), 61–66. Retrieved from http://globaljournals.org/GJCST_Volume10/10-An-Analysis-of-Different-Resampling-Methods-in-Coimbatore-District.pdf

Baral. (2016). *Mapping Carbon Stock Using High Resolution Satellite Imagery in Sub Tropical Forest of USING HIGH RESOLUTION SATELLITE IMAGES IN SUB-TROPICAL FOREST OF NEPAL*. (September). https://doi.org/10.13140/RG.2.1.3996.9768

Basuki, T. M., van Laake, P. E., Skidmore, A. K., & Hussin, Y. A. (2009). Allometric equations for estimating the above-ground biomass in tropical lowland Dipterocarp forests. *Forest Ecology and Management*, *257*(8), 1684–1694. https://doi.org/10.1016/j.foreco.2009.01.027

Bins, L. S., Fonseca, L. M. G., Erthal, G. J., & Ii, F. M. (1996). Satellite Imagery Segmentation : a region growing approach. *Anais VIII Simposia Brasilerio de Sensoriamenta Remoto, Salvador, Brasil, 14-19 Abril 1996, INPE*, 677–680. Retrieved from https://d1wqtxts1xzle7.cloudfront.net/6503536/10.1.1.93.4555.pdf?response-content-disposition=inline%3B+filename%3DSatellite_imagery_segmentation_a_region.pdf&Expires=1603366749&Signature=dnuGfHGDjJTUDYm7B-KtGpNOsI1foHiUVsOY9tVnRvh1No0rIkcxCGBjoisO8JSuRJR

Borra-Serrano, I., Peña, J. M., Torres-Sánchez, J., Mesas-Carrascosa, F. J., & López-Granados, F. (2015). Spatial quality evaluation of resampled unmanned aerial vehicle-imagery for weed mapping. *Sensors (Switzerland)*, *15*(8), 19688–19708. https://doi.org/10.3390/s150819688

Boyd, D. S., & Danson, F. M. (2005, March). Satellite remote sensing of forest resources: Three decades of research development. *Progress in Physical Geography*, Vol. 29, pp. 1–26. https://doi.org/10.1191/0309133305pp432ra

Brack, D. (2019). Background Analytical Study Forests and Climate Change. *Fourteenth Session of the United Nations Forum on Forests*, 56. Retrieved from https://www.un.org/esa/forests/wp-content/uploads/2019/03/UNFF14-BkgdStudy-SDG13-March2019.pdf

Brokaw, N., & Thompson, J. (2000). The H for DBH. *Forest Ecology and Management*, *129*(1–3), 89–91. https://doi.org/10.1016/S0378-1127(99)00141-3

Calders, K., Jonckheere, I., Nightingale, J., & Vastaranta, M. (2020). Remote sensing technology applications in forestry and REDD+. *Forests*, *11*(2), 10–13. https://doi.org/10.3390/f11020188

Carrasco-Escobar, G., Manrique, E., Ruiz-Cabrejos, J., Saavedra, M., Alava, F., Bickersmith, S., … Gamboa, D. (2019). High-accuracy detection of malaria vector larval habitats using drone-based multispectral imagery. *PLoS Neglected Tropical Diseases*, *13*(1). https://doi.org/10.1371/journal.pntd.0007105

Chave^, J., Condit^, R., Aguilar^, S., Hernandez^, A., Lao^, S., & Perez^, R. (2004). *THE ROYAL SOCIETY Error propagation and scaling for tropical forest biomass estimates*. https://doi.org/10.1098/rstb.2003.1425

Chave, J., Réjou-Méchain, M., Búrquez, A., Chidumayo, E., Colgan, M. S., Delitti, W. B. C., … Vieilledent, G. (2014). Improved allometric models to estimate the aboveground biomass of tropical trees. *Global Change Biology*, *20*(10), 3177–3190. https://doi.org/10.1111/gcb.12629

Chen, Q., Laurin, G. V., & Valentini, R. (2015). Uncertainty of remotely sensed aboveground biomass over an African tropical forest: Propagating errors from trees to plots to pixels. *Remote Sensing of Environment*, *160*, 134–143. https://doi.org/10.1016/j.rse.2015.01.009

Ciais, P., Sabine, C., Bala, G., Bopp, L., Brovkin, V., Canadell, J., … Brovkin Germany, V. (2013). *Carbon and Other Biogeochemical Cycles. In: Cli-mate Change 2013: The Physical Science Basis. Contribution of Working Group I to the Fifth Assessment Report of the Intergovernmental Panel on Climate*

Change Coordinating Lead Authors: Lead Authors: Contribu. Retrieved from Peter website: https://www.ipcc.ch/site/assets/uploads/2018/02/WG1AR5_Chapter06_FINAL.pdf

Clinton, N., Holt, A., Scarborough, J., Yan, L. I., & Gong, P. (2010). Accuracy assessment measures for object-based image segmentation goodness. *Photogrammetric Engineering and Remote Sensing*, *76*(3), 289–299. https://doi.org/10.14358/PERS.76.3.289

Clough, B. J., Russell, M. B., Domke, G. M., & Woodall, C. W. (2016). Quantifying allometric model uncertainty for plot-level live tree biomass stocks with a data-driven, hierarchical framework. *Forest Ecology and Management*, *372*, 175–188. https://doi.org/10.1016/j.foreco.2016.04.001

Cummings, D. L., Boone Kauffman, J., Perry, D. A., & Flint Hughes, R. (2002). Aboveground biomass and structure of rainforests in the southwestern Brazilian Amazon. *Forest Ecology and Management*, *163*(1–3), 293–307. https://doi.org/10.1016/S0378-1127(01)00587-4

Dandois, J. P., Olano, M., & Ellis, E. C. (2015). Optimal altitude, overlap, and weather conditions for computer vision uav estimates of forest structure. *Remote Sensing*, *7*(10), 13895–13920. https://doi.org/10.3390/rs71013895

Definiens Developer XD 2.0.4 User Guide. (2012). Retrieved from https://www.imperial.ac.uk/media/imperial-college/medicine/facilities/film/Definiens-Developer-Reference-Book-XD-2.0.4.pdf

Duncanson, L., Armston, J., Disney, M., Avitabile, V., Barbier, N., Calders, K., … Williams, M. (2019). The Importance of Consistent Global Forest Aboveground Biomass Product Validation. *Surveys in Geophysics*, *40*(4), 979–999. https://doi.org/10.1007/s10712-019-09538-8

Effiom, A. E., van Leeuwen, L. M., Nyktas, P., Okojie, J. A., & Erdbrügger, J. (2019). Combining unmanned aerial vehicle and multispectral Pleiades data for tree species identification, a prerequisite for accurate carbon estimation. *Journal of Applied Remote Sensing*, *13*(03), 1. https://doi.org/10.1117/1.jrs.13.034530

Elhabiby, M., Elsharkawy, A., & El-Sheimy, N. (2012). Curvelet transform for water bodies extraction from high resolution satellite images. *The International Conference on Electrical Engineering*, *8*(8th), 1–19. https://doi.org/10.21608/iceeng.2012.30818

Etikan, I. (2016). Comparison of Convenience Sampling and Purposive Sampling. *American Journal of Theoretical and Applied Statistics*, *5*(1), 1. https://doi.org/10.11648/j.ajtas.20160501.11

European Commission. (2019). The European Green Deal. *European Commission*, *53*(9), 24. https://doi.org/10.1017/CBO9781107415324.004

Fernández-Manso, O., Fernández-Manso, A., & Quintano, C. (2014). Estimation of aboveground biomass in Mediterranean forestsby statistical modelling of ASTER fraction images. *International Journal of Applied Earth Observation and Geoinformation*, *31*(1), 45–56. https://doi.org/10.1016/j.jag.2014.03.005

Food and Agriculture Organization. (2015). Global Forest Resources Assessment 2015 - How are the world's forests changing? In *FAO Forestry*. Retrieved from www.fao.org/forestry/fra

Gibbs, H. K., Brown, S., Niles, J. O., & Foley, J. A. (2007). Monitoring and estimating tropical forest carbon stocks: Making REDD a reality. In *Environmental Research Letters* (Vol. 2). https://doi.org/10.1088/1748-9326/2/4/045023

Gopinathan, K. K. (1988). A general formula for computing the coefficients of the correlation connecting global solar radiation to sunshine duration. *Solar Energy*, *41*(6), 499–502. https://doi.org/10.1016/0038-092X(88)90052-7

Gougeon, F. A., & Leckie, D. G. (2006). *The Individual Tree Crown Approach Applied to Ikonos Images of a Coniferous Plantation Area*.

Guerra-Hernández, J., González-Ferreiro, E., Monleón, V. J., Faias, S. P., Tomé, M., & Díaz-Varela, R. A. (2017). Use of multi-temporal UAV-derived imagery for estimating individual tree growth in Pinus pinea stands. *Forests*, *8*(8), 300. https://doi.org/10.3390/f8080300

Gytarsky, M., Kurz, W. A., Ogle, S., Richards, G., & Somogyi, Z. (2006). *Volume 4: Agriculture, Forestry and Other Land Use 1.2 2006 IPCC Guidelines for National Greenhouse Gas Inventories*. Retrieved from https://www.ipcc-nggip.iges.or.jp/public/2006gl/pdf/4_Volume4/V4_01_Ch1_Introduction.pdf

Haagse Bos (Overijssel) - Wikipedia. (2018). Retrieved August 25, 2020, from https://nl.wikipedia.org/wiki/Haagse_Bos_(Overijssel)

Halabisky, M., Babcock, C., & Moskal, L. M. (2018). Harnessing the temporal dimension to improve object-based image analysis classification of wetlands. *Remote Sensing*, *10*(9). https://doi.org/10.3390/rs10091467

Hay, G. J., Castilla, G., Wulder, M. A., & Ruiz, J. R. (2005). An automated object-based approach for the multiscale image segmentation of forest scenes. *International Journal of Applied Earth Observation and Geoinformation*, *7*(4), 339–359. https://doi.org/10.1016/j.jag.2005.06.005

Hennessy, A., Clarke, K., & Lewis, M. (2020). Hyperspectral Classification of Plants: A Review of Waveband Selection Generalisability. *Remote Sensing*, *12*(1), 113. https://doi.org/10.3390/rs12010113

Herold, M., Carter, S., Avitabile, V., Espejo, A. B., Jonckheere, I., Lucas, R., … De Sy, V. (2019, July 15). The Role and Need for Space-Based Forest Biomass-Related Measurements in Environmental Management and Policy. *Surveys in Geophysics*, Vol. 40, pp. 757–778. https://doi.org/10.1007/s10712-019-09510-6

Hirata, Y., Takao, G., Sato, T., & Toriyama, J. (2012). *REDD-plus Cookbook Reducing Emissions from Deforestation and forest Degradation and the Role of Conservation, Sustainable Management of Forests and Enhancement*. 156. Retrieved from https://www.ffpri.affrc.go.jp/redd-rdc/en/reference/cookbook/redd_cookbook_all_high_en.pdf

Hirschmugl, M., Ofner, M., Raggam, J., & Schardt, M. (2007). Single tree detection in very high resolution remote sensing data. *Remote Sensing of Environment*, *110*(4), 533–544. https://doi.org/10.1016/j.rse.2007.02.029

Holman, F. H., Riche, A. B., Castle, M., Wooster, M. J., & Hawkesford, M. J. (2019). Radiometric calibration of "commercial offthe shelf" cameras for UAV-based high-resolution temporal crop phenotyping of reflectance and NDVI. *Remote Sensing*, *11*(14). https://doi.org/10.3390/rs11141657

Hossain, M. D., & Chen, D. (2019). Segmentation for Object-Based Image Analysis (OBIA): A review of algorithms and challenges from remote sensing perspective. *ISPRS Journal of Photogrammetry and Remote Sensing*, *150*(February), 115–134. https://doi.org/10.1016/j.isprsjprs.2019.02.009

Huang, Hongyu, Li, X., & Chen, C. (2018). Individual tree crown detection and delineation from very-high-resolution UAV images based on bias field and marker-controlled watershed segmentation algorithms. *IEEE Journal of Selected Topics in Applied Earth Observations and Remote Sensing*, *11*(7), 2253–2262. https://doi.org/10.1109/JSTARS.2018.2830410

Huang, Huiping, Wu, B., & Fan, J. (2003). Analysis to the Relationship of Classification Accuracy, Segmentation Scale, Image Resolution. *International Geoscience and Remote Sensing Symposium (IGARSS)*, *6*, 3671–3673. https://doi.org/10.1109/igarss.2003.1295233

Hughes, R. F., Kauffman, J. B., & Jaramillo, V. J. (2000). Ecosystem-scale impacts of deforestation and land use in a humid tropical region of Mexico. *Ecological Applications*, *10*(2), 515–527. https://doi.org/10.1890/1051-0761(2000)010[0515:ESIODA]2.0.CO;2

Issa, S., Dahy, B., Ksiksi, T., & Saleous, N. (2020). A review of terrestrial carbon assessment methods using geo-spatial technologies with emphasis on arid lands. *Remote Sensing*, *12*(12). https://doi.org/10.3390/rs12122008

Jayathunga, S., Owari, T., & Tsuyuki, S. (2018). The use of fixed–wing UAV photogrammetry with LiDAR DTM to estimate merchantable volume and carbon stock in living biomass over a mixed conifer–broadleaf forest. *International Journal of Applied Earth Observation and Geoinformation*, *73*, 767–777. https://doi.org/10.1016/j.jag.2018.08.017

Joshi, N., Mitchard, E. T. A., Brolly, M., Schumacher, J., Fernández-Landa, A., Johannsen, V. K., … Fensholt, R. (2017). Understanding "saturation" of radar signals over forests. *Scientific Reports*, *7*(1), 1–11. https://doi.org/10.1038/s41598-017-03469-3

Kankare, V., Holopainen, M., Vastaranta, M., Puttonen, E., Yu, X., Hyyppä, J., … Alho, P. (2013). Individual tree biomass estimation using terrestrial laser scanning. *ISPRS Journal of Photogrammetry and Remote Sensing*, *75*, 64–75. https://doi.org/10.1016/j.isprsjprs.2012.10.003

Kumar, L., & Mutanga, O. (2017, September 1). Remote sensing of above-ground biomass. *Remote Sensing*, Vol. 9, p. 935. https://doi.org/10.3390/rs9090935

Kumar, L., Sinha, P., Taylor, S., & Alqurashi, A. F. (2015). Review of the use of remote sensing for biomass estimation to support renewable energy generation. *Journal of Applied Remote Sensing*, *9*(1), 097696. https://doi.org/10.1117/1.jrs.9.097696

Lausch, A., Erasmi, S., King, D. J., Magdon, P., & Heurich, M. (2017). Understanding forest health with Remote sensing-Part II-A review of approaches and data models. *Remote Sensing*, *9*(2), 1–33. https://doi.org/10.3390/rs9020129

Lechman, E. (2014). *ICTs DIFFUSION TRAJECTORIES AND ECONOMIC DEVELOPMENT – AN AND ECONOMIC DEVELOPMENT – AN EMPIRICAL EVIDENCE FOR 46*

*DEVELOPING COUNTRIES Ewa Lechman * GUT Faculty of Management and Economics*. (January). https://doi.org/10.13140/2.1.2496.4804

Li, A., Feng, M., Li, Y., & Liu, Z. (2016). ScienceDirect Information Technology and Quantitative Management (ITQM 2016) Application of outlier mining in insider identification based on Boxplot method. *Procedia - Procedia Computer Science*, *91*, 245–251. https://doi.org/10.1016/j.procs.2016.07.069

Li, M. F., Tang, X. P., Wu, W., & Liu, H. Bin. (2013). General models for estimating daily global solar radiation for different solar radiation zones in mainland China. *Energy Conversion and Management*, *70*, 139–148. https://doi.org/10.1016/j.enconman.2013.03.004

Lin, J., Wang, M., Ma, M., & Lin, Y. (2018a). Aboveground tree biomass estimation of sparse subalpine coniferous forest with UAV oblique photography. *Remote Sensing*, *10*(11). https://doi.org/10.3390/rs10111849

Lin, J., Wang, M., Ma, M., & Lin, Y. (2018b). Aboveground tree biomass estimation of sparse subalpine coniferous forest with UAV oblique photography. *Remote Sensing*, *10*(11), 1849. https://doi.org/10.3390/rs10111849

Lof, M., Schenau, S., de Jong, R., Remme, R., Graveland, C., & Hein, L. (2017). The SEEA EEA carbon account for the Netherlands. *Wageningen University & Research*, 64. Retrieved from file:///C:/Users/Vitor/Downloads/Carbon-account-2017.pdf

López García, J., Prado Molina, J., Manzo Delgado, L., & Peralta Higuera, A. (2016). Monitoreo de cambios en la densidad de cobertura forestal en bosque templado usando fotografías aéreas digitales de alta resolución. *Investigaciones Geograficas*, *2016*(90), 59–74. https://doi.org/10.14350/rig.47360

Louangrath, P. I. (2017). Sample Size Determination for Non-Finite Population. *SSRN Electronic Journal*, *3*(2), 141–152. https://doi.org/10.2139/ssrn.2710455

Lu, D. (2006). The potential and challenge of remote sensing-based biomass estimation. *International Journal of Remote Sensing*, *27*(7), 1297–1328. https://doi.org/10.1080/01431160500486732

Lu, D., & Batistella, M. (2005). Exploring TM image texture and its relationships with biomass estimation in Rondônia, Brazilian Amazon. *Acta Amazonica*, *35*(2), 249–257. https://doi.org/10.1590/s0044-59672005000200015

Lu, N., Zhou, J., Han, Z., Li, D., Cao, Q., Yao, X., … Cheng, T. (2019). Improved estimation of aboveground biomass in wheat from RGB imagery and point cloud data acquired with a low-cost unmanned aerial vehicle system. *Plant Methods*, *15*(1), 1–16. https://doi.org/10.1186/s13007-019-0402-3

Maack, J., Kattenborn, T., Fassnacht, F. E., Enßle, F., Hernández, J., Corvalán, P., & Koch, B. (2015). European Journal of Remote Sensing Modeling forest biomass using Very-High-Resolution data-Combining textural, spectral and photogrammetric predictors derived from spaceborne stereo images. *European Journal of Remote Sensing*, *48*, 245–261. https://doi.org/10.5721/EuJRS20154814

Mahmood, H., Siddique, M. R. H., Islam, S. M. Z., Abdullah, S. M. R., Matieu, H., Iqbal, M. Z., & Akhter, M. (2020). Applicability of semi-destructive method to derive allometric model for estimating aboveground biomass and carbon stock in the Hill zone of Bangladesh. *Journal of Forestry Research*, *31*(4), 1235–1245. https://doi.org/10.1007/s11676-019-00881-5

Mauya, E. W., Hansen, E. H., Gobakken, T., Bollandsås, O. M., Malimbwi, R. E., & Næsset, E. (2015). Effects of field plot size on prediction accuracy of aboveground biomass in airborne laser scanning-assisted inventories in tropical rain forests of Tanzania. *Carbon Balance and Management*, *10*(1), 10. https://doi.org/10.1186/s13021-015-0021-x

Mcroberts, R. E., Tomppo, E. O., & Czaplewski, R. L. (2015). *Sampling designs for national forest assessments*. Retrieved from http://www.fao.org/fileadmin/user_upload/national_forest_assessment/images/PDFs/English/KR2_EN__4_.pdf

Mishra, P., Pandey, C. M., Singh, U., Gupta, A., Sahu, C., & Keshri, A. (2019). Descriptive statistics and normality tests for statistical data. *Annals of Cardiac Anaesthesia*, *22*(1), 67–72. https://doi.org/10.4103/aca.ACA_157_18

Mitchard, E. (2016). *A Review of Earth Observation Methods for Detecting and Measuring Forest Change in the Tropics*. Retrieved from https://ecometrica.com/wp-content/uploads/2016/12/Review-of-EO-Methods-for-Detecting-and-Measuring-Forest-Change-in-the-Tropics-Final.pdf

Mohren, G. M. J., & Vodde, F. (2006). Forests and Forestry in The Netherlands. *Forests and Forestry in European Union Countries*, (Mei 2014), 1–17. Retrieved from

https://www.researchgate.net/publication/40110393_Forests_and_Forestry_in_the_Netherlands

Mutwiri, F. K., Odera, P. A., & Kinyanjui, M. J. (2017). Estimation of Tree Height and Forest Biomass Using Airborne LiDAR Data: A Case Study of Londiani Forest Block in the Mau Complex, Kenya. *Open Journal of Forestry*, *07*(02), 255–269. https://doi.org/10.4236/ojf.2017.72016

Muukkonen, P. (2007). Generalized allometric volume and biomass equations for some tree species in Europe. *European Journal of Forest Research*, *126*(2), 157–166. https://doi.org/10.1007/s10342-007-0168-4

Navulur, K. (2006). Multispectral Image Analysis Using the Object-Oriented Paradigm - Kumar Navulur - Google Books. Retrieved August 21, 2020, from https://books.google.nl/books?hl=en&lr=&id=vE3StuN8y1MC&oi=fnd&pg=PP1&ots=NSKw_lpPzf&sig=C8o_bcwJkdOqyHc-WQlyeDDhjv8&redir_esc=y#v=onepage&q&f=false

Nichol, J. E., & Sarker, M. L. R. (2011). Improved biomass estimation using the texture parameters of two high-resolution optical sensors. *IEEE Transactions on Geoscience and Remote Sensing*, *49*(3), 930–948. https://doi.org/10.1109/TGRS.2010.2068574

Noorian, N., Shataee-Jouibary, S., & Mohammadi, J. (2016). Assessment of different remote sensing data for forest structural attributes estimation in the Hyrcanian forests. *Forest Systems*, *25*(3). https://doi.org/10.5424/fs/2016253-08682

Ofner, M., Hirschmugl, M., Raggam, H., & Schardt, M. (2006). *Workshop on 3D Remote Sensing in Forestry, 14 th-15 th*. Retrieved from http://www.vexcel.co.at/

Okojie, J. A. (2017). Assessment of Forest Tree Structural Parameter Extractability from Optical Imaging UAV Datasets, In Ahaus Germany. https://doi.org/10.13140/RG.2.2.29630.28484

Pastor, J., Aber, J. D., & Melillo, J. M. (1984). Biomass prediction using generalized allometric regressions for some northeast tree species. *Forest Ecology and Management*, *7*(4), 265–274. https://doi.org/10.1016/0378-1127(84)90003-3

Patenaude, G., Milne, R., & Dawson, T. P. (2005, April). Synthesis of remote sensing approaches for forest carbon estimation: reporting to the Kyoto Protocol. *Environmental Science and Policy*, Vol. 8, pp. 161–178. https://doi.org/10.1016/j.envsci.2004.12.010

Paul, T. S. H., Kimberley, M. O., & Beets, P. N. (2019). Thinking outside the square: Evidence that plot shape and layout in forest inventories can bias estimates of stand metrics. *Methods in Ecology and Evolution*, *10*(3), 381–388. https://doi.org/10.1111/2041-210X.13113

Penman, J., Gytarsky, M., Hiraishi, T., Krug, T., Kruger, D., Pipatti, R., … Wagner, F. (2003). Good practice guidance for land use, land-use change and forestry. *Good Practice Guidance for Land Use, Land-Use Change and Forestry*. Retrieved from https://www.cabdirect.org/cabdirect/abstract/20083162304

Pizaña, J. M. G., Hernández, J. M. N., & Romero, N. C. (2016). Remote Sensing-Based Biomass Estimation. In *Environmental Applications of Remote Sensing*. https://doi.org/10.5772/61813

Platt, R. V., & Schoennagel, T. (2009). An object-oriented approach to assessing changes in tree cover in the Colorado Front Range 1938-1999. *Forest Ecology and Management*, *258*(7), 1342–1349. https://doi.org/10.1016/j.foreco.2009.06.039

Pleiades-1A Satellite Sensor | Satellite Imaging Corp. (2021). Retrieved June 11, 2021, from https://www.satimagingcorp.com/satellite-sensors/pleiades-1/

Popescu, S. C. (2007). Estimating biomass of individual pine trees using airborne lidar. *Biomass and Bioenergy*, *31*(9), 646–655. https://doi.org/10.1016/j.biombioe.2007.06.022

Pouliot, D. A., King, D. J., Bell, F. W., & Pitt, D. G. (2002). Automated tree crown detection and delineation in high-resolution digital camera imagery of coniferous forest regeneration. *Remote Sensing of Environment*, *82*(2–3), 322–334. https://doi.org/10.1016/S0034-4257(02)00050-0

Pu, R., & Landry, S. (2012). A comparative analysis of high spatial resolution IKONOS and WorldView-2 imagery for mapping urban tree species. *Remote Sensing of Environment*, *124*, 516–533. https://doi.org/10.1016/j.rse.2012.06.011

Ravindranath.N.H., & Ostwald, M. (2008). *Carbon Inventory Methods: Handbook for Greenhouse Gas Inventory, Carbon Mitigation and Roundwood Production Projects*. Retrieved from https://link.springer.com/content/pdf/10.1007%2F978-1-4020-6547-7.pdf

Rignot, E., Salas, W. A., & Skole, D. L. (1997). Mapping deforestation and secondary growth in Rondonia, Brazil, using imaging radar and thematic mapper data. *Remote Sensing of Environment*, *59*(2), 167–179. https://doi.org/10.1016/S0034-4257(96)00150-2

Romijn, E., Herold, M., Kooistra, L., Murdiyarso, D., & Verchot, L. (2012). Assessing capacities of

non-Annex I countries for national forest monitoring in the context of REDD+. *Environmental Science and Policy*, *19–20*, 33–48. https://doi.org/10.1016/j.envsci.2012.01.005

Ruiz, L., Hermosilla, T., Mauro, F., & Godino, M. (2014). Analysis of the Influence of Plot Size and LiDAR Density on Forest Structure Attribute Estimates. *Forests*, *5*(5), 936–951. https://doi.org/10.3390/f5050936

Saatchi, S. S., Harris, N. L., Brown, S., Lefsky, M., Mitchard, E. T. A., Salas, W., … Morel, A. (2011). Benchmark map of forest carbon stocks in tropical regions across three continents. *Proceedings of the National Academy of Sciences of the United States of America*, *108*(24), 9899–9904. https://doi.org/10.1073/pnas.1019576108

SEEA Experimental Ecosystem Accounting Revision | System of Environmental Economic Accounting. (2020). Retrieved October 18, 2020, from https://seea.un.org/content/seea-experimental-ecosystem-accounting-revision

Shimano, K. (1997). Analysis of the relationship between DBH and crown projection area using a new model. *Journal of Forest Research*, *2*(4), 237–242. https://doi.org/10.1007/BF02348322

Sinha, S., Jeganathan, C., Sharma, L. K., & Nathawat, M. S. (2015, January 20). A review of radar remote sensing for biomass estimation. *International Journal of Environmental Science and Technology*, Vol. 12, pp. 1779–1792. https://doi.org/10.1007/s13762-015-0750-0

Song, C., Dickinson, M. B., Su, L., Zhang, S., & Yaussey, D. (2010). Estimating average tree crown size using spatial information from Ikonos and QuickBird images: Across-sensor and across-site comparisons. *Remote Sensing of Environment*, *114*(5), 1099–1107. https://doi.org/10.1016/j.rse.2009.12.022

Sousa, A. M. O., Gonçalves, A. C., & da Silva, J. R. M. (2017). Above-Ground Biomass Estimation with High Spatial Resolution Satellite Images. In *Biomass Volume Estimation and Valorization for Energy*. https://doi.org/10.5772/65665

T. Vashum, K. (2012). Methods to Estimate Above-Ground Biomass and Carbon Stock in Natural Forests - A Review. *Journal of Ecosystem & Ecography*, *02*(04), 1–7. https://doi.org/10.4172/2157-7625.1000116

The European Green Deal - Wednesday, 15 January 2020. (2020). Retrieved October 18, 2020, from https://www.europarl.europa.eu/doceo/document/TA-9-2020-0005_EN.html

Troya-Galvis, A., Gancarski, P., Passat, N., & Berti-Equille, L. (2015). Unsupervised Quantification of Under-and Over-Segmentation for Object-Based Remote Sensing Image Analysis. *IEEE Journal of Selected Topics in Applied Earth Observations and Remote Sensing*, *8*(5), 1936–1945. https://doi.org/10.1109/JSTARS.2015.2424457

Valentini, R., Matteucci, G., Dolman, A. J., Schulze, E. D., Rebmann, C., Moors, E. J., … Jarvis, P. G. (2000). Respiration as the main determinant of carbon balance in European forests. *Nature*, *404*(6780), 861–865. https://doi.org/10.1038/35009084

Veljanovski, T., Kanjir, U., & Oštir, K. (2011). Object-based image analysis of remote sensing data. *Geodetski Vestnik*, *55*(04), 641–664. https://doi.org/10.15292/geodetski-vestnik.2011.04.641-664

Vorster, A. G., Evangelista, P. H., Stovall, A. E. L., & Ex, S. (2020). Variability and uncertainty in forest biomass estimates from the tree to landscape scale: The role of allometric equations. *Carbon Balance and Management*, *15*(1), 1–20. https://doi.org/10.1186/s13021-020-00143-6

Wahyuni, S., Jaya, I. N. S., & Puspaningsih, N. (2016). Model for estimating above ground biomass of reclamation forest using unmanned aerial vehicles. *Indonesian Journal of Electrical Engineering and Computer Science*, *4*(3), 586–593. https://doi.org/10.11591/ijeecs.v4.i3.pp586-593

Wang, M., Fei, X., Zhang, Y., Chen, Z., Wang, X., Tsou, J. Y., … Lu, X. (2018). Assessing texture features to classify coastal wetland vegetation from high spatial resolution imagery using Completed Local Binary Patterns (CLBP). *Remote Sensing*, *10*(5). https://doi.org/10.3390/rs10050778

Wang, Z., Jensen, J. R., & Im, J. (2010). An automatic region-based image segmentation algorithm for remote sensing applications. *Environmental Modelling and Software*, *25*(10), 1149–1165. https://doi.org/10.1016/j.envsoft.2010.03.019

Waterman, R. (2014). *R-squared and Root Mean Squared Error (RMSE) Video Title: R-squared and Root Mean Squared Error (RMSE)*. https://doi.org/10.4135/9781473996991

Watson, R. T., Noble, L., Bolin, B., Ravindranath.N, H., Verardo, D., & Dokken, D. (2000). *IPCC Special Report on Land Use, Land-Use Change, and Forestry*. Retrieved from https://www.researchgate.net/publication/253201133_Land_Use_Land-Use_Change_and_Forestry

Westoby, M. J., Brasington, J., Glasser, N. F., Hambrey, M. J., & Reynolds, J. M. (2012). "Structure-from-Motion" photogrammetry: A low-cost, effective tool for geoscience applications. *Geomorphology*, *179*, 300–314. https://doi.org/10.1016/j.geomorph.2012.08.021

Whitehead, K., & Hugenholtz, C. H. (2014). Remote sensing of the environment with small unmanned aircraft systems (UASs), part 1: a review of progress and challenges. *Journal of Unmanned Vehicle Systems*, *02*(03), 69–85. https://doi.org/10.1139/juvs-2014-0006

Xu, Z., Shen, X., Cao, L., Coops, N. C., Goodbody, T. R. H., Zhong, T., … Wu, X. (2020). Tree species classification using UAS-based digital aerial photogrammetry point clouds and multispectral imageries in subtropical natural forests. *International Journal of Applied Earth Observation and Geoinformation*, *92*, 102173. https://doi.org/10.1016/j.jag.2020.102173

Xue, J., & Su, B. (2017). Significant remote sensing vegetation indices: A review of developments and applications. *Journal of Sensors*, Vol. 2017. https://doi.org/10.1155/2017/1353691

Yang, G., Liu, J., Zhao, C., Li, Z., Huang, Y., Yu, H., … Yang, H. (2017, June 30). Unmanned aerial vehicle remote sensing for field-based crop phenotyping: Current status and perspectives. *Frontiers in Plant Science*, Vol. 8, p. 1111. https://doi.org/10.3389/fpls.2017.01111

Zianis, D., & Mencuccini, M. (2004). On simplifying allometric analyses of forest biomass. *Forest Ecology and Management*, *187*(2–3), 311–332. https://doi.org/10.1016/j.foreco.2003.07.007

Appendices

Appendix 1. Different rulesets and algorithm descriptions used for multiresolution segmentation process at different spatial resolution.

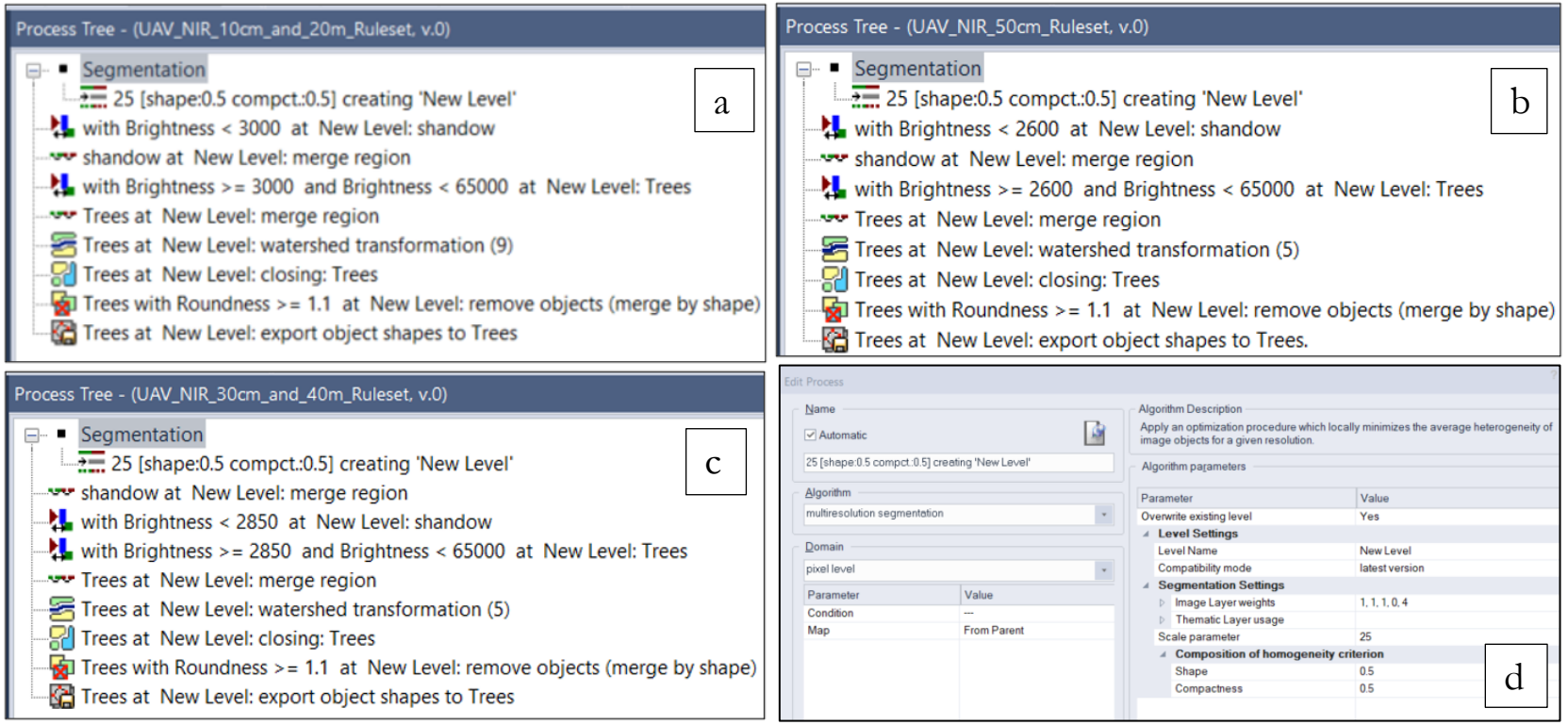

Different rule sets used at different resolutions for UAV_MS: a) Rule set for 10 cm and 20 cm, b) Rule set for 50 cm, c) Rule set for 30cm and 40 cm.

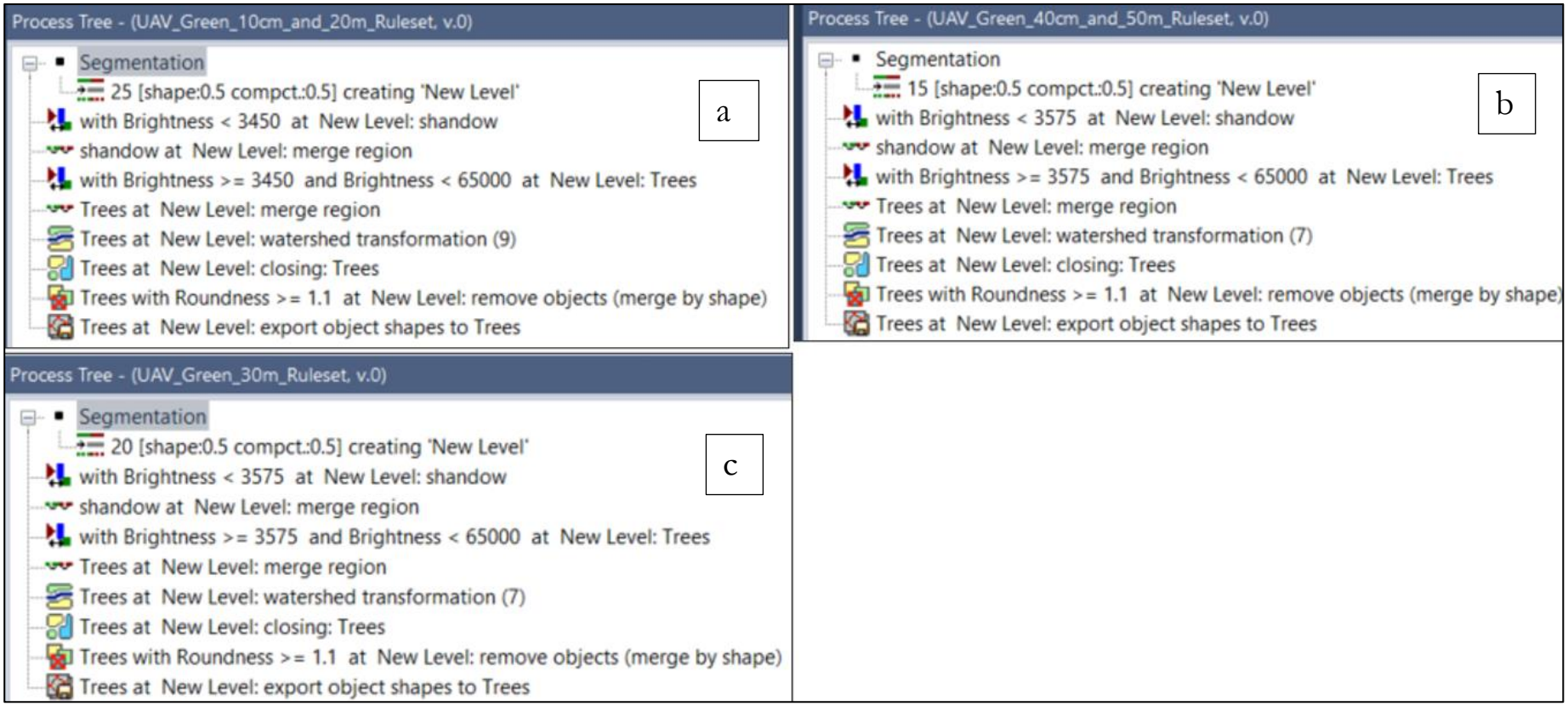

Different rule sets used at different resolutions for UAV_RGB: a) Rule set for 10 cm and 20 cm, b) Rule set for 40 cm and 50 cm and c) Rule set for 30cm.

UAV_RGB Multiresolution algorithm description at 10cm and 20cm resolution

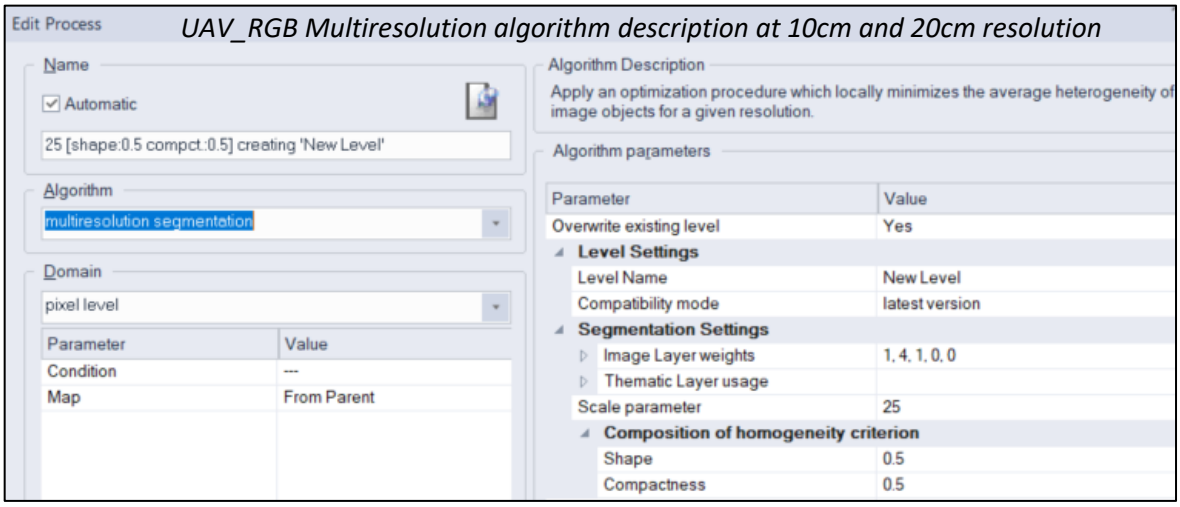

UAV_RGB Multiresolution algorithm description at 30cm

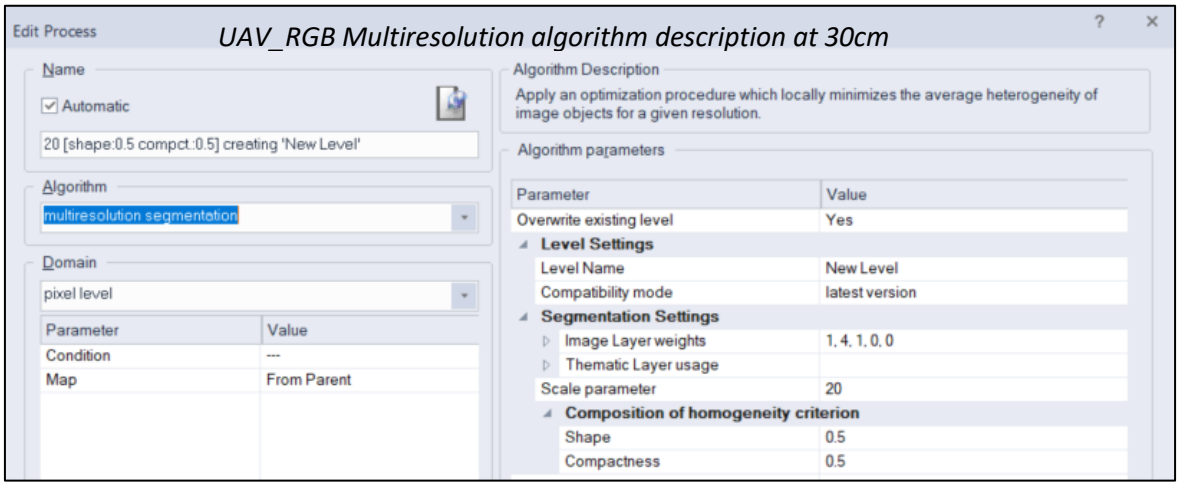

UAV_RGB Multiresolution algorithm description at 40cm and 50cm

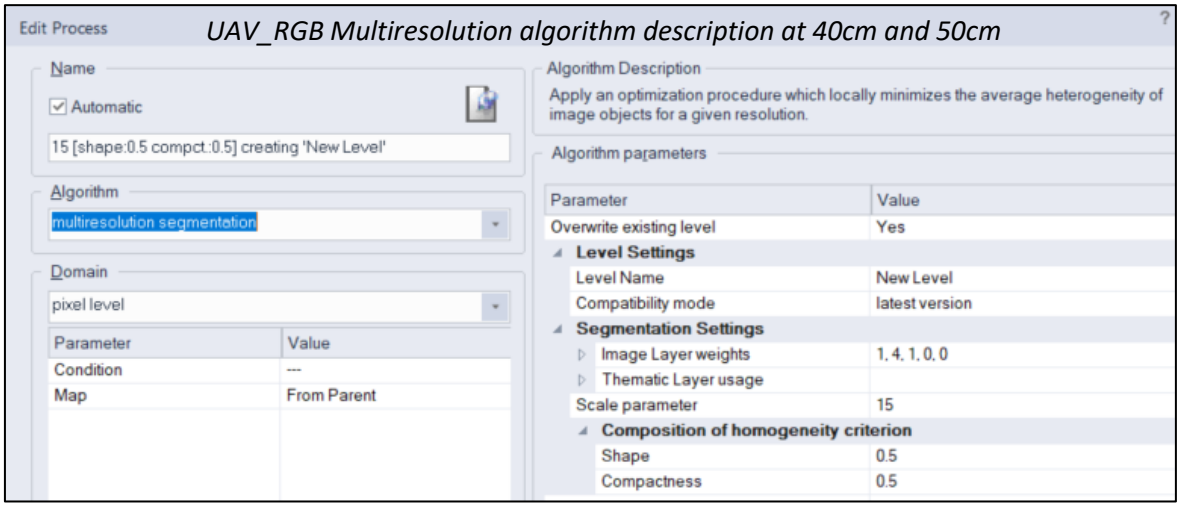

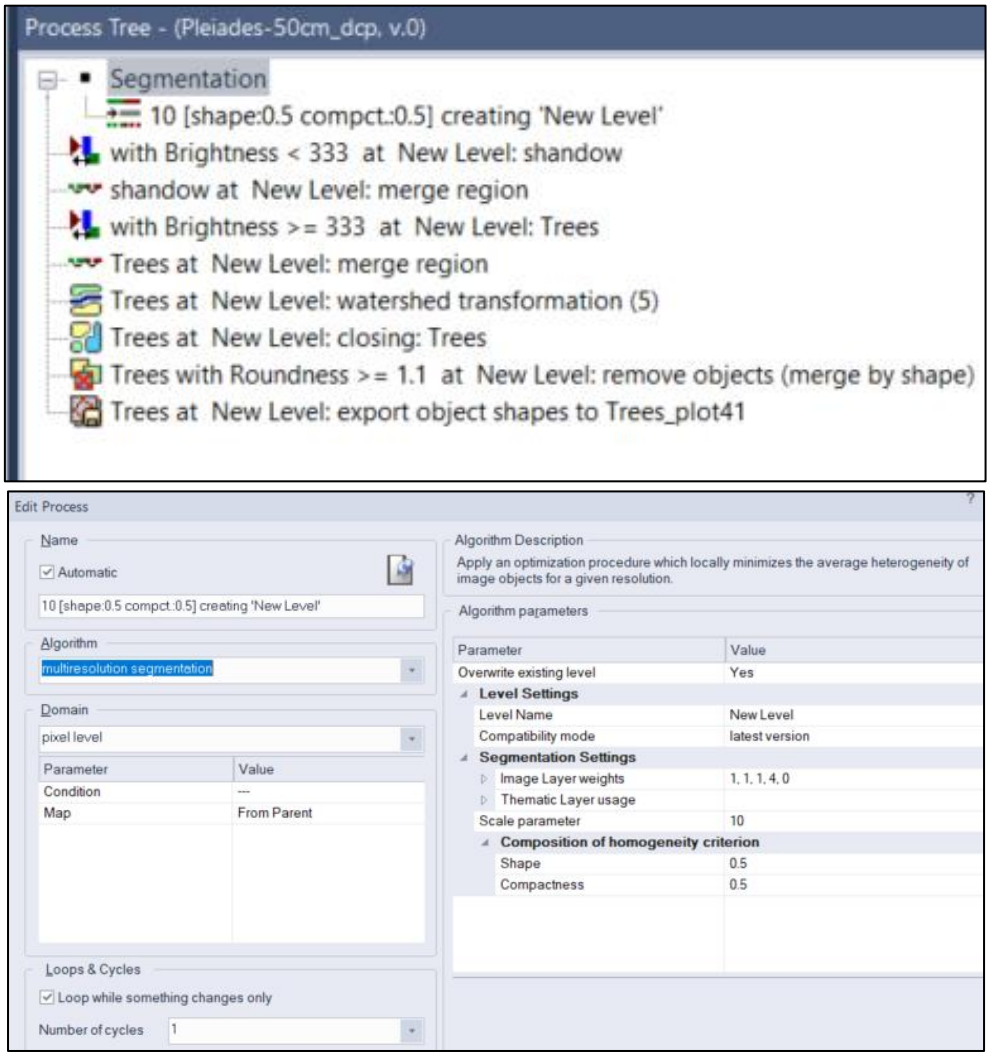

Rule sets and algorithm descriptions used for Pleiades at 50 cm.

Appendix 2. Summary of Pix4D photogrammetry initial report

Project	B45
Processed	2020-09-29 10:58:03
Camera Model Name(s)	FC330_3.6_4000x3000 (RGB)
Average Ground Sampling Distance (GSD)	4.49 cm / 1.77 in
Area Covered	0.575 km^2 / 57.5429 ha / 0.22 sq. mi. / 142.2651 acres
Time for Initial Processing (without report)	53m:49s

Quality Check

Images	median of 58179 keypoints per image	✓
Dataset	1470 out of 1470 images calibrated (100%), all images enabled	✓
Camera Optimization	0% relative difference between initial and optimized internal camera parameters	✓
Matching	median of 5730.64 matches per calibrated image	✓
Georeferencing	yes, 9 GCPs (9 3D), mean RMS error = 0.011 m	✓

Preview

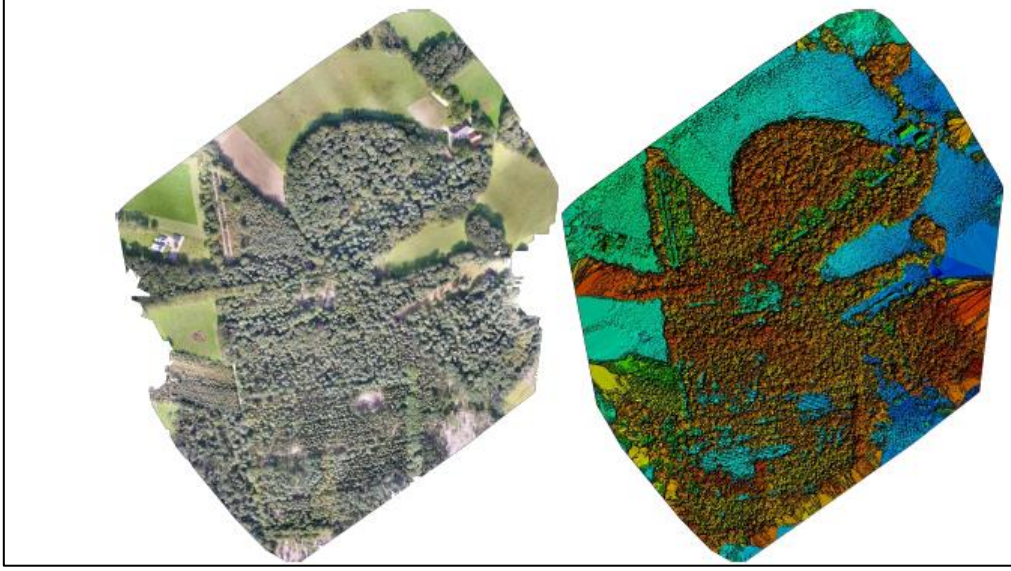

Project	Block4_MS2
Processed	2020-11-16 15:34:54
Camera Model Name(s)	Sequoia_4.0_1280x960 (Green), Sequoia_4.0_1280x960 (Red), Sequoia_4.0_1280x960 (Red edge), Sequoia_4.0_1280x960 (NIR)
Rig name(s)	«Sequoia»
Average Ground Sampling Distance (GSD)	11.20 cm / 4.41 in
Area Covered	0.321 km^2 / 32.1197 ha / 0.12 sq. mi. / 79.4107 acres

Quality Check

Images	median of 10000 keypoints per image	✓
Dataset	4400 out of 4400 images calibrated (100%), all images enabled	✓
Camera Optimization	0.04% relative difference between initial and optimized internal camera parameters	✓
Matching	median of 5089.4 matches per calibrated image	✓
Georeferencing	yes, 10 GCPs (10 3D), mean RMS error = 0.085 m	✓

Preview

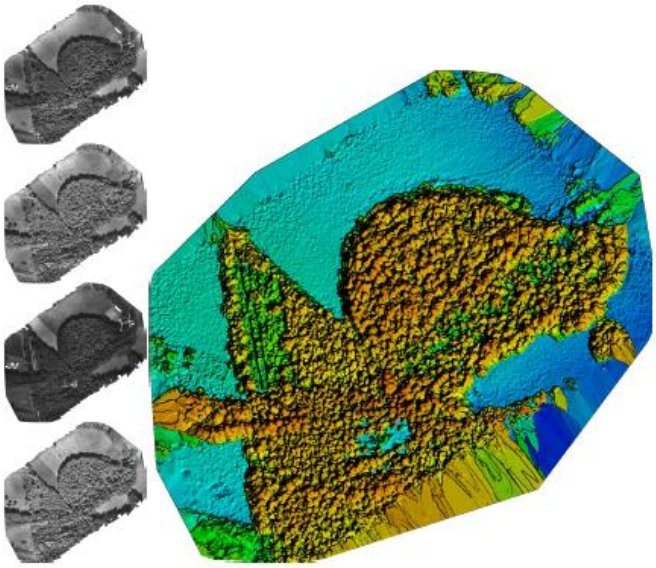

Project	Block5_MS
Processed	2020-11-20 17:58:40
Camera Model Name(s)	Sequoia_4.0_1280x960 (Green), Sequoia_4.0_1280x960 (Red), Sequoia_4.0_1280x960 (Red edge), Sequoia_4.0_1280x960 (NIR)
Rig name(s)	«Sequoia»
Average Ground Sampling Distance (GSD)	11.41 cm / 4.49 in
Area Covered	0.356 km^2 / 35.5594 ha / 0.14 sq. mi. / 87.9146 acres

Quality Check

Images	median of 10000 keypoints per image	✓
Dataset	3468 out of 3496 images calibrated (99%), all images enabled	✓
Camera Optimization	0.03% relative difference between initial and optimized internal camera parameters	✓
Matching	median of 4796.65 matches per calibrated image	✓
Georeferencing	yes, 6 GCPs (6 3D), mean RMS error = 0.07 m	✓

Preview

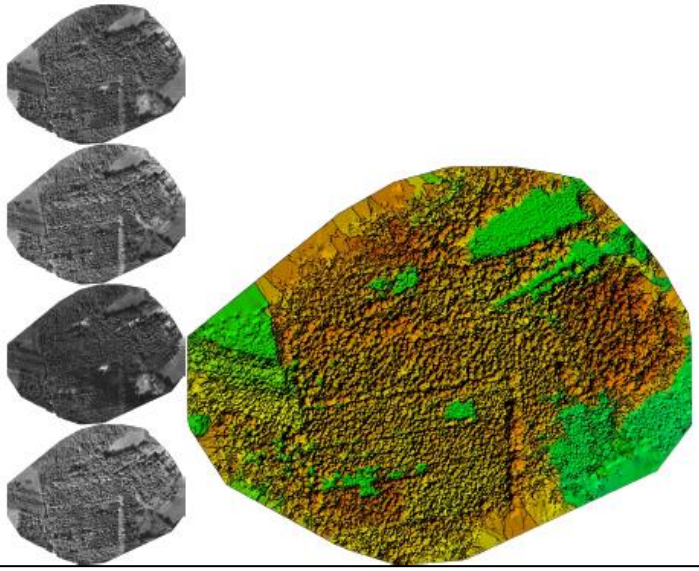

Project	mish
Processed	2021-05-30 02:27:27
Camera Model Name(s)	FC330_3.6_4000x3000 (RGB)
Average Ground Sampling Distance (GSD)	4.41 cm / 1.74 in
Area Covered	0.274 km^2 / 27.4437 ha / 0.11 sq. mi. / 67.8500 acres
Time for Initial Processing (without report)	04m:55s

Quality Check

Images	median of 57501 keypoints per image	✓
Dataset	187 out of 198 images calibrated (94%), all images enabled, 4 blocks	⚠
Camera Optimization	0.41% relative difference between initial and optimized internal camera parameters	✓
Matching	median of 4071.09 matches per calibrated image	✓
Georeferencing	yes, 4 GCPs (4 3D), mean RMS error = 0.006 m	✓

Preview

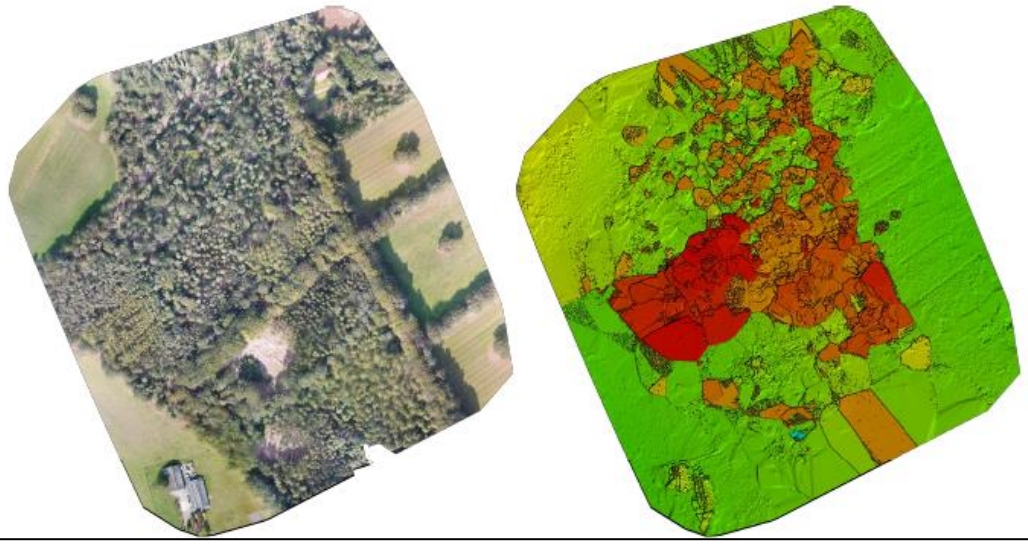

Project	block9_MS
Processed	2021-01-01 00:52:11
Camera Model Name(s)	Sequoia_4.0_1280x960 (Green), Sequoia_4.0_1280x960 (Red), Sequoia_4.0_1280x960 (Red edge), Sequoia_4.0_1280x960 (NIR)
Rig name(s)	«Sequoia»
Average Ground Sampling Distance (GSD)	10.06 cm / 3.96 in
Area Covered	0.411 km^2 / 41.0921 ha / 0.16 sq. mi. / 101.5934 acres
Time for Initial Processing (without report)	06h:30m:07s

Quality Check

Images	median of 10000 keypoints per image	✓
Dataset	5588 out of 5788 images calibrated (96%), 28 images disabled, 3 blocks	⚠
Camera Optimization	0% relative difference between initial and optimized internal camera parameters	✓
Matching	median of 3844.34 matches per calibrated image	✓
Georeferencing	yes, 3 GCPs (3 3D), mean RMS error = 0.287 m	⚠

Preview

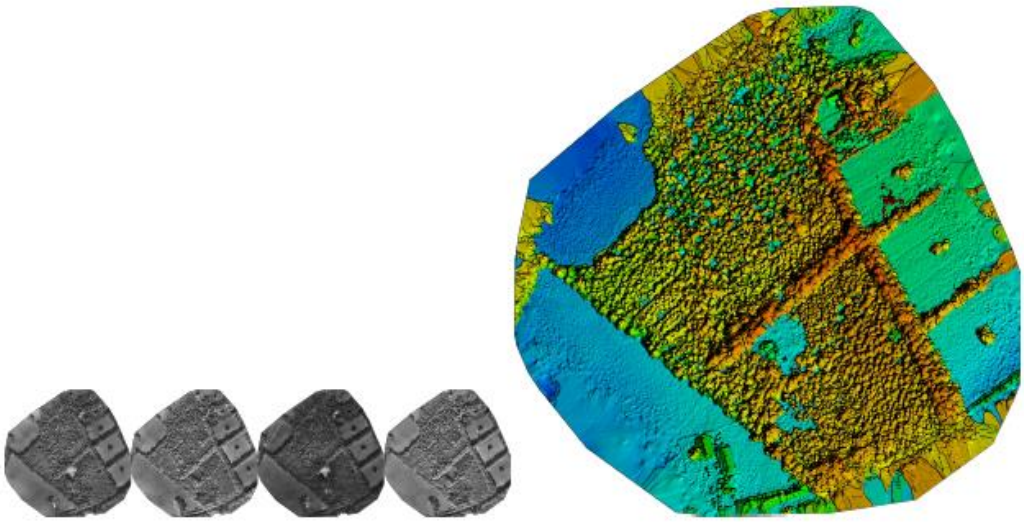

Appendix 3. AGB per plot (mg) at different spatial resolutions

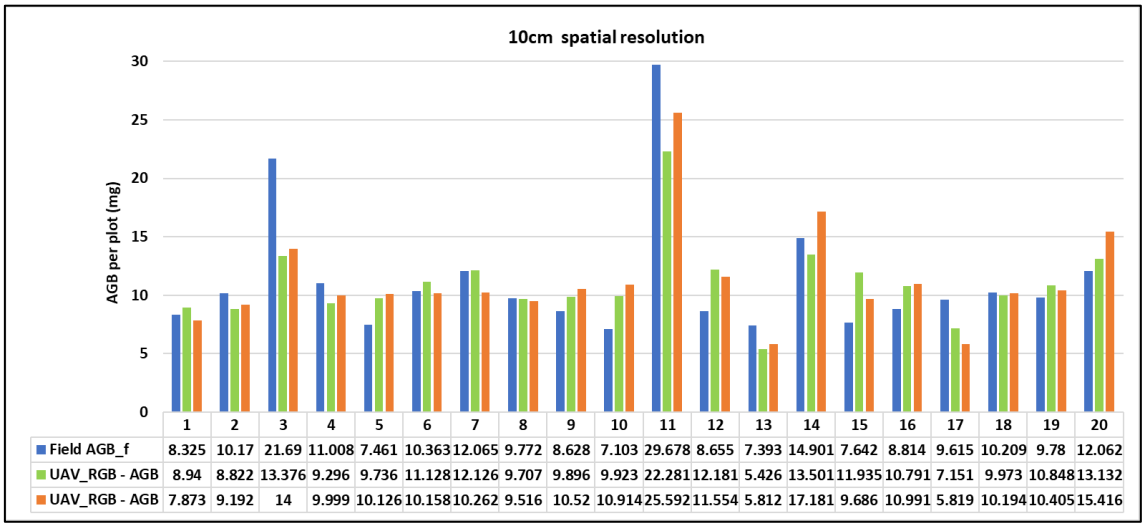

	1	2	3	4	5	6	7	8	9	10	11	12	13	14	15	16	17	18	19	20
Field AGB_f	8.325	10.17	21.69	11.008	7.461	10.363	12.065	9.772	8.628	7.103	29.678	8.655	7.393	14.901	7.642	8.814	9.615	10.209	9.78	12.062
UAV_RGB - AGB	8.94	8.822	13.376	9.296	9.736	11.128	12.126	9.707	9.896	9.923	22.281	12.181	5.426	13.501	11.935	10.791	7.151	9.973	10.848	13.132
UAV_RGB - AGB	7.873	9.192	14	9.999	10.126	10.158	10.262	9.516	10.52	10.914	25.592	11.554	5.812	17.181	9.686	10.991	5.819	10.194	10.405	15.416

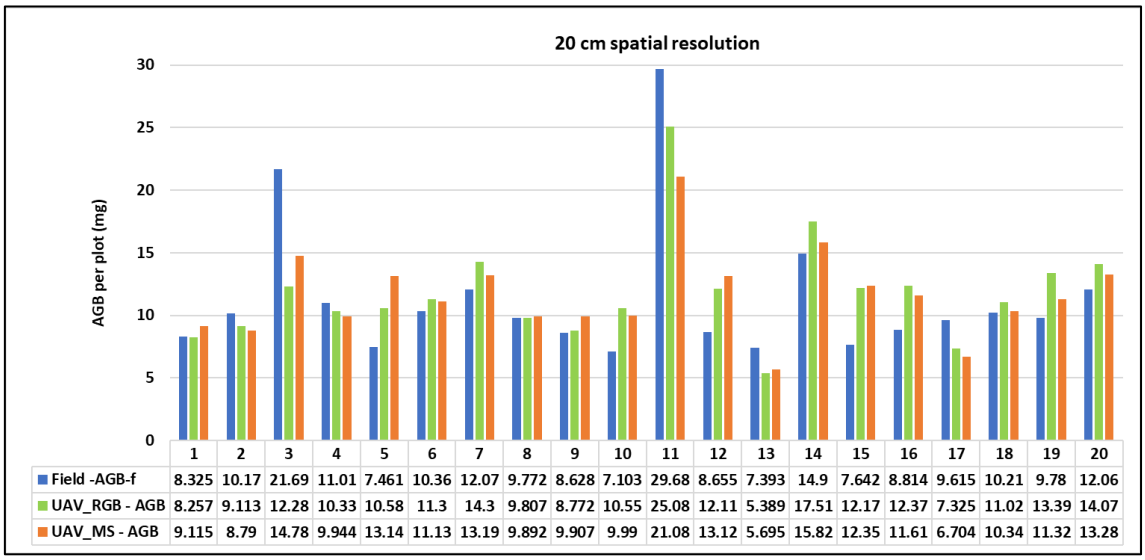

	1	2	3	4	5	6	7	8	9	10	11	12	13	14	15	16	17	18	19	20
Field -AGB-f	8.325	10.17	21.69	11.01	7.461	10.36	12.07	9.772	8.628	7.103	29.68	8.655	7.393	14.9	7.642	8.814	9.615	10.21	9.78	12.06
UAV_RGB - AGB	8.257	9.113	12.28	10.33	10.58	11.3	14.3	9.807	8.772	10.55	25.08	12.11	5.389	17.51	12.17	12.37	7.325	11.02	13.39	14.07
UAV_MS - AGB	9.115	8.79	14.78	9.944	13.14	11.13	13.19	9.892	9.907	9.99	21.08	13.12	5.695	15.82	12.35	11.61	6.704	10.34	11.32	13.28

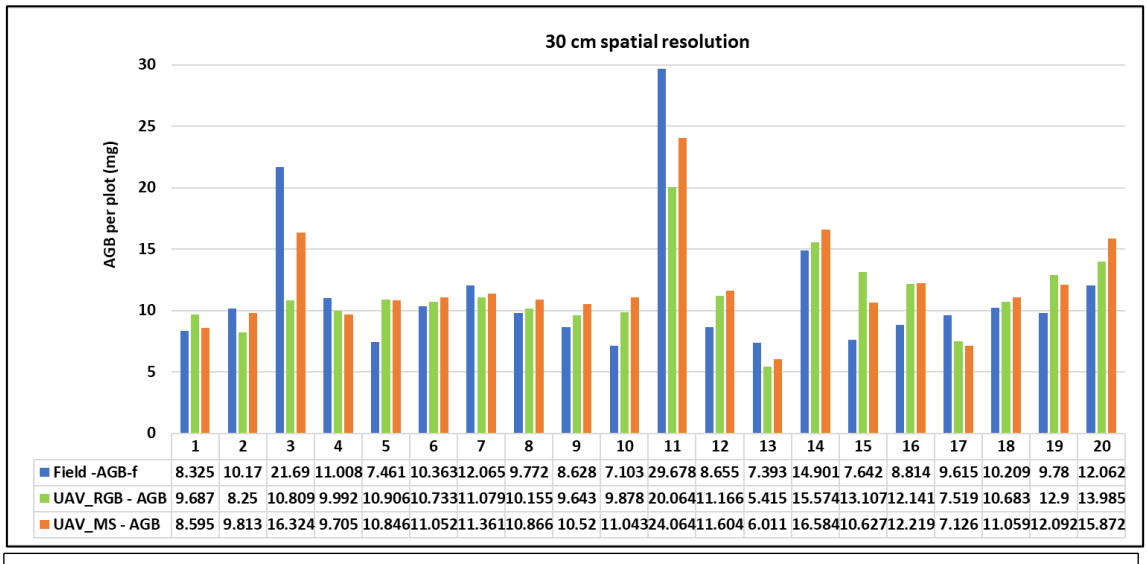

	1	2	3	4	5	6	7	8	9	10	11	12	13	14	15	16	17	18	19	20
Field -AGB-f	8.325	10.17	21.69	11.008	7.461	10.363	12.065	9.772	8.628	7.103	29.678	8.655	7.393	14.901	7.642	8.814	9.615	10.209	9.78	12.062
UAV_RGB - AGB	9.687	8.25	10.809	9.992	10.906	10.733	11.079	10.155	9.643	9.878	20.064	11.166	5.415	15.574	13.107	12.141	7.519	10.683	12.9	13.985
UAV_MS - AGB	8.595	9.813	16.324	9.705	10.846	11.052	11.361	10.866	10.52	11.043	24.064	11.604	6.011	16.584	10.627	12.219	7.126	11.059	12.092	15.872

AGB-field: AGB estimated from the field.
MS-Band weight 1,1,1,4 (R,G,B,NIR): AGB estimated from segmentation process influenced by near-infrared band.
RGB-Band weight 1,4,1,0,0 (R,G,B,NIR): AGB estimated from segmentation process influenced by green band.

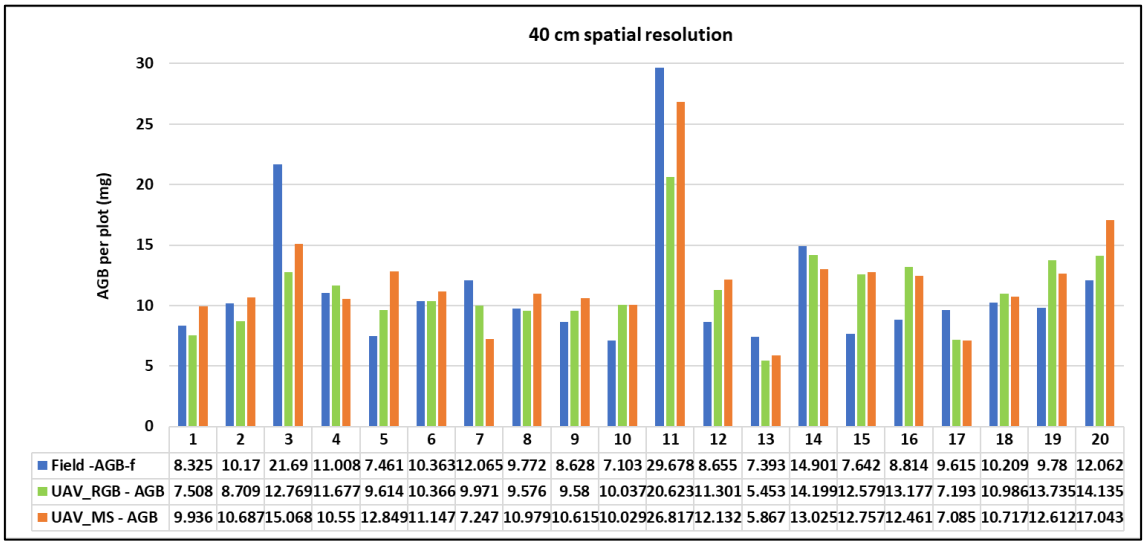

	1	2	3	4	5	6	7	8	9	10	11	12	13	14	15	16	17	18	19	20
Field -AGB-f	8.325	10.17	21.69	11.008	7.461	10.363	12.065	9.772	8.628	7.103	29.678	8.655	7.393	14.901	7.642	8.814	9.615	10.209	9.78	12.062
UAV_RGB - AGB	7.508	8.709	12.769	11.677	9.614	10.366	9.971	9.576	9.58	10.037	20.623	11.301	5.453	14.199	12.579	13.177	7.193	10.986	13.735	14.135
UAV_MS - AGB	9.936	10.687	15.068	10.55	12.849	11.147	7.247	10.979	10.615	10.029	26.817	12.132	5.867	13.025	12.757	12.461	7.085	10.717	12.612	17.043

AGB-field: AGB estimated from the field.
MS-Band weight 1,1,1,4 (R,G,B,NIR): AGB estimated from segmentation process influenced by near-infrared band.
RGB-Band weight 1,4,1,0,0 (R,G,B,NIR): AGB estimated from segmentation process influenced by green band.

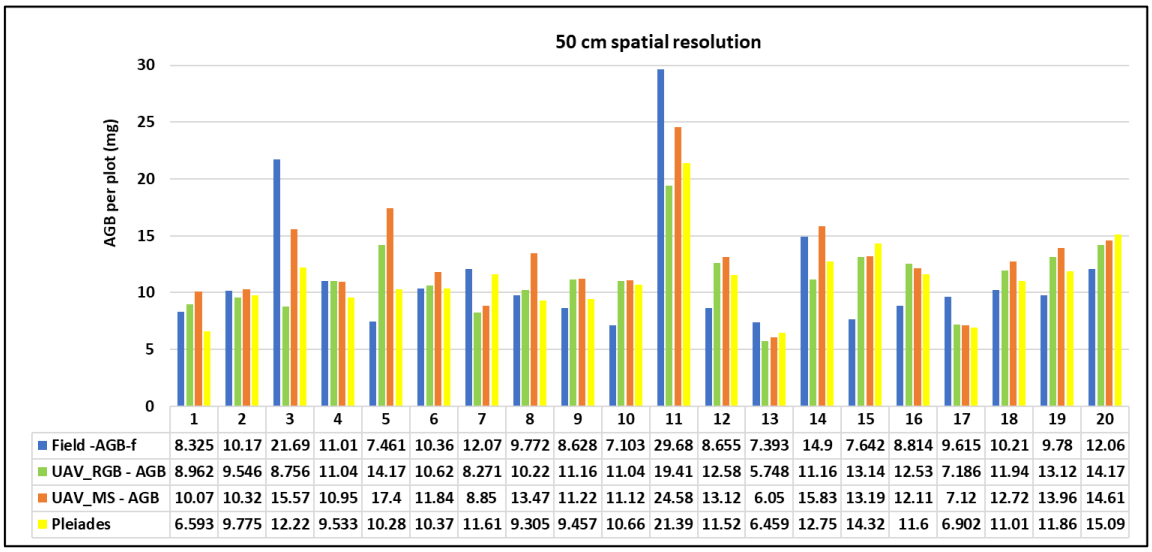

	1	2	3	4	5	6	7	8	9	10	11	12	13	14	15	16	17	18	19	20
Field -AGB-f	8.325	10.17	21.69	11.01	7.461	10.36	12.07	9.772	8.628	7.103	29.68	8.655	7.393	14.9	7.642	8.814	9.615	10.21	9.78	12.06
UAV_RGB - AGB	8.962	9.546	8.756	11.04	14.17	10.62	8.271	10.22	11.16	11.04	19.41	12.58	5.748	11.16	13.14	12.53	7.186	11.94	13.12	14.17
UAV_MS - AGB	10.07	10.32	15.57	10.95	17.4	11.84	8.85	13.47	11.22	11.12	24.58	13.12	6.05	15.83	13.19	12.11	7.12	12.72	13.96	14.61
Pleiades	6.593	9.775	12.22	9.533	10.28	10.37	11.61	9.305	9.457	10.66	21.39	11.52	6.459	12.75	14.32	11.6	6.902	11.01	11.86	15.09

AGB-field: AGB estimated from the field.
MS-Band weight 1,1,1,4 (R,G,B,NIR): AGB estimated from segmentation process influenced by near-infrared band.
RGB-Band weight 1,4,1,0,0 (R,G,B,NIR): AGB estimated from segmentation process influenced by green band.
Pleiades-Band weight 1,1,1,4 (R,G,B,NIR): AGB estimated from segmentation process influenced by near-infrared band.

Appendix 4. Data sheet for forest tree parameters in Haagse Bos

Observer name:					Date:	Plot #:
Central point					X	Y
Plot radius:						
Forest density:	Dense		Medium			Low
General comment:						

Tree #	Species	DBH (cm)	Crown diameter (m)		Tree position		Comment
			N-S	W-E	Distance from centre point (m)	Compass bearing (degrees)	